Converse Magnetoelectric Resonators for Biomagnetic Field Sensing

in partial fulfillment of the requirements for the degree of Doctor of Engineering (Dr.-Ing.)

Dissertation

by Patrick Hayes

Submitted to the Faculty of Engineering of
Christian-Albrechts-Universität zu Kiel

Kiel, July 2020

biomagnetic sensing

SFB 1261

	Date of oral examination: 03.12.2020
Examiners	Prof. Dr.-Ing. Eckhard Quandt Prof. Dr.-Ing. Reinhard Knöchel

Eidesstattliche Erklärung

Ich versichere hiermit an Eides statt, dass ich die vorliegende Dissertation selbstständig und ohne unzulässige fremde Hilfe erbracht habe. Ich habe keine anderen als die angegebenen Quellen und Hilfsmittel benutzt so wie wörtliche und sinngemäße Zitate kenntlich gemacht. Die Arbeit hat in gleicher oder ähnlicher Form noch keiner Prüfungsbehörde vorgelegen. Der Inhalt der Arbeit wurde in Teilen bereits in meinen wissenschaftlichen Publikationen veröffentlicht. Dies ist in der Arbeit entsprechend vermerkt. Die Arbeit ist nach bestem Wissen und Gewissen konform mit den Regeln guter wissenschaftlicher Praxis, welche durch die Deutsche Forschungsgemeinschaft festgelegt sind.

Ort, Datum

Patrick Hayes

Abstract

English

Contact-less biomagnetic sensing constitutes the next frontier for advanced healthcare, bringing novel diagnostic abilities using multichannel magnetocardiography (MCG) and magnetoencephalography (MEG) either as a single source of information for rapid patient screening or in combination with established methods such as electrocardiography (ECG) and electroencephalography (EEG) as a source for additional patient information. The combination of established electrical with magnetic patient information potentially leads to novel tools for deep knowledge generation towards pathologies and early prevention of such. The main obstacle towards biomagnetic diagnosis using magnetic imaging techniques is the lack of easy applicable sensor technology which offers extremely low magnetic noise floors; realtime MCG measurements demand for lower than $10\,\mathrm{pT}/\sqrt{\mathrm{Hz}}$, reaching below $100\,\mathrm{fT}/\sqrt{\mathrm{Hz}}$ enables even MEG signal acquisition. Such extremely minute amplitudes that are six to seven orders lower than earth's permanent magnetic field, demand lowest noise sensor technology as the low frequency signal regime below about 1 kHz is strongly affected by omnipresent 1/f-noise.

Magnetoelectric (ME) thin film composites consisting of a sputtered piezoelectric (PE) and an amorphous magnetostrictive (MS) layer are usually employed for measurements of magnetic fields passively, i.e. an AC magnetic field directly generates an ME voltage by mechanical coupling of the MS deformation to the PE phase. In order to achieve high field sensitivities, a magnetic bias field is required to operate at the maximum piezomagnetic coefficient of the MS phase. Additionally using mechanical resonances further enhances this direct ME effect size. Despite being able to directly detect very small field amplitudes on the order of $1\,\mathrm{pT}/\sqrt{\mathrm{Hz}}$ for magnetic fields of a frequency exactly matching mechanical resonances comes at the expense of available signal bandwidth, because of rather high resonator quality factors. Strong 1/f noise prevalent in the low frequency regime, makes DC or low frequency magnetic fields tedious to record in that regime using direct ME detection scheme.

In the presented work the PE phase is actively excited, thus exploiting the converse ME effect, remedying the shortcomings of the direct effect. ME composites are demonstrated for use as precision sensors, capable of magnetic signal detection in the low frequency, low amplitude biomagnetic regime. The combination of the converse ME effect with high frequency acoustic resonances leads to high piezoelectric stresses generated within the composite, leading to large inverse magnetostriction and thus high sensitivity. A limit of detection (LOD) of $70\,\mathrm{pT}/\sqrt{\mathrm{Hz}}$ at 10 Hz is obtained with composites based on amorphous films of Iron-Cobalt-Silicon-Boron (FeCoSiB). Exploiting advanced magnetoelectric composites based on exchange biased FeCoSiB films (EB-FeCoSiB) LOD values reaching down to $17\,\mathrm{pT}/\sqrt{\mathrm{Hz}}$ at 10 Hz are demonstrated. A trial recording a healthy subjects human MCG signal using an advanced ME composite demonstrates the practical feasibility of biomagnetic measurements and paves the way for routine, realtime biomagnetic measurements in the future.

German

Kontaktlose biomagnetische Diagnostik stellt die nächste Generation von Patientenmonitoring und bildgebender Diagnostik dar, sie ist in der Lage einen schnellen, kontaktlosen Überblick der Vitalfunktionen zu liefern. In Kombination mit etablierten Methoden wie Elektrokardiografie (EKG) und Elektroenzephalografie (EEG) entsteht ein zusätzliches Werkzeug zur Erlangung tieferer Informationen über Pathogenesen und ermöglichen somit eine frühzeitige Erkennung solcher. Die größte technische Hürde der biomagnetischen Diagnose stellt die Entwicklung einer anwenderfreundlichen, wartungsarmen Sensortechnologie dar. Diese Technologie muss über ein extrem niedriges magnetisches Rauschen von kleiner als $10\,\mathrm{pT}/\sqrt{\mathrm{Hz}}$ für Echtzeit Magnetokardiografie (MKG) und bis unter $100\,\mathrm{fT}/\sqrt{\mathrm{Hz}}$ für Magnetoenzephalografie (MEG) verfügen. Derartige Feldstärken von biomagnetischem Niveau sind etwa sechs bis sieben Größenordnungen geringer als das statische Erdmagnetfeld und dabei ebenfalls stets niederfrequent, unterhalb etwa 1 kHz. Damit liegen die relevanten Magnetfelder im Bereich des omnipräsenten 1/f-Rauschens.

Magnetoelektrische Dünnschicht-Komposite werden üblicherweise passiv betrieben, indem ein magnetisches Wechselfeld direkt zu einer proportionalen ME-Spannung führt. Dies geschieht mittels magnetostriktiver Dehnung welche durch mechanische Kopplung auf ein Piezoelektrikum übertragen wird und dort eine elektrische Spannung über den direkten piezoelektrischen Effekt erzeugt. Um den größtmöglichen piezomagnetischen Koeffizienten zu erhalten, kommt zusätzlich ein statisches magnetisches Haltefeld zum Einsatz. Durch die Ausnutzung mechanischer Resonanzen wird die Oszillation verstärkt, diese Verstärkung führt in gleichem Maße zu einer Verstärkung des ME-Effekts. Auf diese Weise ist es möglich, magnetische Detektionsgrenzen von etwa $1\,\mathrm{pT}/\sqrt{\mathrm{Hz}}$ zu erreichen, weit im erforderlichen Bereich für Echtzeit MKG Messungen. Diese direkte Ausnutzung mechanischer Resonanzen von hohem Gütefaktor, bringt den wesentlichen Nachteil, dass die Bandbreite des ME Oszillators auf wenige Herz beschränkt ist, welches einer praktischen, breitbandigen Signalerfassung entgegen steht.

In dieser Arbeit wird die piezoelektrische Materialphase direkt elektrisch angeregt, es wird der inverse ME-Effekt ausgenutzt. Dieser inverse ME Effekt stellt sich als vorteilhaft im Bezug auf den direkten ME-Effekt heraus, da eine rauscharme Operation ermöglicht wird. Magnetoelektrische Dünnschicht-Komposite werden als Präzisionssensoren zur Detektion von niederfrequenten magnetischen Kleinstsignalen untersucht. Die Kombination aus inversem ME-Effekt und der Ausnutzung hochfrequenter mechanischer Oszillationen führt zu starken mechanischen Verspannungen in der magnetostriktiven Phase und dadurch zu hoher Empfindlichkeit des Sensor-Komposites. Eine Detektionsgrenze von $70\,\mathrm{pT}/\sqrt{\mathrm{Hz}}$ bei einer Frequenz von 10 Hz wird unter Verwendung von magnetostriktiven Einfachlagen erreicht. Die Verwendung fortgeschrittener Mehrlagen-Materialsysteme führt zu einer weiteren Verringerung der Detektionsgrenze auf $17\,\mathrm{pT}/\sqrt{\mathrm{Hz}}$ bei 10 Hz. Schließlich wird in einer Feldstudie am gesunden Probanden eine Machbarkeit zur Detektion humaner MKG Signale gezeigt.

Contents

Chapter 1

Introduction

The field of existing magnetic sensing technology is wide, wherein magnetic sensing as a medical tool remains an exotic niche. Sensing of the human vital functions is an established branch in which the human, the system under test, did not develop notably within recent centuries. As such, probing whether a heart is operating by checking for a periodic mechanical deformation of an artery is a straightforward task. However, early knowledge about a covert heart anomaly may be gained by improved resolution, quicker sampling during extended periods of time while performing a modern multichannel electrocardiographic (ECG) recording. Its analogue, magnetocardiography (MCG) exploits the information encoded within the magnetic component, which has the inherent advantage of enabling contact-less recording of such biomagnetic signals. However, new possibilities based on MCG received considerably less attention during recent decades, since available systems usually employ SQUID (Superconducting Quantum Interference Device) magnetometers which are complicated to operate and thus associated costs are unbearable for clinical application.

The diagnosis, especially the localization of a fault using the magnetic field rather than the electrical potential stays unaltered upon passing the human tissue since the variation of its magnetic permeability μ_r is minute compared to its electrical counterpart ϵ_r varying over orders[MP95], potentially skewing electrical signals on transition. Magnetoencephalography (MEG) poses a real frontier, since detecting a malfunction in cortical activity is impossible by any simple means, there is no alternative to acquiring electric surface potentials using many electrodes or detecting emitted neuromagnetic signals around the scalp. The field amplitudes emitted are incredibly small ($10 \ldots 100\,\mathrm{fT}$), two to three orders smaller than MCG signals. Thus a whole field of applications already exists with prime questions arising from epilepsy research and treatment, solely limited by available technology. A recent development, employing optically pumped magnetometers (OPM), being way less tedious to operate than SQUID

magnetometers, is a further step into practical acquisition and utilisation of human biomagnetic signals of any kind [Sha+18].

This thesis is written within a joint attempt of several disciplines to floodlight future possibilities of magnetoelectric composites for use as very sensitive magnetic field sensors, especially directly applied to the demanding field of biomagnetic sensing, enabling new treatments on the knowledge gained. The following thesis presents work done within PAK902 and its successor DFG (Deutsche Forschungsgemeinschaft) collaborative research centre SFB1261, dedicated especially to the converse ME effect under project A7.

Starting with a general introduction into magnetic sensing, especially its technology and areas of application are outlined. Since the ME effect is not yet commercialised and thus sometimes considered rather exotic in text books on sensor technology, a brief overview is given concluding the chapter.

Three journal publications are presented along with additional material deserving record in this manuscript, aiming to present further insights and possibly spark new ideas. A chapter of unpublished recent developments exploiting sophisticated magnetic layer systems to leap towards the goal of contact-less biomagnetic measurements concludes the thesis.

1.1 State of the Art in Magnetic Sensing

1.1.1 Artificial or Controlled Magnetic Signals

The vast majority of magnetic sensors are used as a vehicle to sense the strength or presence of a known magnetic field created artificially by either a permanent magnet, conductor or coil [BO89] or non-magnetic quantities [PFB96] which can be quantified contact-less with the aid of artificial magnetic field sources, such as a liquid level in a tank by a floating permanent magnet. [Rip00] Volume market applications in the vastly booming sensors market [Per+14] include, but are not limited to flow metering by immersing a magnetic paddle in a flowing fluid, position sensing by attaching a permanent magnet to a rotor or shaft, magnetic positioning by magnetic scales [HKG19]. Electromobility which is an emerging topic as of about 2014 [DP16] hosts a plethora of new opportunities for magnetic sensors in many aspects of (electric) mobility, such as pedal inclination sensing, steering wheel angular sensing [Fle08], charging current sensors, proximity detection, electronic joystick controls and rotary encoders [Tum11].

Endpoint detection, interlock and safety mechanisms are often also performed magnetically, in these cases a switching characteristic (sometimes with hysteresis) may be

required, rather than a linear output voltage. Classic reed switches perform exactly this task mechanically by closing a spring-loaded switch through externally applied magnetic force. Hall sensors are used whenever the application requires elevated frequency (e.g. flow meters), available even containing integrated Schmitt trigger circuitry readily delivering switching operation including hysteresis, termed hall switches.

The magnetic recording community is very large but is often excluded within the discussion of magnetic sensors, rendering the topic very special in terms of size of sensors and distance to the field source. The sample space for an interpretation of the generated signal is likewise very limited usually being binary. For tape or hard drive read heads, the magnetic field strengths are easily on the order of mT at the employed distance of only several nm above the recording media [KL05].

All these applications have in common that the magnitude of the detected magnetic field is not of prime importance, but rather absolute differentials or differentials towards calibrated values. The magnitudes of the fields can be engineered in a way to exceed any environmentally present noise by a sufficiently large margin. Even the frequency can, within limits, be pre-determined according to environmental noise, or vibration noise considerations, thus even lock-in techniques or closed loop detection of the field acting as marker can be employed in order to strongly harden a sensing system towards even harshest industrial environments [Tum13].

1.1.2 Natural or Unknown Magnetic Signals

Much more challenging is the application of magnetic field sensors to naturally occurring or at least non-controllable magnetic signals of low frequency of which the prime concern is the determination of its magnitude and direction. These applications require the most sophisticated of magnetic sensors where noise is minimum and sensitivity maximum, in short the LOD needs to be as good as possible.

Usually, especially in geomagnetic surveys all components of the static earth magnetic field are of interest, making vector sensing necessary. On the other hand spatial resolution and thus sensor size is a relaxed requirement in these applications. The largest component of earth's magnetic field in equatorial regions is horizontal and amounts to about 30 µT or 300 mOe, this strength can locally deviate strongly, in Kiruna Sweden, magnetite ore leads to a very strong vertical magnetic field of up to 360 µT [Rip00].

Whereas the daily variations of the magnetic field are on the order of 10 ... 100 nT. MAD (Magnetic Anomaly Detection) is a technique where perturbations in earths' magnetic field caused by ferromagnetic objects are registered. Large structures such as ships or submerged submarines (U-boats) lead to shaping of the static earth magnetic

field due to a much higher magnetic permeability than their natural surroundings. These magnetic perturbations enable knowledge about the position and furthermore may even emit a specific magnetic signature mainly from its hull, but also from aboard machinery and equipment [Hol08]. This technique can be applied from great distances such as aircraft, making it especially interesting for the purpose of military reconnaissance [Hir+01]. Detection of UXO (Unexploded Ordnance) is an additional area of MAD [But03]. Further techniques relying on perturbations in earth magnetic fields are geomagnetic surveys for mineral exploitation [Rip00]. Different fall-off rate characteristics of objects producing magnetic stray fields can be identified, short or distant objects pose a dipole character and thus decay rather strongly with about $\frac{1}{r^3}$, r being the distance to the source. A classic dipole source would be a small wire coil at some distance or the human heart. A magnetic monopole, practically existent i.e. in a case of a long pipeline, with its ends separated at much greater distance than a magnetic sensor to one of them, decays approximately by $\frac{1}{r^2}$. Ultimately, for an infinitely long electrical conductor, the magnetic field only decays by $\frac{1}{r}$ [Bre73]. One ton of Iron produces a magnetic field of about 1 nT a distance of 40 m. The most widespread application of natural field detection is probably a single chip solution magnetic compass serving the purpose of navigation, nowadays present in any smart hand-held device. The earth's field horizontal magnitude being rather large, a noise floor of tens of nT is already sufficient for a precise magnetic compass.

Traditionally magnetocardiography (MCG) and the even more challenging magnetoencephalography (MEG) is performed exclusively by SQUID devices. Chosing the magnetic component instead of the long established electrical component promises to give deeper insight into cardiological questions, eventually the combination of ECG and MCG is anticipated. Especially in cases where multiple dipoles within the human body exist, may be invisible to surface potentials on the skin recorded by ECG, measuring the magnetic field emitted from the heart (MCG) measures vector information at a given point above the skin [NM92]. The specific conductivity, especially of lung tissue [MP95] between source and sensor are not expected to perturbed the magnetic signal, because the human body has a magnetic permeability very close to that of vacuum [NM92]. The magnetic component of brain waves, which was first measured by Cohen et. al. in 1968 [Coh68] using a large cored search coil with 1 million windings. These brain waves are on the order of 70 fT, making such signals three orders of magnitude smaller than those in MCG, which pose the largest human signals with peak amplitudes of about 100 pT. A compilation of various sources of human biomagnetic signals, along with their approximate bandwidths and amplitudes can be seen in figure 1.1 on the facing page. Acquiring patient data from the emitted magnetic fields is especially convenient for quick screening of many patients, as it is contact-less. MCG

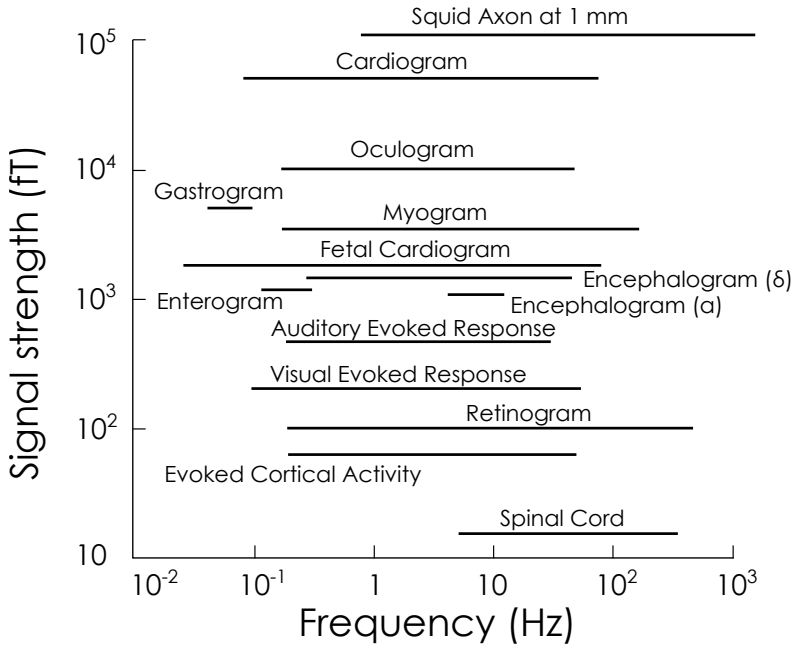

Figure 1.1: Double logarithmic plot of biomagnetic signals, their approximate bandwidth and amplitude ranges. The human heart cardiogram being by far the strongest source of magnetic fields of human origin. Adapted from [Wik95].

technology without the need for a magnetically shielded room could lead to great benefits in daily patient monitoring. Heart rate, heart variance etc. could be monitored by smart mattresses equipped with multiple sensors, on which patients merely need to lie on.

1.1.3 Available Sensor Technology

According to a market analysis of Frost & Sullivan 2005, about 50 % of the global magnetic sensor market were shared by not too cost sensitive markets of Automotive and Industrial, nearly the same amount is taken by the extremely cost sensitive market segment Computer Technology. High precision/reliability markets such as aerospace/defence and medical only share about 12 % of the total sensing market.

Figure 1.2 on the next page classifies available magnetometer technology in three categories, whereas category 1 contains the devices of lowest precision, usually not used for precise determination of a field amplitude, but more in thresholded switching applications and current measurements as described in section 1.1.1 on page 2. The fields in this category are all greater than the earth magnetic field, hence no special care needs to be taken [LE06]. This sensor market is the largest, lowest precision and most cost sensitive. It is dominated by Hall effect sensors, which score by very small sizes [LE06]. Magnetoresistive sensor technology (xMR) takes a huge market share in magnetic recording branch. For this market, device size on the order of nanometers is of highest importance, the fringing fields from perpendicular recording media are on the order of tens of mT at typical flying height of 5 nm [KL05]. Additionally the sample space for these sensors is essentially binary, thus a much higher noise can be tolerated without impeding performance. A comprehensive review on low noise xMR sensors for non-recording applications is given by [Zhe+19]. Category 2 poses an intermediate range where precision is necessary down to about 10 ... 100 nT, making precise yet cheap magnetic compasses for consumer goods possible. The *LIS3MDL* of *STmicroelectronics* is a low cost magnetic compass for consumer applications based on the TMR effect, offering a best case resolution of 300 nT, the same specification is given for the newer *LSM303AGR* based on the AMR effect which features three axis acceleration as well as three axis magnetic compassing. By using the great benefit of Hall technology being monolithically integrable into silicon, *Asahi Kasei Microdevices* offers a three axis Hall-based consumer grade compass *AK09918* showing similar resolution as above. *Aichi Steel* of Japan markets a fully integrated three axis magnetic compass *AMI306R* based on the MI effect, showing resolution also on the order of several 100 nT. All of these quoted products have a volume unit price of about one dollar.

Between category 2 and the most precise category 3 there are medium volume produced MI as well as AMR devices available at several tens of dollars which combine small form factor with precisions well below $150\,\mathrm{pT}/\sqrt{\mathrm{Hz}}$ at 10 Hz [Stu+05] [Zim+05]. *HMC1001* of *Honeywell* is an AMR sensor and the *MI-CB-1DH* of *Aichi Steel* a commercial MI sensor, both precision devices.

Category 3 poses stringent requirements on magnetic field precision and is in most cases required to operate under shielded conditions as the dynamic range of even the best

sensors is limited. Biomagnetic measurements require detection limits of 10 fT...100 pT, see figure 1.1 on page 5. For these very sensitive measurements of biologic MEG and

	1 nT		100 µT
	Category 3 High Precision	**Category 2 Medium Precision**	**Category 1 Low Precision**
Definition	Measuring field gradients or differences due to induced dipole moments (in Earth's field) or other natural dipole moments	Measuring perturbations in the magnitude and/or direction of Earth's field due to induced or permanent dipoles	Measuring fields stronger than Earth's magnetic field
Major Applications	Magnetocardiography (MCG) Magnetic anomaly detection (MAD) Magnetoencephalography (MEG)	Magnetic compasses Munitions fuzing Mineral prospecting Traffic control	Non-contact switching Position sensing Current measurements Magnetic memory readout
Most common Sensor	SQUID gradiometer Optically pumped magnetometer	Search-coil magnetometer Flux-gate magnetometer Magnetoresistive magnetometers (xMR)	Hall-effect sensor Magnetoresistive magnetometers (xMR) Search-coil magnetometer

Figure 1.2: Three principal categories of magnetic field sensors based on their precision and typical applications. Adapted from [LE06].

MCG signals the SQUID (Superconducting Quantum Interference Device) is state of the art, unfortunately even in a HTS (High Temperature Superconductor) version it is required to operate under liquid nitrogen conditions (77 K), this is its main disadvantage, and inhibits widespread use. In epilepsy treatment HTS SQUIDS find some use for the localisation of seizure foci [Pfe+20]. Nevertheless they pose a great tool for medical studies, despite their high complexity and operational efforts. Non-HTS SQUID versions prove the most sensitive, exhibiting noise floors of about $250\,^{\mathrm{fT}}/\sqrt{\mathrm{Hz}}$. However, they also pose the most expensive and complex to operate due to the required liquid Helium cooling for operation at 4.2 K [Dru95].

Induction coil sensors are very simple, yet effective low power magnetic sensors [PG09]. Their very low noise is only determined by 1/f-noise and thermal magnetisation fluctuations, as the system is completely passive as opposed to modulated sensors as fluxgates or ME sensors, see section 1.2.2 on page 21. A very comprehensive review on induction coil sensors is given by Tumanski in [Tum07]. The main drawback is a large sensor size and weight, due to coils consisting of several (ten) thousand windings around a usually rather macroscopic (often ferrite) core, leading to inductances of several Henrys. As a consequence search coil sensors achieve low spatial resolution [Zim+05], which is of no concern regarding fields emitted from huge sources such as in space observations [Rou+08] or geomagnetic research. These features make them rather expensive and bulky due to large amounts of copper conductor and core material, rendering them unattractive for large scale production. Measuring low frequencies is an inherent problem, as required by the induction law, DC fields do not induce currents, very low frequencies down to 20 mHz have been measured [PG09]. At 1 Hz a value of about

$20\,\mathrm{pT}/\sqrt{\mathrm{Hz}}$ was found [PCP00]. A commercially available search coil magnetometer of *MEDA Inc.*[1] is the *MGCH-2*, which shows $2.5\,\mathrm{pT}/\sqrt{\mathrm{Hz}}$ at 10 Hz, it weights 715 g and is a 33 cm by 2.5 cm long cylinder.

Fluxgates rely on the fact that ferromagnetic hysteresis loops are non-linear and symmetric [Tum11]. The simplest sensor is composed of a high permeability core material with an excitation and usually a separate sense winding around it, serving for signal pick-up [Rip03]. By periodically driving the core material into saturation, the incremental permeability μ of the core material is dynamically modulated, the uneven symmetry of the magnetisation curve leads to only odd harmonics of the drive signal appearing in the sense winding [Tum11]. Figure 1.3 illustrates the working principle

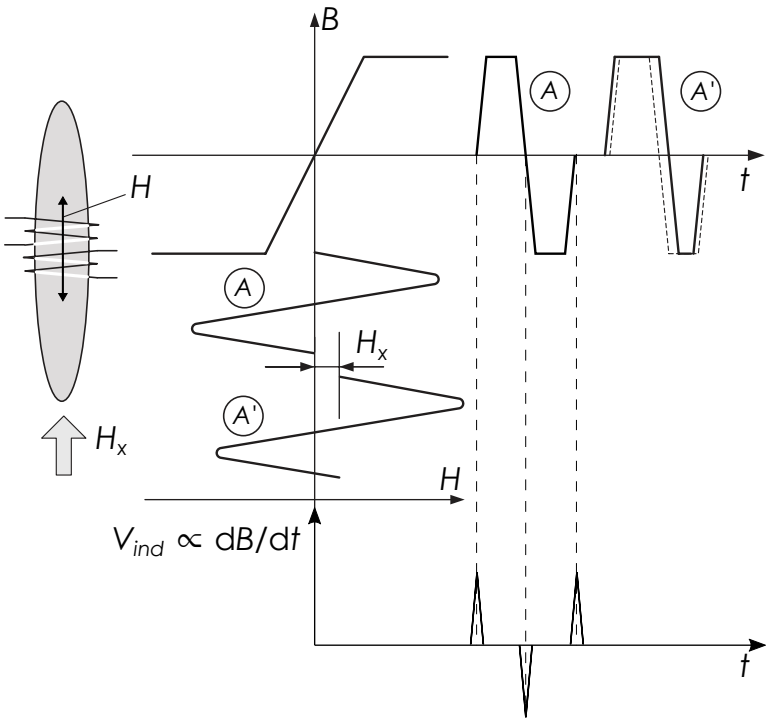

Figure 1.3: The fluxgate magnetometer principle. A soft magnetic core material is periodically saturated by a large magnetic field H, producing a symmetric output, case A. Upon presence of an external magnetic field H_x this symmetry is broken, making the top branch stay saturated longer, case A'. This asymmetry consequently changes duration between adjacent voltage pulses $^{dB}/_{dt}$ in the pickup coil, giving rise to even harmonics generated in frequency domain. Adapted from [Tum11].

of fluxgate sensors, any small field H_x applied along the magnetising direction shifts this dynamic situation and leads to asymmetry in the magnetisation loops, causing even harmonics produced in the frequency domain. Usually the second harmonic in the sense coil output spectrum is of interest, as its amplitude depends linearly on the external magnetic field. By using a phase sensitive detector (PSD) set to twice the

[1] Macintyre Electronic Design Associates, Inc.

excitation frequency, a DC voltage proportional to the applied external field is generated [Pri79]. A fluxgate neatly constructed of two rod cores individually wound with excitation windings was first proposed by Vacquier et. al. in 1947 these excitation windings oppose each other and are surrounded by a common sense winding. The opposing fluxes of the excitation windings lead to perfect [2] cancellation of the excitation flux, leading to a clean output spectrum in which only the external field has an influence, by subtraction and addition onto the hysteresis loops of the two cores [Tum11]. Fluxgates are available in two fundamentally different constructions, parallel type and orthogonal type [Pri79]. In Europe, *Stefan Meyer Instruments* as well as *Bartington* are suppliers of commercial fluxgates. The *FL-1* of *Stefan Meyer Instruments*, offers a noise of $20\,\mathrm{pT}/\sqrt{\mathrm{Hz}}$ at 1 Hz and the *Bartington Mag-03*[3] achieves $6\,\mathrm{pT}/\sqrt{\mathrm{Hz}}$ at 1 Hz being physically larger, about 5 cm by 2 cm diameter, cylindrical.

Apart from traditional parallel [4] fluxgates using one or more single rod cores or a ring core and at least two coil windings. Orthogonal [5] fluxgates operate using an excitation current running through its core, producing the orthogonal drive field by ampere's law [GHM16]. An orthogonal type fluxgate typically consists of an amorphous material which is bent to a slender U-shape or π-shape within a pickup coil, thus ensuring cancellation of the excitation signal. An advanced example of such an orthogonal fluxgate is shown in figure 1.4 on the following page, where two 125 µm diameter wires soldered to a PCB form the core, contained in about 1800 windings of wire. The ferromagnetic wires carry a modulated unipolar AC+DC current which creates a time varying axial magnetic field [GHM16]. Because of unipolar drive signals these fluxgates operate at their fundamental frequency, unlike second harmonic operation exploited by the traditional type [Jan+19]. Especially orthogonal fluxgates are emerging in recent years, triggered in 2002 by [Sas02] followed by others, because they are quite compact and reach impressive LODs [Jan+19]. A main drawback seems to be strong offset drift [Jan+19] and their high power consumption on the order of 100 mW excluding any low noise amplification. Optically pumped magnetometers (OPMs) have gained a lot of attention during the last years, as they are commercially available and easy to operate, though still expensive. *QuSpin* manufactures commercial devices showing noise floors of 15 fT within 3 ... 100 Hz. The ambient residual field needs to be lower than ±50 nT, thus these sensors already require quite a good magnetic shielded room in order to operate. Nevertheless even a small residual field needs to be compensated for, using electronic compensation coils. A change of ambient field of 1 nT requires such recalibration [Sha+18]. For the most sensitive open loop type, the dynamic range

[2] for adequate construction and calibration
[3] In a special low-noise version, $< 10\,\mathrm{pT}/\sqrt{\mathrm{Hz}}$ at 1 Hz otherwise.
[4] The external magnetic field and the excitation field are parallel to each other.
[5] The external magnetic field and the excitation field are orthogonal to each other.

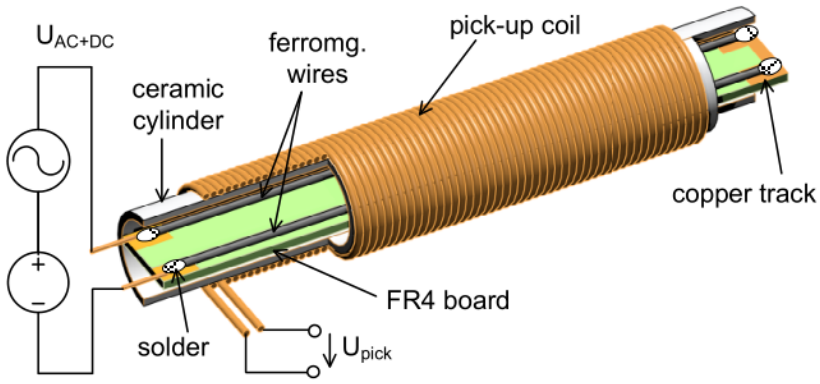

Figure 1.4: Orthogonal fluxgate, two amorphous wires soldered to a PCB (FR4), act as core. They are magnetically modulated by opposite currents (created by U_{AC+DC}) flowing through them. The coil generates signal U_{pick}. An external field is to be applied in axial direction. [Jan+19] ©2019 IEEE

after compensation and calibration is ±5 nT and the bandwidth is inherently limited to below 200 Hz [KST14]. In literature this sensor type is often stated as scalar type, but by modulation schemes, it is possible to obtain a directivity - at the cost of precision. Special models of OPMs, labeled total field OPMs are available, which typically have degraded performance to about $1\,\mathrm{pT}/\sqrt{\mathrm{Hz}}$. The employed laser source unfortunately has a limited lifetime, leading to required maintenance after several tens of operation hours. Thermal fatigue, by thermal cycling from ambient to about 55 °C is another concern.

Giant magnetoimpedance (GMI or MI) sensors are constructed quite similar to orthogonal fluxgates in which an amorphous ferromagnetic wire experiencing circular magnetic anisotropy is pulsed by an excitation current and two coils are wrapped around it [Hon02]. Typically high excitation frequencies are employed in order to exploit the skin effect, i.e. the effective cross-section of a conductor diminishes towards its skin (its outer shell) at high frequencies. This skin depth in general depends on the resistivity and the frequency, in ferromagnetic materials additionally on the magnetic permeability. Thus in GMI, the AC impedance is a strong function of the external magnetic field, modulating the permeability and by that the electrical impedance [Rip00]. Recent research has demonstrated noise floors below 1 pT for frequencies above 1 Hz [UM20]. There is a plethora of MI effects which seem constructively similar but physical effects at completely different frequencies are exploited.

Figure 1.5 on the next page gives an overview of available sensors and their respective dynamic range, irrespective of frequency or other limitations. The most relevant ones in terms of an existing market were discussed in further detail. Strongly depended on an application and its specific requirements towards sensitivity, bandwidth, dynamic range, linearity, spatial resolution, energy consumption and cost.

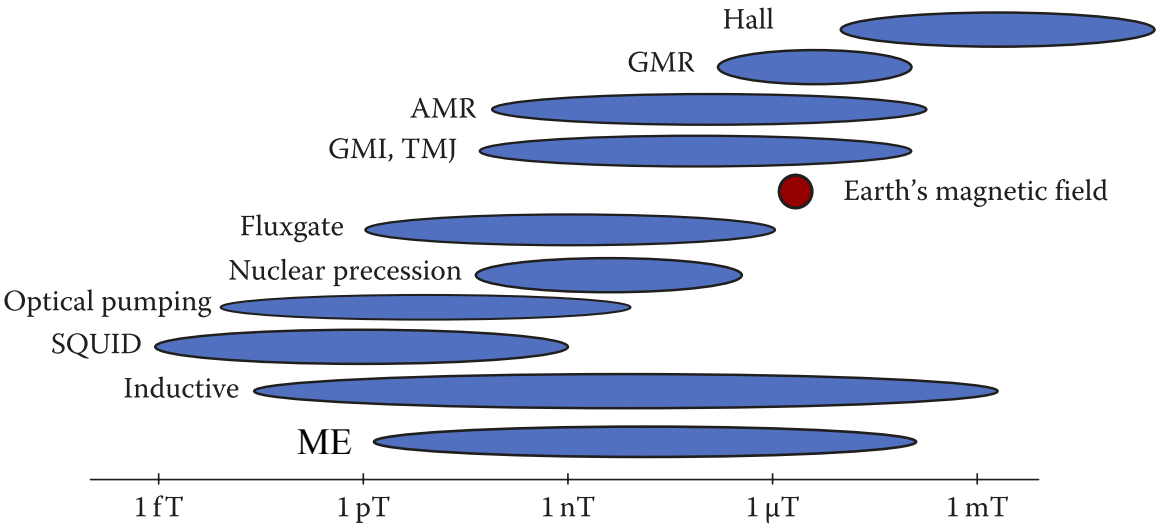

Figure 1.5: An overview of established sensors and their approximate range of field amplitudes. Magnetoelectric (ME) sensors are added for comparison. Adapted, edited, updated from [Tum11].

Sensors based on thin film Magnetoelectric composites are most promising for device application, they form the core matter of this thesis and are a subject of active investigations worldwide. The following sections go into further detail.

1.2 Magnetoelectricity in Composite Materials

Single phase magnetoelectric materials pose an interesting topic for research, unfortunately the achievable effect size is very low (order of $10\,^{\mathrm{mV\,Oe}}/_{\mathrm{cm}}$) [Ou-+18], making those materials unattractive for short to medium term practical application as magnetic field sensors. Figure 1.6 on the following page schematically shows single phase multiferroics being orders of magnitude less polarisable, electrically and magnetically, than composites [LS11]. Magnetoelectric composites remedy these shortcomings by essentially bringing a piezoelectric and a magnetostrictive constituent in physical contact, this can be done using several connectivity routes shown in figure 1.7 on the next page [SSP14]. However, practically route a) and route c) pose rather tedious compromises towards composite engineering. Using cylinders inside a matrix requires sophisticated aligning strategies of the micro cylinders, using route c) is complicated by particle agglomeration, clogging or incomplete dispersion issues, finally leading to an overall either magnetically or electrically polarizable composite, consequently preventing a high ME effect. From a practical point route b) enables maximum design freedom, as virtually

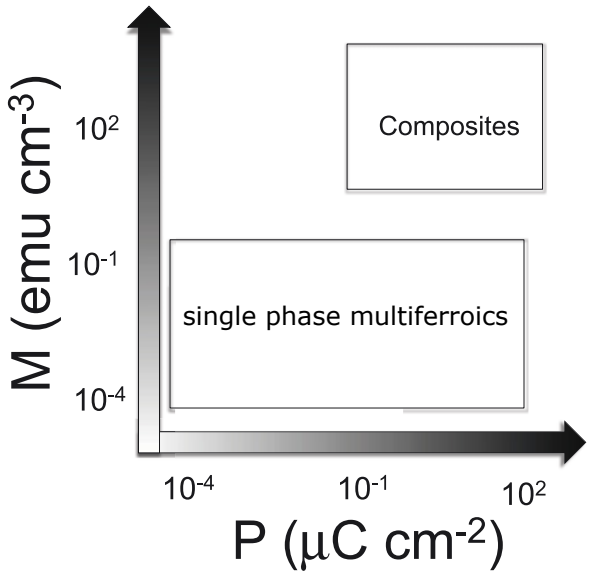

Figure 1.6: Electric and magnetic polarisation in composite and single phase multiferroics, schematically. Edited and reprinted with permission, [LS11].

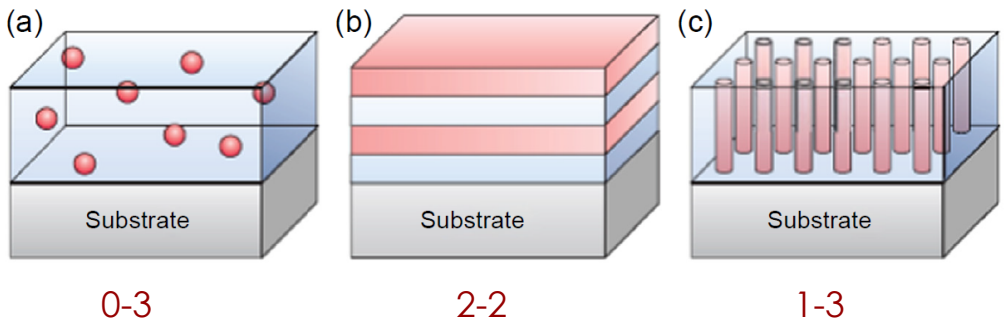

Figure 1.7: Connectivity schemes in magnetoelectric composites. Numbers denote dimensions of phases. a) 0D magnetic material dispersed in a matrix of piezoelectric material. Note that this scheme does not rely on magnetostriction b) Laminate composites, consisting of at least one 2D layer of magnetostricitve material and one layer of piezoelectric material. c) Pillars of one phase aligned in a matrix of the other phase. [SSP14].

any material combination can be laminated together, without the constraints associated with one material acting as the matrix component [CP11]. This can take several forms, one is to macroscopically bond ME laminates using epoxy glue. In this field, Viehland et. al. established a vacuum bagging technique in order to minimize losses at the interface [She+14], this form of bulk 2-2 magnetoelectric laminates is rather popular [Zha+08a], [CP11]. The other main type of laminate composites is of thin film nature, whereas either a magnetostrictive film is deposited onto a sufficiently smooth piezoelectric substrate [Wu+11] or a sillicon wafer is used as a substrate material to host both active phases forming the thin film ME composite [Nan+13], [Nai+13].

Obviously, thin film types offer all advantages associated with thin film cleanroom processing, such as high volume production, good reproducibility, low unit cost, high utilisation of materials. On the contrary it seems that bulk composites can be advantageous in terms of performance [Don+06b], [Mer92] this may be directly related to more available magnetic volume leading to higher magnetoelectric effect [Sri+01]. This leads to more magnetic flux lines being confined into the sensor structure, thus leading to higher signal but likewise to lower spatial resolution. Early studies of Bittel and Storm state that ferromagnetic noise in general is inversely proportional to the volume of the employed magnetic material [BS70] making large layer dimensions beneficial in terms of noise, this was also discussed by [Sal18]. A selection of published performance values with respect to the employed magnetic volume is tabulated in table 1.1. The anticipated use of ME composites as sensors for biomedical imaging poses a strong constraint on the size and thus the achievable spatial resolution the sensors.

A trend, indicating that large ferromagnetic volumes are more sensitive is apparent, whereas the dependency towards volume is clearly not linear. According to Koch et. al. [KDG99] the noise present for a magnetic material in equilibrium magnetisation is given by equation (1.1).

$$S_M^{eq} = \frac{4k_B T \chi''(\omega)}{\Omega \omega} \tag{1.1}$$

where k_B, T, χ'',Ω and ω is Boltzmanns' constant, the temperature, the imaginary part of the magnetic susceptibility the magnetic volume and the measurement frequency. Consequently the tabulated data on the one hand gives rise to encouraging results in terms of detection limits on the other hand most highly sensitive sensors published are physically too large to be employed for any biologic application. Biological field sources generate gradient fields even at small distances, which require sensors always smaller than those gradients in order to deliver meaningful spacial data. Apart from being used as a sensor, where an external magnetic field ultimately produces a proportional voltage, magnetoelectric composites have additional anticipated uses. Acoustic antennas, which can emit and receive frequencies at drastically smaller form factors

than traditional electric loop antennas [Nan+17], [Don+20]. Usage as a gyrator, an impedance converter was anticipated by the group of Viehland [Zha+09].

Table 1.1: Low frequency performance of various integrated magnetic sensors based on ferromagnetic materials.

Author	Year	Material	Type	Magnetic volume (m^3)	LOD/Resolution	Frequency (Hz)	Reference
Mermelstein	1992	Metglas	Conv. ME	25×10^{-9}	$7.9\,\mathrm{pT}/\sqrt{\mathrm{Hz}}$	1	[Mer92]
Li	2013	Vitrovac 7600F	Direct ME	128×10^{-9}	$30\,\mathrm{pT}/\sqrt{\mathrm{Hz}}$	1	[Li+13]
Fang	2015	Metglas	Direct ME	300×10^{-9}	$900\,\mathrm{fT}/\sqrt{\mathrm{Hz}}$	30	[Fan+15]
Chu	2017	Metglas	Direct ME	37.5×10^{-9}	$135\,\mathrm{fT}/\sqrt{\mathrm{Hz}}$	DC	[Chu+17a],[Chu+17b]
Mermelstein	1987	Metglas	Conv. ME	12.5×10^{-9}	$120\,\mathrm{pT}/\sqrt{\mathrm{Hz}}$	DC	[MAD87]
Annapureddy	2017	Nickel	Direct ME	288×10^{-9}	$120\,\mathrm{pT}/\sqrt{\mathrm{Hz}}$	5	[Ann+17]
Das	2009	Metglas	Direct ME	112.5×10^{-9}	$300\,\mathrm{pT}/\sqrt{\mathrm{Hz}}$	0.6	[Das+09]
Zhuang	2015	Metglas	MFC	360×10^{-9}	$250\,\mathrm{pT}/\sqrt{\mathrm{Hz}}$	1	[Zhu+15c]
Zhuang	2015	Metglas	MFC/EFC	120×10^{-9}	$90\,\mathrm{pT}/\sqrt{\mathrm{Hz}}$	1	[Zhu+15a]
Wang	2011	Metglas	Direct ME	120×10^{-9}	$10\,\mathrm{pT}/\sqrt{\mathrm{Hz}}$	1	[Wan+11]
Kirchhof	2015	FeCoSiB	DeltaE	6×10^{-12}	$140\,\mathrm{pT}/\sqrt{\mathrm{Hz}}$	20	[Zab+15]
Kittmann	2018	FeCoSiB	SAW	3×10^{-12}	$300\,\mathrm{pT}/\sqrt{\mathrm{Hz}}$	10	[Kit+18]
Butta	2019	CoFeSiB	Orth. Fluxgate	4.3×10^{-9}	$600\,\mathrm{fT}/\sqrt{\mathrm{Hz}}$	1	[BS19]
Janosek	2019	CoFeSiB	Orth. Fluxgate	2×10^{-9}	$1.1\,\mathrm{pT}/\sqrt{\mathrm{Hz}}$	1	[Jan+19]
Malátek	2010	CoFeSiBCr	GMI	1.9×10^{-9}	$17\,\mathrm{pT}/\sqrt{\mathrm{Hz}}$	1	[MK10]
Yabukami	2009	CoNbZr	GMI	2.5×10^{-9}	$1.35\,\mathrm{pT}/\sqrt{\mathrm{Hz}}$	1	[Yab+09]
Kraus	2008	CoFeSiBCr	GMI	3.2×10^{-9}	$5.9\,\mathrm{pT}/\sqrt{\mathrm{Hz}}$	1	[KMD08]
Zimmermann	2005	Permalloy	AMR	10×10^{-15},[6]	$50\,\mathrm{pT}/\sqrt{\mathrm{Hz}}$	10	[Zim+05]
Cardoso	2014	$Co_{93}Zr_3Nb_4$	TMR	50×10^{-15}	$300\,\mathrm{pT}/\sqrt{\mathrm{Hz}}$	1	[Car+14]
Nan	2013	FeGaB	DeltaE	6×10^{-15}	300 pT,[7]	DC	[Nan+13]
Hayes	2018	FeCoSiB	Conv. ME	100×10^{-12}	$70\,\mathrm{pT}/\sqrt{\mathrm{Hz}}$	10	[Hay+19]
Schell	2020	FeCoSiB	SAW	2.3×10^{-12}	$70\,\mathrm{pT}/\sqrt{\mathrm{Hz}}$	10	[Sch+20]

[6]This is an estimated value.
[7]Note this value refers to resolution.

1.2.1 Direct Magnetoelectric Effect

The direct magnetoelectric effect in composites occurs by mechanical coupling of a magnetostrictive material (typically of ferromagnetic type) to a piezoelectric material (of piezoelectric or poled ferroelectric material). Upon application of an external field the (Joule) magnetostrictive material deforms (at constant Volume) thus creating a strain ϵ, which is transfered by means of a coupling effectiveness (or coefficient k) to the piezoelectric phase where it creates a stress σ, thus leading to charge generation by the direct piezoelectric effect. This generated charge in turn is amplified and quantified as the magnetoelectric voltage coefficient α_{ME}, normalized by the piezoelectric layer thickness as well as the magnitude of the exciting AC magnetic field. The basic concept is given in Figure 1.8, three parameters are identified, left to be optimised by the engineer.

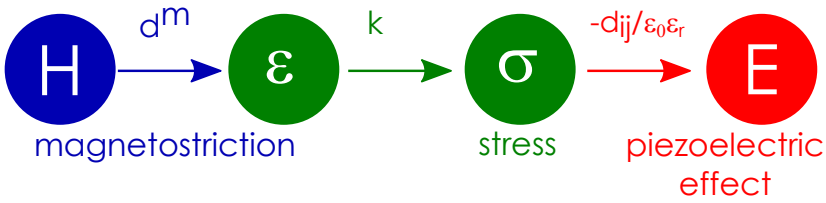

Figure 1.8: A portion of the famous Nye diagramm. Schematically showing the direct ME effect. d^m beiing the piezomagnetic coefficient, which connects the magnetic field H with strain ϵ, k the coupling and $-\frac{d_{ij}}{\epsilon_0 \epsilon_r}$ describes the piezoelectric charge generated.

Equation (1.2) gives the full expression for the magnetoelectric voltage coefficient.

$$\alpha_{ME} = \frac{\partial P}{\partial H} = \frac{\partial P}{\partial \sigma} \frac{\partial \sigma}{\partial \lambda} \frac{\partial \lambda}{\partial H} \tag{1.2}$$

Where P and H denote piezoelectric polarisation and magnetic field, σ and λ are the piezoelectric stress and the magnetostrictive strain, respectively. In order to obtain an overall strong ME effect, the magnetostriction λ, the coupling between the phases k as well as the direct piezoelectric effect $-d_{ij}/\epsilon_0 \epsilon_r$ should be maximum. Using composite materials enables nearly free optimisation of those parameters, without compromising others, this is a unique advantage [GDS08]. Magnetostrictive response is at maximum if a magnetically hard axis is present, transverse to which a magnetic field should be applied enabling saturation magnetostriction λ_s to be reached. This hard axis magnetostriction is by definition quadratic with the magnetisation M of the material $\lambda \propto M^2$ [CG09]. The linear piezomagnetic coefficient d^m is the derivative of the magnetostrictive response, which needs to be large in order to obtain a high linear magnetoelectric response from the system. Relating the actual deformation per field

is the key parameter to high magnetoelastic coupling as required for a ME magnetic field sensing device.

To elaborate briefly; the alloy with the largest known saturation magnetostriction is Terfenol-D ($Tb_{(1-x)}Dy_xFe_2$), which shows around 1400 ppm [SSP14] at a saturation field of 200 mT or 2.000 kOe [Pri+07], very simply assuming linear behavior in one quandrant of the magnetostriction curve yields a value of $\frac{1400\,\mathrm{ppm}}{2000\,\mathrm{Oe}} = 0.7\,{}^{\mathrm{ppm}}/_{\mathrm{Oe}}$ for the linear piezomagnetic coefficient. For the case of amorphous FeCoSiB, considering a saturation magnetostriction of about 30 ppm at around 12 Oe, this slope amounts to $\frac{30\,\mathrm{ppm}}{12\,\mathrm{Oe}} = 2.5\,{}^{\mathrm{ppm}}/_{\mathrm{Oe}}$. This oversimple estimation makes FeCoSiB already 3.5 times the value available with Terfenol-D, underlining the importance of the linear piezomagnetic coefficient for the direct magnetoelectric effect, unlike the achievable saturation magnetostriction.

Introducing a bias magnetic field along the hard magnetisation axis is the most straightforward route to achieving this linearity, as shown in figure 1.9 on the following page, a measured example of the magnetostriction along with the piezomagnetic coefficient of a 4 µm thick annealed FeCoSiB film on a 300 µm Sillicon substrate. The magnetoelastic phase reveals four maxima, giving rise to four working points in the piezomagnetic response, in the vicinity of ±2 Oe . Very high initial permeability on the order of 20 000 makes the piezomagnetic coefficient high at such low bias fields. A pronounced hysteresis is visible towards the zero crossing, making a positive bias field exhibit maximum d^m after negative saturation and vice-versa. This phenomena stems from local micromagnetic effects emerging from the edges of the magnetostricvtive layer [Urs+14].

The magnetoelectric coupling coefficient k bundles all coupling effects between the magnetic and the electric material phases. Looking at low frequencies, near DC the direct magnetoelectric effect is expected to be vanishingly small. This is caused by interfacial relaxation of stress between the phases as well as finite DC resistance of the piezoelectric layer, viewed as a parallel plate capacitor [AP12] causing a constant "bleed" of available charge resulting in very low performance at DC.

Ferroelectric thin film materials like lead zirconate titanate (PZT) exhibit spontaneous polarisation which is, given polycrystalline nature, randomly oriented after deposition [TM04]. A metallic seed layer is used to establish a texture in the material [EP01]. Thus, in order to be successfully employed as sensing element these ferroelectric films need to be poled after deposition at elevated temperature and high field strength on the order of ${}^{\mathrm{MV}}/_{\mathrm{m}}$ [Pio+13] strongly enlarging the direct piezoelectricity and thus the direct ME effect. This ferroelectric poling is fragile, it can be lost when heating the material above its curie temperature or by applying high reverse field strengths [MH08]. Piezoelectric materials such as aluminium nitride (AlN) and zinc oxide (ZnO) hold a

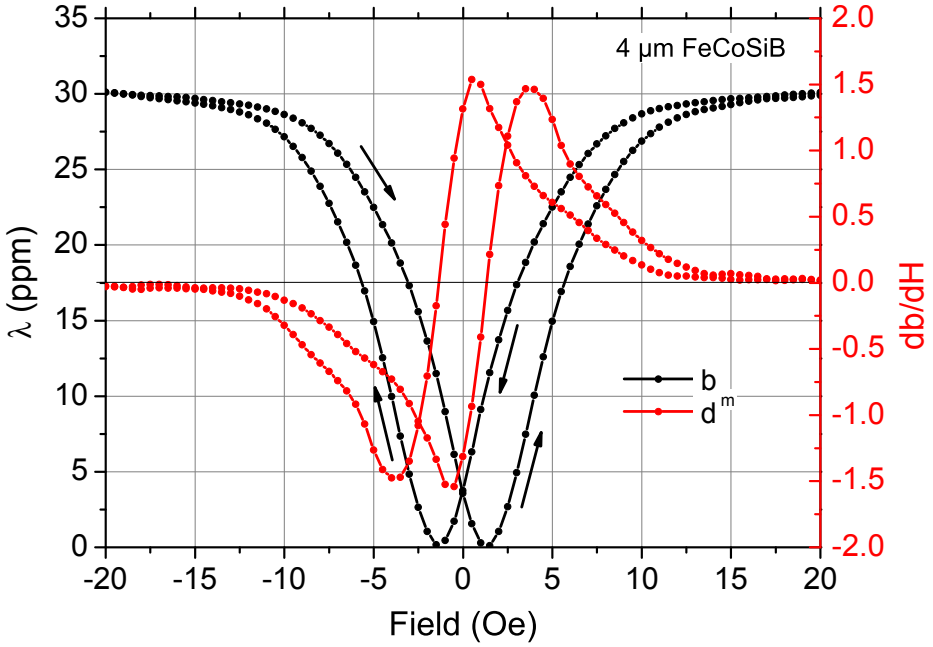

Figure 1.9: Magnetostriction measurement. Showing the magnetostriction λ of a hard axis magnetisation of an annealed FeCoSiB thin film cantilever sample. The linear piezomagnetic coefficient d^m is separately calculated for the same sample, giving rise to four magnetoelastic working points using this material.

polar crystallographic axis which determines the piezoelectricity, thus strong texturing during deposition is of prime importance for obtaining high piezoelectricity [Yar+16b].

Next to the piezoelectric parameters ($\epsilon_{ij,f}$ and $d_{ij,f}$)[8] the loss tangent ($tan\,\delta$) typically likewise enters equations for signal-to-noise ratio [Yar+16b], [Mur97]. Piezoelectric parameters show about an order of magnitude larger values in well poled ferroelectric materials compared to well textured piezoelectric materials [TM04]. Losses on the contrary, are typically one order of magnitude higher for ferroelectric materials, caused by ferroelectric domains and associated hysteresis, which is absent in piezoelectric crystals [Mur97]. Thus both parameters have to be balanced in order to reach high electrical output using the direct ME effect.

Excited by a time varying magnetic field coinciding to a mechanical resonance of the composite can yield tremendous effect enhancements by two orders of magnitude and thus is the strongest contributor to strong ME coupling k. This time varying magnetic field is superimposed onto a stationary magnetic field in order to operate the composite in a working point of the piezomagentic coefficient. Figure 1.10 on the next page shows such a resonance, able to increase the effect strongly if the resonance frequency is matched precisely by an external magnetic AC field. The mechanical quality factor

[8] indices i, j denote the directions between which the respective coefficient is concerned. f denotes quantities obtained from thin films.

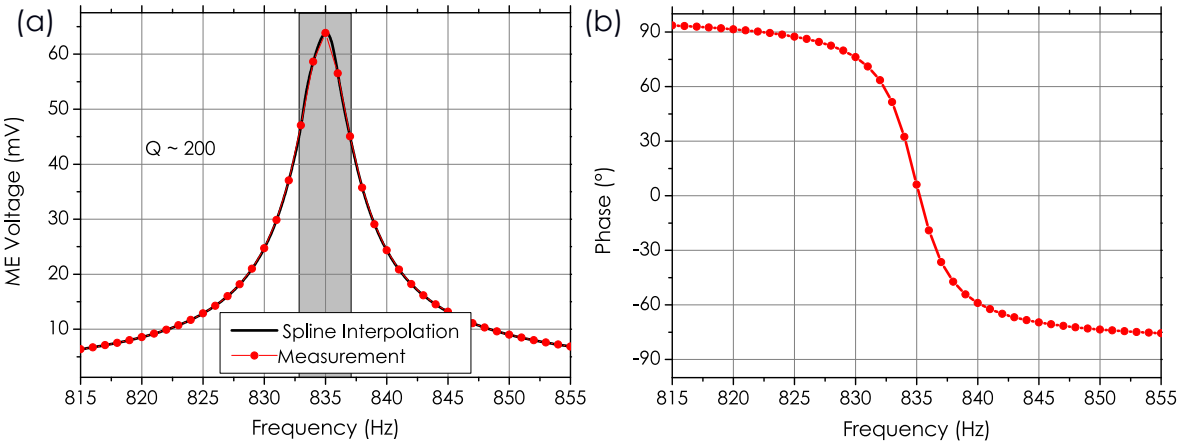

Figure 1.10: ME effect enhancement in mechanical flexural resonance and its phase (a) giving rise to sharp increase of V_{ME} in a narrow bandwidth, given by the quality factor Q of the resonator and its specific resonance mode excited. (b) at mechanical resonance frequency a phase reversal with respect to the exciting magnetic field occurs. This is characteristic for harmonic mechanical resonances.

Q determines the magnitude of effect enhancement by mechanical resonance. Furthermore, together with the mechanical resonance frequency it determines the bandwidth of the oscillator, see section 1.2.2 on page 22. Thin film composites are usually deposited on a substrate material, by definition of greater thickness than the films, this in a magnetoelectric sense passive chunk of material poses the largest contributor to the dynamic response of a thin film magnetoelectric oscillator. Figure 1.11 demonstrates the intimate linkage between an ME cantilever composite tip deflection at resonance to the generated ME voltage at resonance under static magnetic field.

The parameter k seems to be the most challenging to optimize, since it contains all losses occurring in the path of magnetostrictive deformation to charge generation. The direct piezoelectric effect, represented by the piezoelectric coefficient $d_{ij,f}$[9], concludes the chain taken from the Nye diagram in figure 1.8 on page 16. Obviously the same principal applies to this property, it should be linear, free of hysteresis and its magnitude should be highest possible. Highest values are obtained using ferroelectric materials like PZT[10], showing d_{33} values up to 130 pm/V, having easily an order of magnitude larger coefficients than the inherently linear non-ferroelectric materials such as ZnO $d_{33} \approx 6$ pm/V [TM04] and AlN $d_{33} \approx 7$ pm/V [Yar+16b]. Virgin ferroelectric materials experience strong hysteresis, as the name implies, in order to obtain a linear response towards applied electric fields or loads they need to undergo an electric poling procedure, covered later on. Piezoelectric materials, on the contrary have a crystallographi-

[9] the lowercase f indicates thin films

[10] this strongly dependend on composition, at the morphotrophic phase boundary a great increase in effect takes place.

cally built in polar axis, here best control over piezoelectric properties can be achieved by using single crystal materials, [Sre+12] [Sri+05] [Tur+18b], if available, PZT fibers [Don+06a], or strongly textured or grain oriented films [AP12] [Yar+16a].

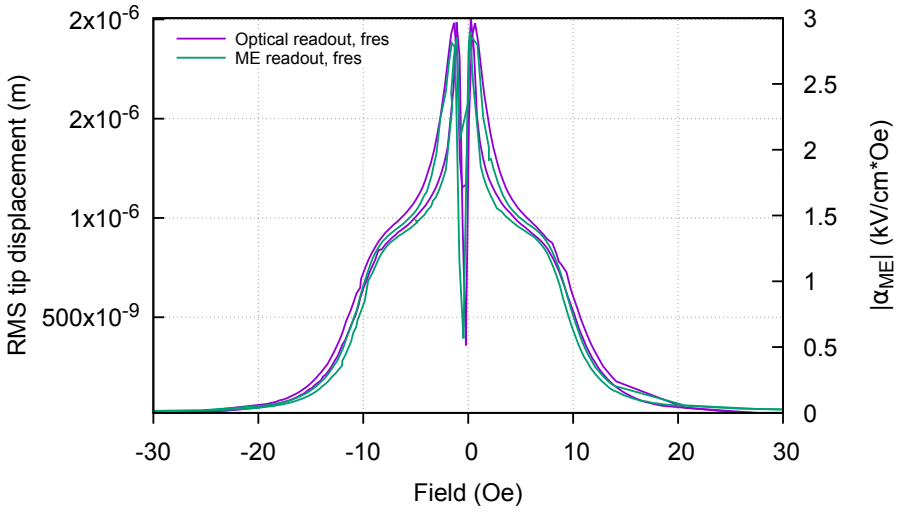

Figure 1.11: Measurements of optical tip deflection of an ME cantilever as well as piezoelectrically recorded ME voltage α_{ME}. This resembles a piezomagnetic measurement under resonance conditions, using the 1st flexural mode. With $H_{AC} = 3\,\mu\mathrm{T}$ and AlN as the piezoelectric phase.

The direct magnetoelectric effect in composites is a widely studied phenomenon, formed from bulk laminated materials [Zha+08b] down to microresonators made from all MEMS compatible methods [Mar+13]. A comprehensive outline on the direct magnetoelectric effect in thin film composites is to be found in [Yar17]. Despite being well studied, the direct ME effect has potential device applications in which a high sensitivity is required only within a tight bandwidth. Such an application is given for the purpose of magnetic particle imaging, where the narrow, sensitive resonance is utilised for harmonic components selection and detection [Fri+19]. Especially magnetoelectric devices relying on a boost in the coupling caused by exploiting mechanical resonance amplification can reach very large magnetoelectrically generated voltages [Kir+13]. For any device converting a magnetic field into an electric signal, whether for the purpose of magnetic field sensing [Tur+18a] of harvesting of stray magnetic fields for energy generation [Yar+19], the external magnetic field frequency needs to very closely match the mechanical resonance in order maximize the magnetoelectric α voltage coefficients and thus reach a high detectivity. When tailoring the mechanical resonance frequency of the composite for direct ME detection at low frequencies immediately conflicting goals arise. (a) Employing low order flexural resonances make the resonators physically larger or requires soft substrates such as polymers [Kul+14] exhibiting low mechanical quality factors. (b) As resonance frequency drops, the res-

onator is more susceptible to acoustic interferences [Ree+15] and 1/f-noise contribution is increased. Concluding, the direct ME effect is of great use in composite materials characterisation and materials exploration, its commercial use in magnetic field sensors is not yet reached. Hence why modulation, or active techniques successfully remedy limitations of the passive, direct ME effect, enabling prospective usage.

1.2.2 Active Operation or Modulation of Magnetoelectric sensors

Generally many modern sensors rely on modulation schemes, usually by switching the quantity of interest at a known frequency [Chi+97] [Gue+08], or applying an additional quantity at a higher frequency (a carrier, $f_{carrier}$ or f_{mod}), both routes lead to escaping all DC related trouble, such as 1/f-noise, DC offset, drift etc. [GB02]. In fact GMI sensors are intrinsically modulated [GHM16] by a much higher frequency signal than the one of interest, in order to exhibit large magnetoresistance effects. In fluxgates the second harmonic is demodulated, and its amplitude gives the actual sensor response towards external fields. Orthogonal fluxgates achieve offset cancellation by rapidly switching polarity of the bias field [Sas02].

As an example in magnetoelectric composites, magnetic modulation is performed by applying an AC bias field f_{mod} parallel to the measurement direction, whereas its frequency may be coinciding to a mechanical resonance, thus by amplitude or frequency modulation two sideband signals are created in the frequency domain [Jah+12], [Gil+11], [Pet+11]. If the carrier frequency f_{mod} is offset from resonance by the frequency of the field of interest f_{AC}, leading to the sum or difference sideband coinciding to the actual mechanical resonance frequency f_{res} [Jah+12], thus equation (1.3)

$$f_{res} = f_{mod} \pm f_{AC} \tag{1.3}$$

holds. A magnetically modulated operation of a magnetoelectric composite is very similar to the operation principle of fluxgates, differing only in terms of piezoelectric readout and excited mechanical resonance. These modulation techniques allow for significant 1/f-noise reduction as well as mechanical resonance enhancement by the mechanical resonance Q-factor, which leads to a further amplification of one of the sidebands. In order to apply this technique practically, a sweep of f_{mod} must occur, to keep the equation (1.3) satisfied. Jahns et. al. proposed a magnetic spectrum analyser [Jah+12] based on this technique which was implemented by Burdin el. al. [Fet+14], by using a sweep generator to constantly change f_{mod} and by this selectively acquire a wideband spectrum.

In principle these modulation techniques benefit from very high quality factors, but these will inherently limit the sweep speed to practically a few times $B = Q\frac{1}{f_{res}} = QT$.

Table 1.2: Dynamic range comparison of different benchtop data aqusision devices commonly used in the field of magnetoelectric composites and their dynamic reserve.

Type	Model	Dynamic reserve
Sound card	RME Audio, ADI-2 Pro FS	120 dB
Lock-In amplifier	Zurich Instruments, HF2LI	120 dB
Lock-In amplifier	Stanford Research, SR830	100 dB
Lock-In amplifier	Stanford Research, SR850	100 dB
Lock-In amplifier	Ametek, ST7265	100 dB
Spectrum analyser	Stanford Research, SR785	90 dB

For any oscillator to settle it takes at least Q oscillation periods T. Consequnetly when Q is very high, f_{res} should also be very high, in order to maintain high sensing bandwidth B. This approach of satisfying equation (1.3) on the previous page is only meaningful if the frequency of the signal of interest $f(H_{AC})$ is significantly larger than the bandwidth of the employed mechanical resonance mode, i.e. $f_{AC} > f(H_{AC})$. Otherwise the benefit by resonance amplification for one of the sidebands is negligible and excitation at the resonance itself is preferable.

The counterpart to this magnetic modulation scheme will employ an external electric field in order to remedy shortcomings associated with the technique, thus electrical modulation will be discussed in its most related form in the publication in section 2.

Depending on the form of such a modulation scheme, there are specific challenges associated with its benefits. Amplitude modulation leads to splitting of the power among the two generated sidebands [Jah+12], requiring some sort of amplification in order to account for this loss. Additional electronics are necessary for demodulation which need to be designed carefully in order not to introduce additional noise, usually this is done by at least one phase sensitive detector or simply analog switches [Rup+17]. Furthermore as the modulation field amplitude can be rather large, care has to be taken not to experience strong carrier feedtrough in the output spectrum, which may limit the available dynamic range provided by the demodulation circuit. In cases of dynamic range limiting carrier amplitudes, suppression schemes may be required, making electronics more complex and especially tedious [Dur+17].

Available bandwidth

Utilizing the direct ME effect in resonance (section 1.2.1 on page 16), the signal of interest is amplified by coinciding to a mechanical resonance frequency of an ME oscillator resulting in high sensitivity at precisely that frequency. In this scenario the exact sensitivity gain in resonance is given by the quality factor Q and is a direct trade-off

with available signal bandwidth B by equation (1.4);

$$\begin{aligned} B &= \frac{f_{res}}{Q} \\ B_{mod} &= \frac{f_{res}}{2Q} \end{aligned} \tag{1.4}$$

Typical cantilever thin film type sensors show a first flexural resonance of about 1 kHz, as utilised in section 2, associated with a rather low Q on the order of 100, limited by air damping. This example would result in a calculated direct ME bandwidth of 10 Hz centered at 1 kHz, which is too narrow for anticipated biomagnetic signals. So it would either require a resonator comb using various cantilever lengths in order to obtain larger bandwidth [Gri+02], designing towards lower frequency resonances results in overly large and vibration susceptible structures [Kul+14] .

If however active operation or a modulation scheme is already pursued, there is merit in using high frequency mechanical resonances in ME composites, as this has several advantages. Figure 1.12 on the next page shows the relations from equation (1.4) graphically. Note that B_{mod} effectively leads to half of the bandwidth being available, because the information carried by upper and lower sideband is the same, hence the available bandwidth is half. Utilising higher frequency resonances leads to increased bandwidth even at high quality factors, using a mode at about 500 kHz and a maximum quality factor of 1000 would lead to at least 250 Hz. This would already be suitable for the majority of biomagnetic tasks, see figure 1.1.

Magnetic Noise

Active operation in terms of supplying a modulation quantity to a magnetoelectric composite leads to successful escape of various low frequency noise contributions. However, a rather large magnetic modulation field is required in order to reach optimum SNR. This field modulation amplitude is on the order of several Oe, for sputtered amorphous soft magnetic materials [Urs+20] [Röb+15] [Chu+19] as well as amorphous ribbons [Fet+14]. Such a modulation field leads to strong periodic magnetisation changes [Jah13], these in turn lead to vast micromagnetic domain wall activity [Dea+96]. Periodic domain wall migration leads to strong interactions of domain walls with any kind of defects leading to effects which induce step wise magnetisation changes, such as;

- ▷ wall pinning at defects
- ▷ wall nucleation/annihilation [Urs+20]
- ▷ wall polarity change

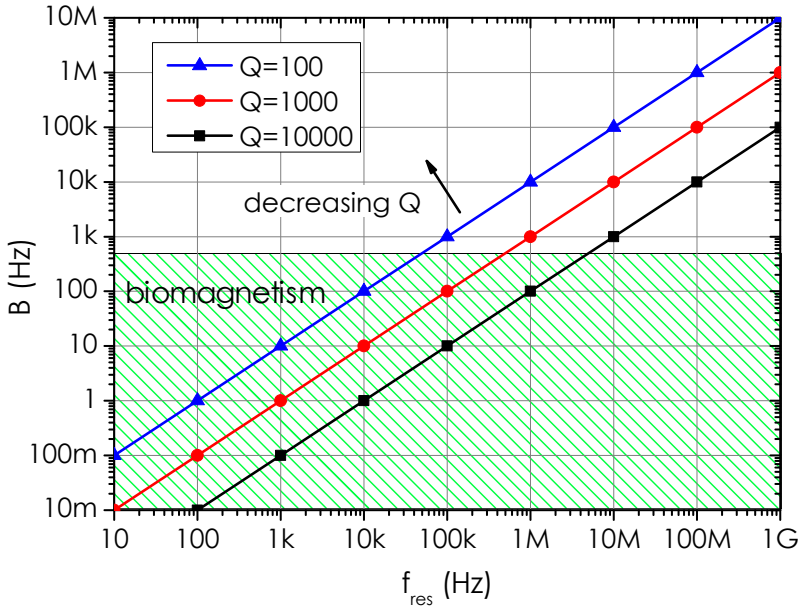

Figure 1.12: Maximum sensing bandwidth B for mechanical resonators as a function of their resonance frequency f_{res} and quality factors Q. The hatched area refers to biomagnetically relevant frequencies, the area under a curve is then available.

A microscopically step wise magnetisation change provoked by any of the aforementioned processes leads to induced voltage spikes when imagining a pickup coil arround a ferromagnet for readout. Likewise, but less intuitive, a step wise magnetostrictive response leads to mechanical fluctuations caused by quantified magnetostriction, in the case of magnetic field modulation via a surrounding coil. Any step wise occurring magnetisation process is responsible for magnetic noise generation, typically these discontinuities are found near the highest permeability [BS70], i.e. the working point of ME sensor composites. A perfectly periodic induced voltage spike caused by a domain wall snapping free from a pinning center would already lead to white noise. In any experiment other energy contributions such as local thermal fluctuations lead to randomisation of domain wall pinning and de-pinning events within subsequent magnetisation loops [BS70]. The reduction of domain wall density by introducing non ferromagnetic Cr spacer layers between magnetostrictive FeCoSiB layers proved successful in reducing Barkhausen noise [Jah13]. The ideal magnetic noise suppression is reached when practically no magnetic domains are present, either through the use of single domain structures [Dea+96] or by introducing an internal exchange bias field [Röb+15] and thus render domain formation energetically unfavorable [Urs+20]. Using such exchange biased multilayer films leads to strongly reduced noise generation through coherent rotation of the magnetisation rather than nucleation and migration of domain walls [Röb+15]. Magneto-optic images comparing a single layer with a magnetostrictive multilayer system can be found in section 5.1 on page 96.

Chapter 2

Publication: Electrically Modulated Magnetoelectric Sensors

After exploiting "active operation" principles of magnetoelectric resonators using alternating quantity modulation (or pumping) sources, the idea of substituting the rather large magnetic pumping field acting as a carrier for modulation with an electric field in order to manipulate the magnetism seemed worth a trial. Especially, as this brings several potential benefits at once;

(a) strongly reduced power consumption

(b) no large emitted stray magnetic fields, as required for sensor arrays

(c) electromagnetic coils are difficult to integrate.

Electric field control of magnetism is a trending topic as of post 2010s [Vaz12] as it seems highly attractive to be able to switch magnetic (polarisation) information using a voltage[1] pulse, as there are few alternate ways of creating a spatially confined magnetic field efficiently, without the use of electromagnetic coils. Essentially, one route for frequency independent manipulation of magnetic properties using an electric field is using a thick, strongly ferroelectric substrate (PMN, PZT) or electrostrictive lead magnesium niobate-lead titanate (PMN-PT) materials, able to supply the strains on the order of 100 ppms neccessary to control or even switch magnetisation of thin films using electric fields [Bur+11] [Hoc+13] [Kim+10]. The other route, exclusively used within this thesis is by thin film piezoelectrics in combination with strong mechanical resonance amplification supplying the required strain for the dynamic manipulation of the magnetic phase even at comparably low electric field strengths.

Attempts of measuring the influence of a static electric field on the magnetostrictive behavior of the presented thin film composites, unfortunately remained unsuccessful

[1] current essentially only flows when charging or discharging the piezoelectric capacitor

to date of writing. Static tuning of the slope and width of the magnetostriction curve by applying a DC voltage to the piezoelectric phase would be of great benefit in order to compensate for internal film stresses and thus taylor the piezomagnetic coefficient.

In order to clarify whether the principle of mixing an external magnetic signal onto an electrically applied carrier signal stems from; (a) the nonlinearity of the ferroelectric actuation or (b) is inherent to the strong stresses periodically straining the magnetostrictive phase during flexing specific experiments were carried out. (a) a monopolar excitation of the ferroelectric phase as well as (b) dynamical/static MOKE imaging was performed.

Figure 2.1 shows the upper sideband amplitude at increasing carrier amplitudes, for different DC offsets added to the unpoled PZT actuation film. At a DC offset corresponding to about the peak amplitude, the mixing product also reaches a maximum, when no DC offset is applied to the exciting waveform, the mixing output stays very low. The polarity of the offset does not affect the output strongly, thus this study indicates that a strong, linear excitation is neccessary for this kind of electrical modulation. Figure 2.2a shows a FEM simulation indicating high stresses generated near the

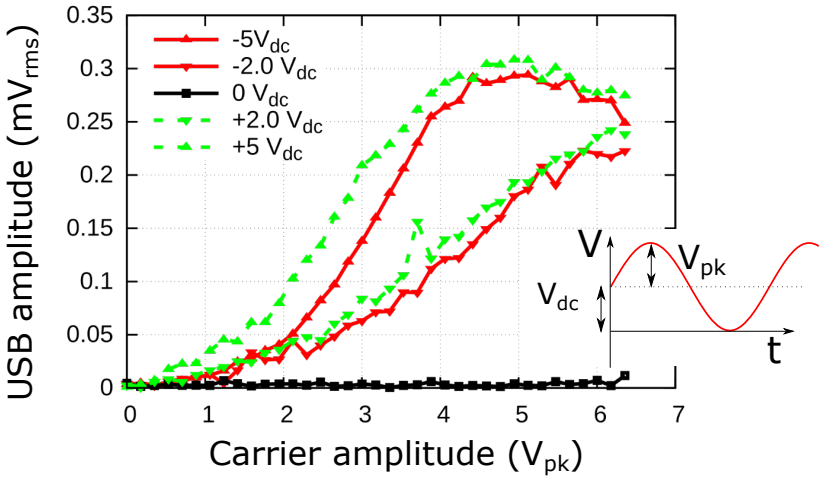

Figure 2.1: Sideband amplitude with respect to carrier amplitude and its DC offset, employing unpoled PZT. At an amplitude of 5 V_{pk}, equal to its offset at 5 V_{dc} a maximum occurs. This indicates that the mixing efficiency is enhanced by linerising the piezoelectric response by staying on one branch of the ferroelectric butterfly. This behavior holds true irrespective of the offset polarity. Very low sideband amplitudes are reached using no DC offset.

clamping of the cantilever structure in the first bending mode. Red color indicates high von Mieses stresses, whereas blue indicates very low stress. The cantilever is stressed very inhomogeneously, exhibiting a high stress intensity directly at its clamping, indicated by the dashed line, smearing out a bit due to the finite thickness of the substrate.

MOKE investigations indicate a good alignment of magnetic domains forming a stripe pattern along the short cantilever axis (x-axis) after a magnetisation decay perpendicular, figure 2.2b. The uniformity of the stripe pattern is an indication of a mostly relaxed film, although closure domains, which are formed towards the film edge are not visible here. A slight bulging of the domains in figure 2.2b evinces a static stress imposed on the film as it was glued to its carrier PCB after the magnetic annealing was performed. Using a 2 µm thick piezoelectric AlN film excited at 2 V, close to its first flexural mechanical resonance, shows a domain coarsening near the clamping of the cantilever, solely by the piezoelectrically generated stress, as no external magnetic field is applied. This MOKE imaging study was performed statically, meaning that the shutter is not tuned to the excitation phase. Furthermore time averaging, spanning several hundred excitation periods is performed, this leads to blurring of contrast in regions of non-reversible magnetisation processes. The blurring towards the free end of the cantilever as well as pronounced edge contrast is caused by strong deflection, thus defocussing of the image plane in the frontal section. Further increasing the excitation to 3 V the observed blurring is intensified as seen in figure 2.2c, however even at such high excitations the domain pattern is still visible, even in the presented, severely averaged images. The strong deflection of the free end furthermore leads to the invalidation of the background image taken after magnetic decay, which is substracted from the images in order to suppress non-magnetic dust particles and noise.

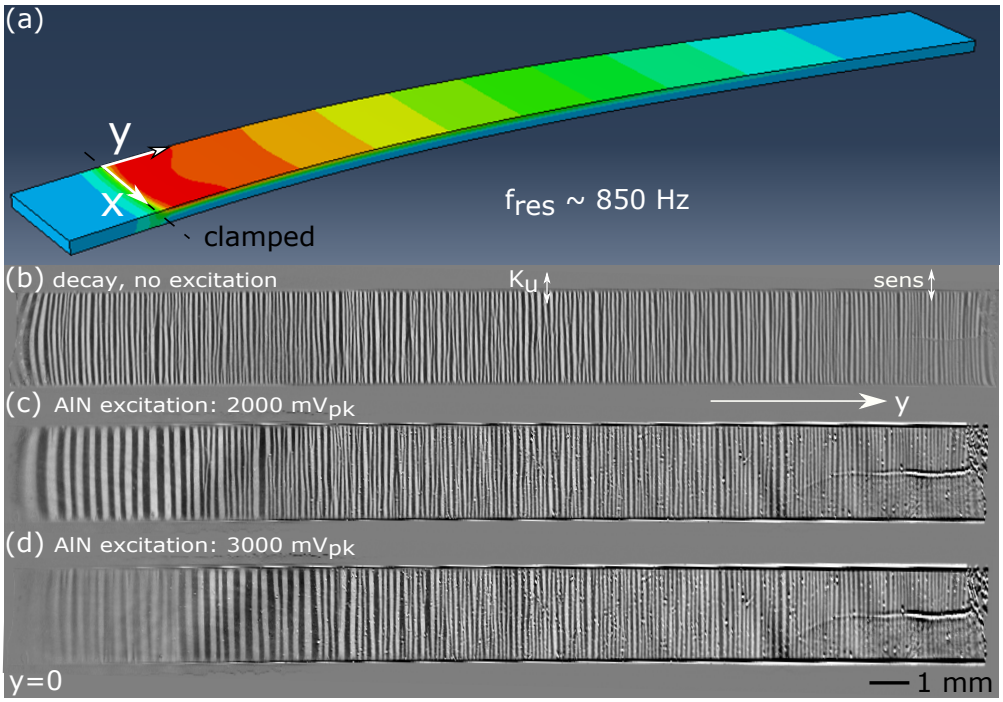

Figure 2.2: A cantilever excited in its first flexural resonance mode. a) FEM simulation showing color coded stress distribution, indicating that stress is severely concentrated near the fixed end. b) MOKE images after demagnetisation, revealing the magnetic domain configuration in a complete overview, spanning the entire magnetostrictive side of the ME cantilever. The domain pattern follows the induced anisotropy K_U, which points along the x direction. c) Upon application of a rather strong electric excitation of 2000 mV matching its first flexural resonance frequency at about 850 Hz, a slight modulation and blurring of the magnetic domains near the clamping is observed. indicating inverse magnetostrictive effects of the piezoelectrically generated stress. No magnetic bias field is present. d) Further increasing the excitation voltage amplitude to 3000 mV leads to even increased blurring near the fixed end. The crack-like disorder on the right side is a dust particle on the surface.

2.1 Publication: Electrically modulated magnetoelectric sensors

Own contributions to the following article[2]

- ▷ sample fabrication (large fraction)
- ▷ magnetic annealing (large fraction)
- ▷ wirebonding (large fraction)
- ▷ beam deflection measurements (large fraction)
- ▷ interpretation of the results (large fraction)
- ▷ writing of the manuscript (large fraction)

[2]this page is required by regulations

APPLIED PHYSICS LETTERS **108**, 182902 (2016)

Electrically modulated magnetoelectric sensors

P. Hayes,[1] S. Salzer,[2] J. Reermann,[2] E. Yarar,[1] V. Röbisch,[1] A. Piorra,[1] D. Meyners,[1] M. Höft,[2] R. Knöchel,[2] G. Schmidt,[2] and E. Quandt[1]
[1]*Institute for Materials Science, Christian-Albrechts-Universität zu Kiel, Kiel 24143, Germany*
[2]*Institute of Electrical and Information Engineering, Christian-Albrechts-Universität zu Kiel, Kiel 24143, Germany*

(Received 17 February 2016; accepted 20 April 2016; published online 2 May 2016)

Magnetoelectric thin film composites have demonstrated their potential to detect sub-pT magnetic fields if mechanical resonances (typically few hundred Hz to a few kHz) are utilized. At low frequencies (1–100 Hz), magnetic field-induced frequency conversion has enabled wideband measurements with resonance-enhanced sensitivities by using the nonlinear characteristics of the magnetostriction curve. Nevertheless, the modulation with a magnetic field with a frequency close to the mechanical resonance results in a number of drawbacks, which are, e.g., size and energy consumption of the sensor as well as potential crosstalk in sensor arrays. In this work, we demonstrate the feasibility of an electric frequency conversion of a magnetoelectric sensor which would overcome the drawbacks of magnetic frequency conversion. This magnetoelectric sensor consists of three functional layers: an exchange biased magnetostrictive multilayer showing a high piezomagnetic coefficient without applying a magnetic bias field, a non-linear piezoelectric actuation layer and a linear piezoelectric sensing layer. In this approach, the low frequency magnetic signal is shifted into the mechanical resonance of the sensor, while the electric modulation frequency is chosen to be either the difference or the sum of the resonance and the signal frequency. Using this electric frequency conversion, a limit of detection in the low nT/Hz$^{1/2}$ range was shown for signals of low frequency. *Published by AIP Publishing.* [http://dx.doi.org/10.1063/1.4948470]

Magnetoelectric (ME) composites, i.e., composites consisting of a piezoelectric and a magnetostrictive phase, gained large interest during the last decades as they offer, e.g., the possibility of sensing small magnetic fields.[1,2] In comparison to single phase magnetoelectric materials, composites show much higher magnetoelectric coefficients, which can be described as a product property, and much higher temperature ranges of use, which are limited by the ferroic transformations.[3] Furthermore, in case of thin film composites, one can benefit from small sensor sizes and a MEMS compatible low-cost fabrication route.[1]

In magnetoelectric composites, the magnetic field is transferred via a mechanical strain, i.e., the magnetostriction, in a change of the electric polarization state by the piezoelectric effect of the piezoelectric phase, which is described in whole by the magnetoelectric coefficient. Due to this mechanical transduction, the magnetoelectric coefficient is frequency dependent, showing large resonance enhancement of the magnetoelectric composite. Compared to other composites, thin film composites exhibit a large enhancement at the mechanical resonance, which is determined by the high quality factor of the Si-based cantilevers.[4,5] This can be further enhanced by reducing the resonance frequency,[6] or by eliminating air damping by operation in vacuum.[7] In the mechanical resonance, which is typically between 100 Hz and 10 kHz for single-side clamped cantilevers, limit of detections (LOD) of approximately 1 pT/Hz$^{1/2}$ can be reached.[8] This LOD can be further enhanced using two cantilevers in a tuning fork arrangement, which is less sensitive to acoustic noise and vibrations. In this case, 500 fT/Hz$^{1/2}$ were achieved at a mechanical resonance of 958 Hz.[9]

One disadvantage of magnetoelectric composites is the necessity to use a magnetic DC bias field in order to operate at the maximum of the piezomagnetic coefficient. This can be omitted, e.g., by the use of an exchange biased (EB) magnetic phase.[10] Other possibilities are based on the integration of hard magnetic layers with a permanent moment,[11] the use of remanence magnetization,[12] or field-dependent resonant frequency[13] in a hysteretic magnetostrictive material, or the use of stresses by means of the inverse magnetostriction. Further details can be found in Ref. 14.

Magnetic field sensors which are capable of detecting sub-pT magnetic fields are in general attractive for biomagnetic applications, such as magnetocardiography (MCG) and magnetoencephalography (MEG). Figure 1 schematically shows the typical field-frequency ranges of MCG and MEG, respectively, as well as the frequency-dependent LOD of a cantilever-type magnetoelectric sensor.[15] These data were derived from noise analysis and the measurement of the magnetoelectric coefficient using

$$H_{min}(f) = LOD(f) = \frac{U_{noise}(f)}{\alpha(f)}, \tag{1}$$

where H_{min} denotes the minimum detectable field, which is equal to the limit of detection (LOD), U_{noise} the voltage noise density that includes all noise contributions and α the magnetoelectric voltage coefficient. Although the resonance frequency can be adjusted by the geometry of the cantilever, the results indicate that the required broadband, low-frequency, and low field measurements required for MCG and MEG applications cannot be met using the present magnetoelectric thin film sensors. For out-of-resonance measurements, the

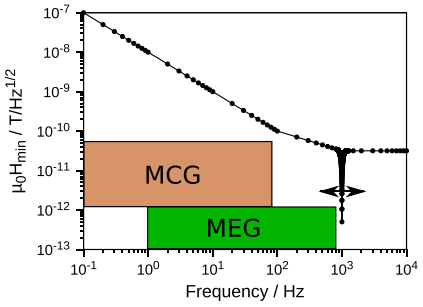

FIG. 1. Typically achievable limit of detection (LOD) of cantilever type thin film ME composites. The dip indicates the strongly enhanced detection limit in mechanical resonance. 1/f noise is strongly dominant towards frequencies below 100 Hz. The resonance bandwidth is determined by the mechanical quality factor. The horizontal arrows indicate the possibility to set the mechanical resonance by adjusting the geometry of the cantilever. The field-frequency regions of magnetocardiography (MCG) and magnetoencephalography (MEG) are indicated for comparison.

LOD is not sufficient, as the effect enhancement by the mechanical resonance is missing and the required sensor electronics exhibit a 1/f noise increase in the low-frequency range. Furthermore, tuning the resonance to lower frequencies would result in an extremely narrow resonance bandwidth (<0.1 Hz), equivalent to an extremely slow oscillation build-up, as well as in fragile sensor structures and in enhanced cross-sensitivity to acoustic noise and vibrations.

In recent years, two indirect detection schemes have emerged to remedy the challenges posed by direct magnetoelectric measurements at low frequencies: magnetoelectric sensors based on the delta-E effect[16,17] or those using frequency conversion.[18,19]

By exploiting the change in Young's modulus of a ferromagnetic material upon magnetization, i.e., the delta-E effect, low frequency magnetic fields lead to a change of the resonance frequency of the cantilever, while the mechanical resonance is excited using the piezoelectric layer. This approach offers a promising route to measure low-frequency magnetic fields, largely avoiding acoustic and 1/f noise contributions. With resonators exhibiting resonant frequencies of several kHz to hundreds of MHz showing high quality factors, it is possible to achieve, e.g., a LOD in the hundred pT/Hz$^{1/2}$ range at 20 Hz,[17,20] which is an enhancement of approximately two orders of magnitude compared to direct magnetoelectric measurements.

The magnetically induced frequency conversion technique (MFC) allows transferring a signal of arbitrary frequency outside resonance to the mechanical resonance frequency of the sensor.[18,19] To this end, the nonlinear characteristics of the magnetostriction curve is utilized: in a certain range of around zero magnetic field, the magnetostriction changes almost quadratically. If now instead of the commonly used constant bias field an alternating bias B_{mod} is applied, the slope of the magnetostriction curve of the sensor, which is seen by the small AC magnetic field B_{AC} to be measured, is caused to vary with time at the instantaneous operating point corresponding to the modulation frequency. The slope describes a small signal transfer characteristic of the superposition of B_{mod} and B_{AC} into a magnetostrictive elongation. Assuming sinusoidal signals, the square of the sum of both signals contains a product term, which expresses a frequency conversion given by,

$$\begin{aligned} &2 \cdot \hat{B}_{\mathrm{mod}} \hat{B}_{AC} \cdot \cos(2\pi f_{\mathrm{mod}} t) \cdot \cos(2\pi \cdot f_{AC} \cdot t) \\ &= \hat{B}_{\mathrm{mod}} \cdot \hat{B}_{AC} \cdot (\cos(2\pi (f_{\mathrm{mod}} + f_{AC}) \cdot t) \\ &\quad + \cos(2\pi (f_{\mathrm{mod}} - f_{AC}) \cdot t)), \end{aligned} \tag{2}$$

where hats denote peak values and f_{mod} and f_{AC} is the frequency of the alternating bias and of the small AC signal, respectively. If f_{mod} is chosen to make either $f_{mod}+f_{AC}$ (upper sideband) or $f_{mod}-f_{AC}$ (lower sideband) exactly meet the mechanical resonance of the sensor, the great advantage is offered that resonant operation of the sensor at a virtually arbitrary input frequency is possible. Further details are described in Ref. 18. For low input frequencies, it was thus shown that the sensitivity can be enhanced by up to three orders of magnitude compared to the unmodulated case, reaching a LOD of up to 100 pT/Hz$^{1/2}$ in the low frequency range.[20,21] In theory, if all the additional noise could be fully suppressed, the LOD for an up-converted signal would be expected to be comparable to the LOD in the mechanical resonance. But currently, additional magnetic noise impairs the attainment of the same sensitivity as in resonance.[8]

Despite the encouraging results, the modulation with a magnetic field with a frequency close to the mechanical resonance results in a number of drawbacks (e.g., size, energy consumption, crosstalk by the modulation fields in sensor arrays, additional magnetic noise through considerable magnetic domain activity caused by large modulation amplitudes[8,22]), which could be overcome by a corresponding electric modulation of the magnetoelectric sensors.

Therefore, the focus of this paper is a feasibility study of electrically induced frequency conversion of a low frequency magnetic signal into the resonance frequency of a magnetoelectric cantilever-type sensor, employing two electrically independent electrodes. In this case, the sum (or the difference) of the electric modulation frequency f_{mod} and the frequency of the magnetic signal f_{AC} matches the resonance frequency of the cantilever thus being a completely different approach to the electrical resonant modulation as it is used in delta-E effect sensors or in noise suppression studies.[23,24]

For this work, magnetoelectric sensors with two electrically independent piezoelectric phases with different properties are utilized (Figure 2) in order to substitute the driving magnetic field used in MFC by an electric field. The electric modulation field is applied to an unpoled lead zirconate titanate (PZT) layer, and a comparison of the two piezoelectric displacement characteristics is given in Figure 2(b). AlN behaves strictly linear, whereas the PZT shows a hysteretic, rather quadratic displacement with respect to applied DC voltage. PZT is used since it shows a non-linear piezoelectric coefficient, which is considered to be essential for the frequency conversion. AlN is used for the detection of the magnetoelectric voltage, which has a much higher piezoelectric voltage coefficient, along with a lower loss tangent, promising an overall better choice for detection purposes.[25] In other

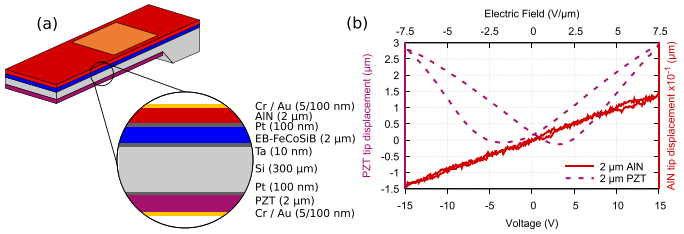

FIG. 2. (a) Schematic of the ME composite samples incorporating three active layers, EB-FeCoSiB as magnetostrictive phase, AlN as linear piezioelectric phase for readout, and non-linear unpoled PZT for excitation. (b) Displacement-voltage characteristic for both piezoelectric phases of a ME cantilever under DC electric field.

studies on electrically modulated magnetoelectric sensors, the readout is performed by using a pickup coil wound around the sensor.[21,26,27]

Cantilevers of 25 mm length and 2.3 mm width were fabricated using 300 μm double side polished silicon substrates. A schematic sketch of the cantilever is given in Figure 2(a). A seed layer of 100 nm sputtered platinum is followed by 2 μm PZT deposited by chemical solution deposition, and further details on the process are given by Piorra *et al.*[28] Electrodes of Cr/Au are sputter deposited on top and structured using standard lithography and wet etching. This electrode spans across the length of the cantilever with approx. 300 μm of spacing towards the edges. On the flip-side, 10 repetitions of a 200 nm exchange biased stack of FeCoSiB were sputter deposited, and the detailed layer sequence is given by Röbisch *et al.*[8] This magnetostrictive phase was patterned using standard photolithography followed by lift-off, spanning the full free-standing length of the cantilever. On top of this, a 2 μm layer of piezoelectric AlN was reactively deposited using pulse DC sputtering of Al in a pure nitrogen atmosphere without substrate heating. Wet etching of the AlN was performed using H_3PO_4 at 80 °C for 40 min in order to electrically access the FeCoSiB layer, which also acts as AlN bottom electrode. Cr/Au was again used as a top electrode for the AlN, with reduced dimensions of 7.5 mm × 1.2 mm, starting from the line of mechanical clamping. The samples were magnetically field annealed (1 kOe, 250 °C under ambient conditions for 30 min) in order to set the in-plane direction of the exchange bias and the induced anisotropy at 45° with respect of the long axis of the cantilever similar to Ref. 10. Both Au top electrodes of the cantilever sides were contacted using 20 μm AlSi wires by wirebonding, and the bottom electrodes were electrically shorted and contacted using silver paste. The capacitances of the two formed plate capacitors are 420 pF and 250 nF for the AlN and PZT capacitors, respectively.

Measurements were done using a setup which is located in a magnetically and electrically shielded chamber as described in Ref. 15. The magnetic low frequency signal was supplied by a Keithley 6221 current source driving a home-made coil, providing field in axial direction of the sensor. Measurements were conducted using an RME Fireface UFX sound card and an SR785 Spectrum Analyser both as source for the electrical modulation signal applied directly to the PZT and sink for the output signal from the AlN. The output signal was amplified using a low noise battery operated charge amplifier circuit employing the AD745 by Analog Devices.

In a first experiment, given in Figure 3, the sensor was excited via the PZT layer with a 0.3 V_{pp} sinusoidal signal at the mechanical resonance (f_{res}) of 689 Hz, while a low frequency sinusoidal 2 Hz magnetic field with an amplitude of 1 μT was applied in parallel. No constant magnetic bias field was applied as the exchange biased magnetostrictive multilayer shows its maximum magnetoelectric response in zero field. The output spectrum as detected at the AlN layer (Figure 3) shows a maximum peak at the resonance frequency that stems from the carrier signal which is electrically isolated but elastically coupled to the AlN layer. Furthermore, two side bands at $f_{mod} \pm 2$ Hz can be seen, which exhibit an equal amplitude and demonstrate the up-conversion similar as it is also shown by Zhuang *et al.*[29] The resonance curve is superimposed by the dashed line indicating the resonance amplification, being maximum at the mechanical resonance frequency. A limit of detection of approximately 5 nT/Hz$^{1/2}$ can be derived upon the fact that a 1 μT signal is approx. 45 dB above the noise floor. The drawback of this approach is related to the high quality factor of the resonator so that resonance amplification is restricted to a very limited frequency range of maximum a few Hz.

For higher frequencies of the magnetic field, in this case at $f_{AC} = 20$ Hz with an amplitude of 1 μT, the electric frequency conversion was examined. Figure 4(a) shows an

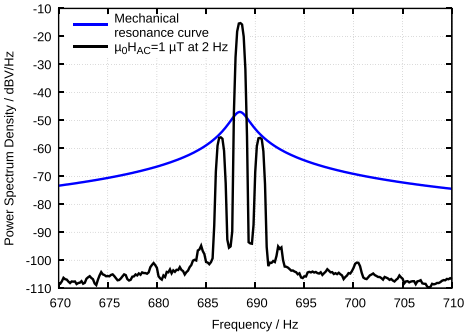

FIG. 3. Sensor output spectrum taken from the AlN layer. The sensors PZT layer is excited in mechanical resonance at $f_{mod} = 689$ Hz by a sine signal of an amplitude of 0.3 V_{pp}, and the dashed line qualitatively indicates the resonance behavior of the cantilever. A low frequency 2 Hz sinusoidal magnetic field of an amplitude of 1 μT is present, as a result two equally large sidebands are formed around the resonance at $f_{mod} \pm 2$ Hz. From a simple estimation, the LOD can be deduced as 5 nT/Hz$^{1/2}$.

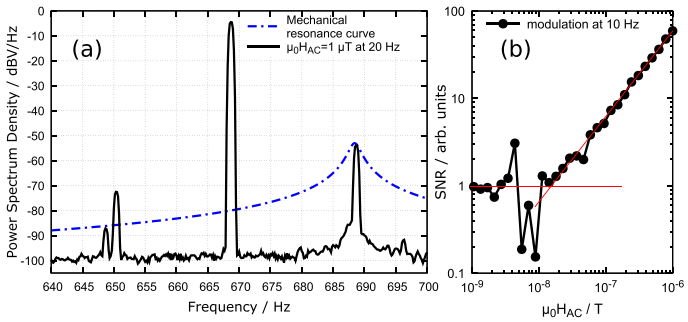

FIG. 4. (a) Sensor output spectrum taken from the AlN layer. The applied carrier signal frequency is given by f_{mod} at 669 Hz, the amplitude of the sinusoidal carrier signal corresponds to 2 V_{pp}, and this is applied 20 Hz below the mechanical resonance. A 20 Hz sinusoidal magnetic field of 1 μT magnitude is applied to the sensor, and this is seen in the two sidebands $f_{mod} \pm 20$ Hz forming upon magnetic signal application. Note that the lower sideband is 40 Hz away from the mechanical resonance. At 650 Hz, an odd mains multiple is seen. (b) Shows a linearity measurement performed at magnetic field of 10 Hz, where the noise floor is reached at about 10 nT/$Hz^{1/2}$.

output spectrum of the same sensor, again recorded across the AlN layer. The carrier can be interpreted as a residual carrier, which appears as perfect carrier suppression is not given due to the fact that the piezoelectric PZT is not perfectly quadratic with respect to the driving voltage, instead it shows some hysteresis, as can be seen in Figure 2(b). In this case, the sinusoidal carrier signal of 2 V_{pp} is applied to the PZT layer, corresponding to a maximum electric field strength of 0.5 MV/m. The modulation frequency was set to $f_{mod} = f_{res} - f_{AC} = 669$ Hz. As a result, an upper and a lower side band appears around the carrier signal f_{res} separated by f_{AC}, $f_{mod} + f_{AC}$, and $f_{mod} - f_{AC}$, respectively. One can see that the upper sideband peak, corresponding to the resonance at 689 Hz, greatly benefits from the bending resonance gaining approximately 30 dB in amplitude over the lower sideband ($f_{mod} - f_{sig}$), which is 40 Hz below the resonance. Thus, this result demonstrates the general feasibility of an electrical frequency conversion. In this mode, the 1 μT signal shows a signal-to-noise ratio of 40 dB, which corresponds to an LOD of about 10 nT/$Hz^{1/2}$. It is also apparent that there is a slight increase in the noise floor in close vicinity to the resonance, which might be attributed to thermal noise similar as described by Zhuang *et al.*[24] Figure 4(b) shows the linear dependence with respect to the magnetic field amplitude for a magnetic field of 10 Hz.

This study has demonstrated the general feasibility of electrical frequency conversion, enabling the detection of low amplitude magnetic fields at low frequencies. The excitation as well as the readout is conducted by means of individual piezoelectric phases, rather than employing pickup coils around the composite. Using two individual piezoelectric layers brings the additional benefit of inherent electrical isolation between actuation voltage and readout signal, opening the possibility for compensation-free operation. The presented electrical frequency conversion remedies the main drawbacks associated with magnetic frequency conversion. The power consumption is much lower; additionally, the electrical frequency conversion produces no interfering external stray fields. Furthermore, electrical frequency conversion allows to operate the sensor at much higher resonance frequencies, which is not possible for magnetic excitation due to the high magnetic field amplitudes that are required. Higher resonance frequencies are of advantage for achieving wide bandwidths and for reducing cross-sensitivities to acoustic noise and vibrations. Additionally, sweeping the carrier signal, a magnetic spectrum analyzer can be realized, which effectively scans a range of frequencies into the mechanical resonance.[30] By this the detection of wideband waveforms is enabled. In this case, it is beneficial to design the sensor in a way which provides higher resonance frequencies. When the resonance frequency is sufficiently high, the onset time when scanning the carrier signal gets negligible against the period of the highest frequency in the signal to be measured.

Two different paths are possible for this conversion approach to work. First due to large amplitude excitation of the PZT thin film layer the mechanical motion of the cantilever is governed by the non-linear displacement curve (see Figure 2(b)), the instantaneous slope determines the piezoelectric conversion coefficients which are seen by the magnetostrictive response to small magnetic fields. The output voltage in the AlN then shows a voltage which is the commutation of the large amplitude carrier signal and the small magnetic signal, similar to the case of magnetic frequency conversion. The second path relies on inverse magnetostriction which is present whenever the sensor is mechanically deformed by the actuating PZT layer. Upon deformation the magnetostrictive layer periodically alters its piezomagnetic coefficient, which, when at its maximum offers high sensitivity towards small magnetic fields.

Future work will be conducted in order to clearly discern which route is primarily responsible for the mixing, taking place either in the magnetostrictive layer or in the piezoelectric sensing layer. Furthermore, the noise sources for the electrical frequency conversion have to be investigated in comparison to the magnetic frequency conversion.

The authors would like to thank the German Research Foundation (Deutsche Forschungsgemeinschaft, DFG) who funded this work under the Grant No. PAK 902 “Magnetoelectric Sensors for Medicine.”

[1]S. Marauska, R. Jahns, H. Greve, E. Quandt, R. Knöchel, and B. Wagner, J. Micromech. Microeng. **22**, 65024 (2012).
[2]R. Jahns, H. Greve, E. Woltermann, E. Quandt, and R. H. Knöchel, IEEE Trans. Instrum. Meas. **60**, 2995 (2011).
[3]C.-W. Nan, M. I. Bichurin, S. Dong, D. Viehland, and G. Srinivasan, J. Appl. Phys. **103**, 31101 (2008).
[4]J. Zhai, Z. Xing, S. Dong, J. Li, and D. Viehland, J. Am. Ceram. Soc. **91**, 351 (2008).
[5]H. Greve, E. Woltermann, H.-J. Quenzer, B. Wagner, and E. Quandt, Appl. Phys. Lett. **96**, 182501 (2010).
[6]A. Kulkarni, K. Meurisch, I. Teliban, R. Jahns, T. Strunskus, A. Piorra, R. Knöchel, and F. Faupel, Appl. Phys. Lett. **104**, 22904 (2014).
[7]C. Kirchhof, M. Krantz, I. Teliban, R. Jahns, S. Marauska, B. Wagner, R. Knöchel, M. Gerken, D. Meyners, and E. Quandt, Appl. Phys. Lett. **102**, 232905 (2013).
[8]V. Röbisch, E. Yarar, N. O. Urs, I. Teliban, R. Knöchel, J. McCord, E. Quandt, and D. Meyners, J. Appl. Phys. **117**, 17B513 (2015).
[9]S. Salzer, R. Jahns, A. Piorra, I. Teliban, J. Reermann, M. Höft, E. Quandt, and R. Knöchel, Sens. Actuators A **237**, 91 (2016).
[10]E. Lage, C. Kirchhof, V. Hrkac, L. Kienle, R. Jahns, R. Knöchel, E. Quandt, and D. Meyners, Nat. Mater. **11**, 523 (2012).
[11]K. Tadahiko and S. Isao, "Self bias magnetostrictive material," Japanese patent 09083037 A (1997).
[12]S. K. Mandal, G. Sreenivasulu, V. M. Petrov, and G. Srinivasan, Appl. Phys. Lett. **96**, 192502 (2010).
[13]T.-D. Onuta, Y. Wang, C. J. Long, and I. Takeuchi, Appl. Phys. Lett. **99**, 203506 (2011).
[14]Y. Zhou, D. Maurya, Y. Yan, G. Srinivasan, E. Quandt, and S. Priya, Energy Harvesting Syst. **3**, 1 (2016).
[15]R. Jahns, R. Knöchel, H. Greve, E. Woltermann, E. Lage, and E. Quandt, in *2011 IEEE International Workshop on Medical Measurements and Applications Proceedings (MeMeA)* (2011), pp. 107–110.
[16]B. Gojdka, R. Jahns, K. Meurisch, H. Greve, R. Adelung, E. Quandt, R. Knöchel, and F. Faupel, Appl. Phys. Lett. **99**, 223502 (2011).
[17]T. Nan, Y. Hui, M. Rinaldi, and N. X. Sun, Sci. Rep. **3**, 1985 (2013).
[18]R. Jahns, H. Greve, E. Woltermann, E. Quandt, and R. Knöchel, Sens. Actuators A **183**, 16 (2012).
[19]S. M. Gillette, A. L. Geiler, D. Gray, D. Viehland, C. Vittoria, and V. G. Harris, IEEE Magn. Lett. **2**, 2500104 (2011).
[20]S. Zabel, C. Kirchhof, E. Yarar, D. Meyners, E. Quandt, and F. Faupel, Appl. Phys. Lett. **107**, 152402 (2015).
[21]X. Zhuang, M. Lam Chok Sing, C. Dolabdjian, Y. Wang, P. Finkel, J. Li, and D. Viehland, KEM **644**, 236 (2015).
[22]N. O. Urs, I. Teliban, A. Piorra, R. Knöchel, E. Quandt, and J. McCord, Appl. Phys. Lett. **105**, 202406 (2014).
[23]X. Zhuang, M. L. C. Sing, C. Dolabdjian, Y. Wang, P. Finkel, J. Li, and D. Viehland, IEEE Trans. Magn. **51**, 1 (2015).
[24]X. Zhuang, M. L. C. Sing, and C. Dolabdjian, IEEE Trans. Magn. **49**, 120 (2013).
[25]S. Trolier-McKinstry and P. Muralt, J. Electroceram. **12**, 7 (2004).
[26]Y. K. Fetisov, V. M. Petrov, and G. Srinivasan, J. Mater. Res. **22**, 2074 (2007).
[27]J. L. Hockel, T. Wu, and G. P. Carman, J. Appl. Phys. **109**, 64106 (2011).
[28]A. Piorra, R. Jahns, I. Teliban, J. L. Gugat, M. Gerken, R. Knöchel, and E. Quandt, Appl. Phys. Lett. **103**, 32902 (2013).
[29]X. Zhuang, M. L. C. Sing, C. Cordier, S. Saez, C. Dolabdjian, L. Shen, J. F. Li, M. Li, and D. Viehland, IEEE Sens. J. **11**, 2266 (2011).
[30]Y. K. Fetisov, D. A. Burdin, D. V. Chashin, and N. A. Ekonomov, IEEE Sens. J. **14**, 2252 (2014).

2.1.1 Supplemental Material

Figure 2.3 shows the amplitude response for an electrically modulated sensor as shown in publication 1 Fig. 4a. The higher the f_{AC} frequency is, the further f_{mod} needs to move away from the resonance, resulting in less amplification for a given carrier amplitude of $4.5\,\mathrm{V_{pp}}$. Hence why the amplitude at f_{res} decays with increasing F_{AC}. In a practical scenario the carrier amplitude has to be equalized in order to account for the lowpass character of the mechanical resonance, see section 4 on page 83. Slices from figure 2.3 prove a linear response towards the external magnetic signal amplitude H_{AC} at various frequencies of f_{AC} are shown in figure 2.4 on the following page.

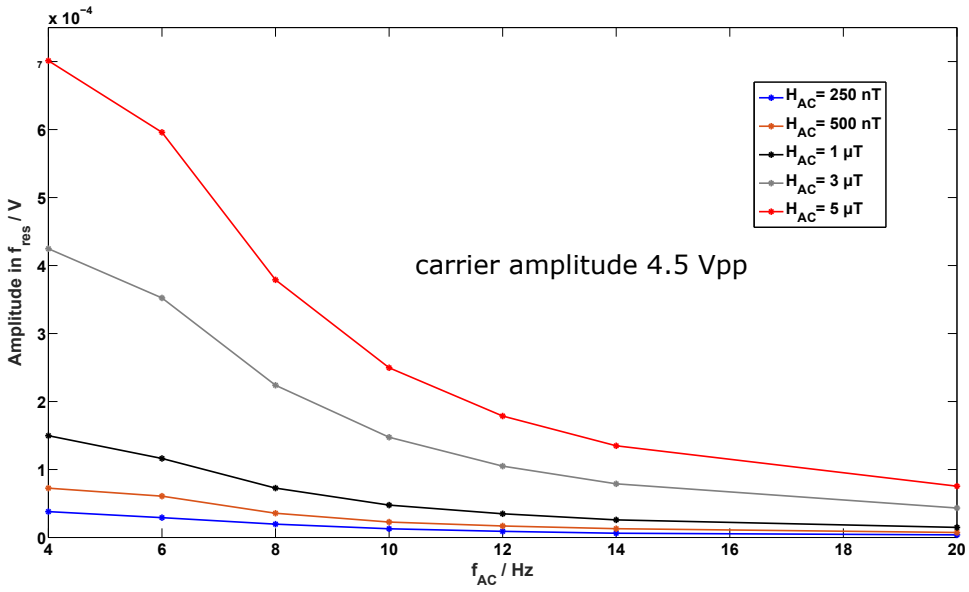

Figure 2.3: Sensor response for various frequencies and H_{AC} amplitudes. The carrier frequency (f_{mod}) was continually changed to satisfy the condition of $f_{res} = f_{mod} + f_{AC}$, maintaining a constant carrier amplitude. Note the different slopes which are due to the fact that the carrier as well as the signal get less resonance enhanced for increasing values of f_{AC}. This can be accounted for by adapting the amplitude of f_{mod}.

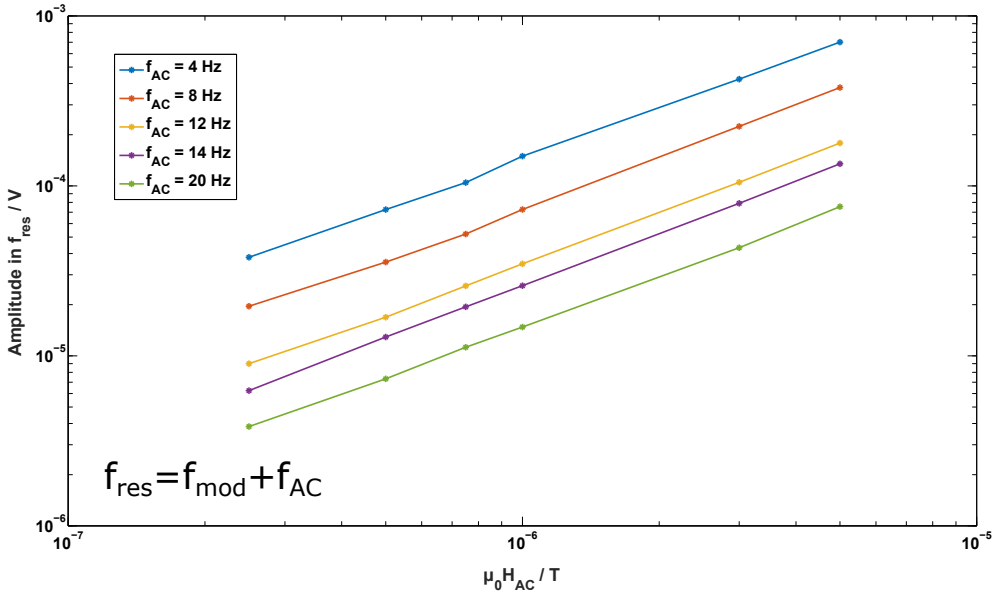

Figure 2.4: Linearity for various frequencies f_{AC} of the external magnetic field H_{AC}. Frequency behavior of the magnetic field amplitude under a fixed excitation amplitude of the PZT of 4.5 V_{pp}.

2.2 Conclusion

Successful implementation of electrical modulation using the first flexural mode of oscillation was shown. A great advantage of this method lies in its inherent integrability achieved by using an electrically excited piezoelectric material rather than an electromagnetic coil to modulate and readout the magnetoelectric composite. A bias or modulation coil surrounding the composite is omitted when an exchange biased magnetostrictive phase is employed, internally setting the working point. Absence of an actively excited coil in the vicinity of the composite furthermore enables the integration into sensor arrays, diminishing cross talk between nodes. This work was filed for a patent application and was granted under [HQK16].

Nevertheless, using the first flexural resonance mode leads to strong acoustic noise pickup, as the resonance frequencies typically lie within the audio frequency regime. A rather low converse magnetoelectric coupling demands high excitation voltages on the order of several volts in order to modulate the magnetisation, see figure 2.2 on page 28.

Chapter 3

Publication: Electrically modulated magnetoelectric AlN/FeCoSiB film composites for DC magnetic field sensing

The discovery of two high frequency mechanical modes exhibiting very large converse magnetoelectric coupling has led to further exploitation and thus departure from low order flexural modes. Using a pickup coil surrounding the composite has improved the LOD by about one order of magnitude. Traditionally such a readout scheme is associated with bulk ME composites [HWC11], [FPS07]. This scheme circumvents issues with spatially extended magnetic fields arising via electromagnetic coils when used as an excitation source, as this coil is only passively operated. Acoustic noise [Ree+15] does not couple strongly into such high frequency oscillations, leading to increased immunity towards ambient acoustic pickup. The resonance modes are especially insensitive to length variations of cantilever mounting, significantly lowering spread through fabricated composites, see section 3.3 on page 60.

Own contributions to the following article[1]

- ▷ design and construction of the measurement setup (large fraction)
- ▷ measurements (large fraction)
- ▷ design/construction of coil body (large fraction)
- ▷ coil winding (large fraction)
- ▷ interpretation of results (large fraction)
- ▷ writing of the manuscript (large fraction)

[1] this information is required by regulations

Journal of Physics D: Applied Physics

ACCEPTED MANUSCRIPT

Electrically modulated magnetoelectric AlN/FeCoSiB film composites for DC magnetic field sensing

To cite this article before publication: Patrick Hayes *et al* 2018 *J. Phys. D: Appl. Phys.* in press https://doi.org/10.1088/1361-6463/aad456

Electrically Modulated Magnetoelectric AlN/FeCoSiB Film Composites For DC Magnetic Field Sensing

P. Hayes[1], V. Schell[1], S. Salzer[2], D. Burdin[3], E. Yarar[1], A. Piorra[1], R. Knöchel[2], Y. Fetisov[3], and E. Quandt[1]

[1]*Institute for Materials Science, Christian-Albrechts-Universität zu Kiel, Kiel 24143, Germany*

[2]*Institute of Electrical and Information Engineering, Christian-Albrechts-Universität zu Kiel, Kiel 24143, Germany*

[3]*Moscow Technological University (MIREA), Moscow 119454, Russia*

Keywords: Magnetoelectric thin film composite, electric frequency conversion, pickup coil, AlN, amorphous FeCoSiB, inverse magnetostrictive, magnetic field sensor, mechanical vibration

Abstract

Measurements of the converse magnetoelectric effect, observed for mesoscopic cantilever type magnetoelectric composites are presented. The silicon based samples employ 2 µm of amorphous $(Fe_{90}Co_{10})_{78}Si_{12}B_{10}$ film as soft magnetic, magnetostrictive phase. The piezoelectric phase consists of 2 µm sputter deposited, highly textured aluminum nitride (AlN) in a plate capacitor arrangement.

Exciting the piezoelectric phase at various frequencies leads to sharp peaks of induced voltage in a surrounding, mechanically decoupled pickup coil, corresponding to several mechanical resonances of the beam. The peak amplitude modulation can be exploited to detect DC magnetic fields. This entirely passive readout strategy is advantageous over other methods of sensitivity enhancement, typically requiring an active source of magnetic fields, thus prohibiting the construction of sensor arrays.

Field dependent mechanical quality factors of up to 3800 near magnetic saturation are featured by a strong field dependence of induced voltage, reaching to 2290 V/T in the 20 µT field regime. Vibrational measurements reveal a combination of the 15th flexural with a high order torsional mode as primarily active, at a resonance frequency of 520.7 kHz. This finding is supported by simple analytical estimations and literature. In unbiased operation a linear resolution of 1.2 nT towards small 200 mHz fields is shown.

Introduction

The magnetoelectric effect in composites arises artificially as a product property, governed by the magnetic as well as the piezoelectric phase. Thin film magnetoelectric composites allow for great design flexibility in that a combination out of a great plethora of materials [1, 2] of both classes can be chosen independently, specific to the application. For the detection of very small magnetic fields, on the order of picotesla [3] , soft magnetic materials in combination linear piezoelectric thin films pose a great potential as next generation magnetic sensors, exploiting a mechanical resonance enhancement on the magnetoelectric effect. Magnetoelectric composite sensors, show excellent performance when utilized in a direct measurement using low order mechanical flexural resonances at several hundred hertz [4]. However, the detection of magnetic signals, especially those of low amplitude and very low frequency as ubiquitous in biomagnetic systems can reach down to as low as 100 mHz for human brain delta waves encountered during deep sleep phases [5], up to brain gamma waves which reach up to about 50 Hz [6].

In order to access these biomagnetic applications, demanding detection of very low frequencies and low field amplitudes in the fT to pT range, it is essential to conduct frequency conversion by actively driving the composite either using a magnetic field modulation [7] or an electric modulating field [8]. Using this strategy, the narrow bandwidth, typically seen in magnetoelectric composites can be remedied without the loss of the mechanical resonance enhancement.

One of the most severe challenges is the detection of quasi DC magnetic fields using magnetoelectric composites [9, 10] or AMR sensors [11]. Fundamentally, a magnetoelectric composite is limited by two factors governing the low frequency response, (a) the 1/f-noise exhibited by any charge amplifier

employed and (b) the time constant arising by the charge conservation in any leaky piezoelectric material, given by $t = R_{piezo} \cdot C_{piezo}$.

In this work a passive readout method using a pickup coil is applied to a mesoscopic thin film magnetoelectric composite under active piezoelectric excitation. The induced voltage is characterized in terms of the obtainable limit of detection (LOD) for very low frequency magnetic fields of 200 mHz.

Methods / Experimental

Thin film composites were fabricated using oxidized silicon substrates with a thickness of 350 µm. The processes are magnetron sputter deposition, standard photolithography and subsequent ion beam etching as described in [12]. Double side polished substrates were employed, enabling both active layers to have low-roughness surface as well as maximum the design flexibility. The employed AlN piezoelectric film is pulse DC sputtered, the details of the process can be found elsewhere [4]. The amorphous magnetostricitve phase consists of an amorphous iron-cobalt-silicon-boron alloy of a nominal composition of $(Fe_{90}Co_{10})_{78}Si_{12}B_{10}$, which was sputter deposited in 10 subsequent layers of 200 nm thickness. A cooling pause of 15 minutes is introduced between these depositions, in order to prevent any excessive heating and thus maintain the amorphous structure[13].

On the aluminum nitride (AlN) side (Figure 1, b) of the substrate all layers were deposited without any vacuum breakage, an AlN wet etching step is performed using H_3PO_4 at 80 °C for 20 minutes in order to allow electrical access to the platinum bottom electrode, followed by a subsequent room temperature wet etching of the chromium/gold top electrode. The top electrode width is reduced by 100 µm with respect to the AlN layer, in order to prevent short circuits between top and bottom electrode, indicated in Figure 1,b. The formed plate capacitor features a capacity of about 1.7 nF at 1 kHz. Finally, the samples are diced into cantilever beams with dimensions of 2.45 mm by 25 mm. Magnetic annealing in a homogenous magnetic field in excess of 800 Oe directed along the short axis for 30 minutes at 280 °C is performed in order to induce a magnetic easy axis and to reduce film

stresses without crystallising the film. At last the composites are fixed to FR4 boards using cyanoacrylate adhesive, resulting in an effective freestanding cantilever structure length of 23 mm. Wire bonding to copper pads on the FR4 PCB with a manual wire bonder (Devoltec) ensures electrical contact, see Figure 1a.

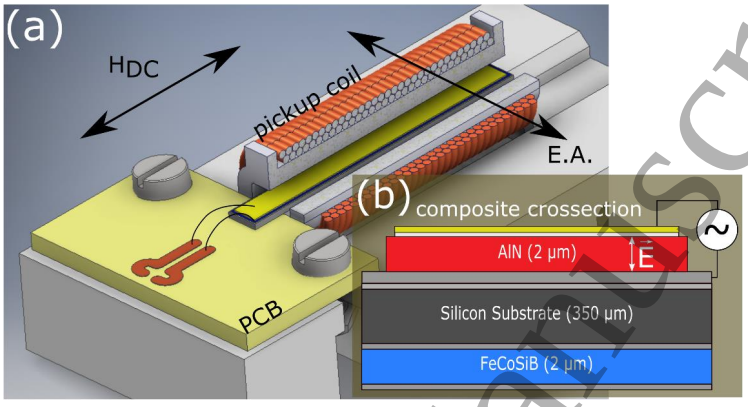

Figure 1 (a) Holder assembly, showing a cutaway view of the pickup coil which is designed to fit around the center of a single side clamped magnetoelectric cantilever beam. The magnetoelectric cantilever is fixed to a piece of FR4 board using cyanoacrylate adhesive, wire bonding is used to contact top and bottom electrodes. The PCB board is fixed to the holder using polymeric screws. An external DC magnetic field may be applied along the long axis of the assembly, orthogonal to the induced easy axis (E.A.). (b) The composite layer structure in schematic crosssection view. On the top side the piezoelectric layer is deposited, being part of a plate capacitor structure. On the bottom side of the double side polished silicon substrate the magnetostrictive layer is deposited.

The converse magnetoelectric effect was measured by applying an alternating voltage to the piezoelectric phase of the magnetoelectric composite which is, free to mechanically oscillate, immersed in a custom made pickup coil, depicted in Figure 1a. The coil holds around N = 1200 windings and matches an R_{DC} = 50 Ohm. The inner dimensions of the elliptical polymeric coil body are 7 mm by 5 mm.

The resonance measurements of the composite were made using an Agilent Technologies 33512B signal generator for application of the driving signal to the AlN and a classic Keithley 2000 series multimeter in AC mode connected to the pickup coil. The magnetic bias field is generated using the

second channel of the signal generator in DC voltage mode in conjunction with a bipolar power supply (KEPCO BOP-3606ML) and a pair of Helmholtz coils, delivering a maximum magnetic field (H_{DC}) of 20 mT. The applied field is measured using a hall probe (Group3 Technology, Ltd.). The magnetic sensitivity measurements were performed in a magnetically and electrically shielded environment, further details concerning the setup can be found in [14]. In this case the time signal of the pickup coil was acquired using a UHFLI of Zurich instruments locked to the high frequency excitation.

For the mechanical characterization of the magnetoelectric composites a laser beam deflection setup is used. The displacement as well as the phase of the cantilever beam motion is detected by a lateral effect photodiode (Hamamatsu) also known as a position sensitive device (PSD) in uniaxial configuration. The signal is amplified by a high speed amplifier (LTC1753) and subsequently fed into a lock-in amplifier (Zurich Instruments HF2LI) which is locked to the excitation frequency set by the signal generator. An X-Y stage (Newport, ESP-301) allows scanning of the cantilever surface and monitoring the lateral deflection amplitude as well as phase. The employed red semiconductor laser had a spot size of about 250 µm. The beam deflection seen by the PSD in the given configuration corresponds to the out-of plane bending of the long axis, as well as motion along the short axis.

Results and Discussion

Figure 2 shows the voltage induced into the pickup coil in the frequency regime below 10 kHz. Without the application of a magnetic bias field essentially only the noise floor of the read-out circuit connected to the coil in the unshielded environment is present, which amounts to about 480 µVrms. Upon application of a magnetic bias field two clear peaks emerge, which can be attributed to the first and second flexural modes of the cantilever. By following the formalism by Cleveland [15] for flexural resonances

$$f = \frac{t}{2\pi l^2}\sqrt{\frac{E}{\rho}} \quad \text{(Eq. 1)}$$

(where *f* is the resonance frequency, *t* is the thickness of the beam, *l* is the free standing length and *ρ* and *E* are the density [16] and Young's modulus [16] of the silicon substrate) for a free standing length of 24 mm and a thickness of 350 µm one finds good agreement of the measured value of 840 Hz with a calculated value of 835 Hz. The flexural resonance modes are spaced non evenly [17], thus a frequency factor of 6.27 [18] is to be expected between the first and the second flexural resonance. With a value of $f_2 = 6.27 f_1 \approx 5232$ Hz it lies within approximately 3 % of the experimentally determined frequency for f_2 = 5360 Hz.

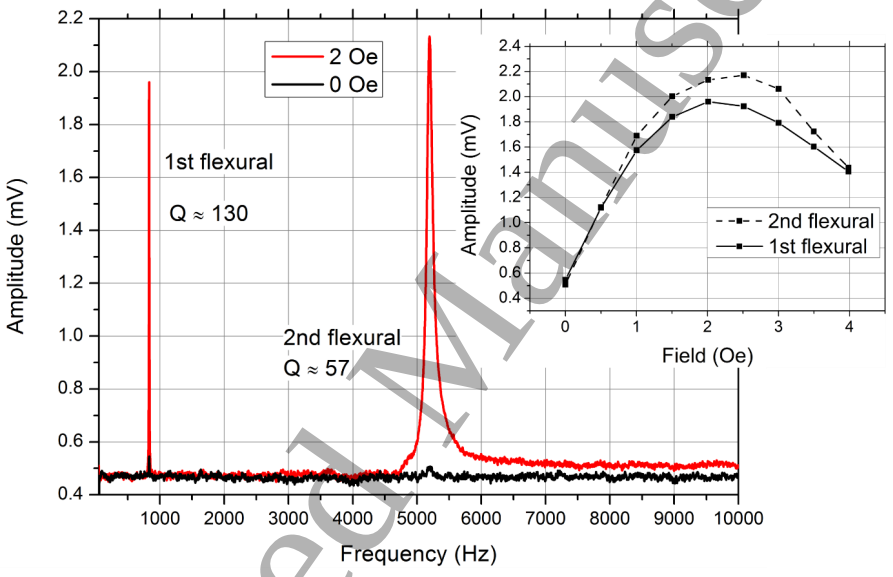

Figure 2: Pickup coil voltage versus excitation frequency of the piezoelectric layer. Exciting the piezoelectric phase with 5V_{pp} without an external magnetic bias field, the induced signal amplitude is rather low, reaching 50 µV above the noise floor of about 480 µV, for the first bending resonance of the cantilever, which is to be seen at 840 Hz. Upon application of a magnetic bias field the induced amplitude increases vastly, reaching an optimum point of 1.96 mV for the first bending resonance at a bias field of 1.86 Oe, the second bending resonance at 5360 Hz exhibits a maximum signal output of 2.17 mV at 2.36 Oe bias field. At field values above the amplitudes decrease again. The quality factor of the first flexural mode is more than twice as large as the one measured for the second mode.

Increasing the magnetic bias field the induced voltage for both modes increases vastly, see Figure 2, inset. At the working point of 2 Oe the induced voltage reaches nearly 2 mV for the first flexural

mode and close to 2.2 mV for the second flexural mode at a slightly higher optimum bias field of 2.5 Oe. Upon further increase of the magnetic field towards the saturation of the FeCoSiB, at a field of about 3 Oe, the induced voltage decreases again. Contrary to the expectation that the mechanical quality factor of the second flexural mode is higher than for the first [19], it is seen to decrease to half its value, this has its origin in acoustic radiation losses [20], as it is highly audible. In Figure 3a wider frequency range from 10 kHz to 800 kHz is shown using the same excitation amplitude of 3 Vpp. Even at no applied magnetic bias field one can observe a very broad peak with a comparably low quality factor of Q ≈ 27 at 175 kHz. It is possible that this resonance is comprised of two or more resonances, leading to a broadening of the peak in the measurement. Upon application of a bias field corresponding to the value of the working point of the first flexural mode, the induced voltage difference is less than threefold, rendering this mode unsuitable for magnetic field sensing purposes. Figure 3b shows a zoom of two remarkable peaks in terms of induced voltage amplitude, peak T1 exhibits a strong nonlinearity and an induced voltage of nearly 500 mV, the peak T2 induces a maximum of 130 mV but shows rather harmonic behavior at the given excitation voltage of 3 Vpp. The quality factors of the oscillations T1 and T2 amount to roughly Q ≈ 1300 at zero applied magnetic bias field.

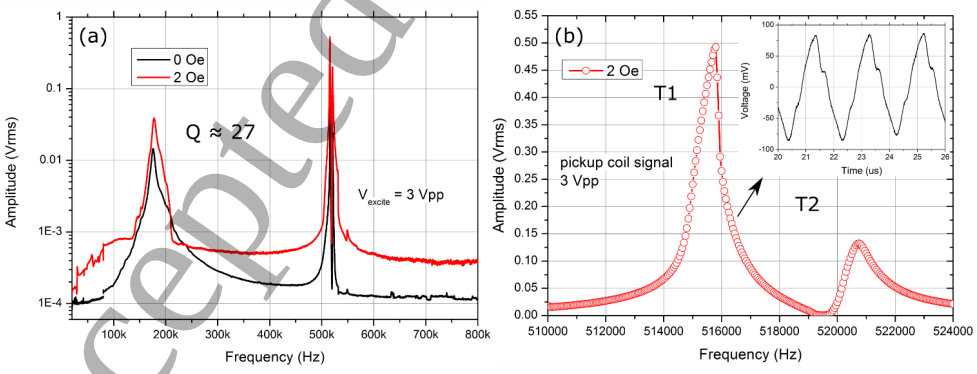

Figure 3 (a) shows the induced voltage for an excitation frequency range of 10 kHz to 800 kHz and an excitation amplitude of 3 Vpp. Without magnetic bias field and with a bias field close to the optimum working point bias field needed for the 1st and 2nd flexural modes, Figure 2. Besides a very broad peak at 175 kHz two closely spaced peaks at 515.7 kHz and 520.7 kHz can be seen in the

spectrum. (b) shows the induced voltage at the working point of two high frequency vibration modes near 515.7 kHz and near 520.7 kHz, indicated by T1 and T2. The inset shows the inharmonic time domain voltage response of T1 mode. The induced voltage is about three orders of magnitude higher than that for the 1st and 2nd flexural mode (figure 2).

The fact that the oscillatory mode T1 shows such a strong nonlinearity in the induced voltage, see Figure 3b inset, makes it non straightforward for use in magnetoelectric sensors, as a linear response towards the magnetic field is desirable. Therefore, from here, the focus is laid on the T2 mode of oscillation. Figure 4a, relates the induced voltage of the T2 oscillation to the applied magnetic bias field. Coming from the negative saturation, the induced voltage increases steadily and amounts to a maximum value of nearly 140 mV at a bias field of -1.6 Oe, decreasing the field further decreases the induced voltage until reaching zero, at zero bias field. Note that while approaching a bias field of zero, a high sensitivity towards the external field is observed. A value of 2290 V/T is observed coming close to zero from negative saturation.

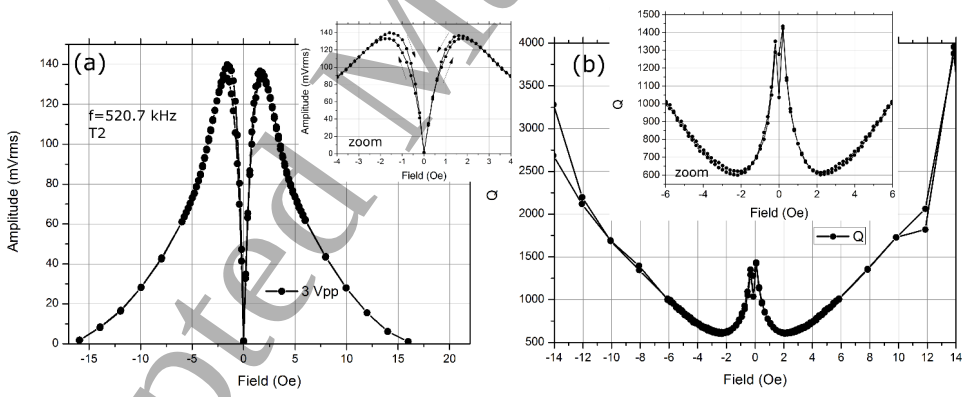

Figure 4 (a): Loop of the induced voltage vs. magnetic field for the T2 mechanical mode. At 0 Oe the induced voltage is near zero, reaching its maximum at about 140 mV at a magnetic bias field of -1.6 Oe. Towards small fields the initial slope is up to 2290 V/T. At a bias field of 16 Oe the amplitude again reaches to zero. The field step size in the region below a magnitude of 6 Oe is 0.2 Oe. (b) The quality factor of the vibration with respect to the magnetic bias field. At zero bias field the Q factor is 1030 and 1270, depending on the magnetic history. The minimum Q factor of about 600 is reached at a field magnitude of 2.2 Oe. Towards saturation fields, the Q factor rises above 2000 for bias fields greater than 12 Oe.

When crossing zero the initial slope is lowered to 1685 V/T. Note that the voltage measured in this measurement is taken from a broad spectrum by the AC multimeter. On looping back, hysteresis is observed, lowering the peak amplitude by about 5 %. It is expected that a magnitude of 16 Oe is not sufficient to entirely saturate the ferromagnetic film. The quality factor of the induction caused by the oscillation is shown in Figure 4b, also taken from a field loop measurement. It is a strong function of applied magnetic field exhibiting a rather unstable value of about 1000 to 1400 at no applied bias. Upon field application, the quality factor symmetrically drops by about 40 % until reaching a minimum value of 600 at a field magnitude of 2.2 Oe. Further increasing the magnetic field leads to a steady increase of the quality factor, reaching approximately its initial value at a field magnitude of 8 Oe, climbing to 3800 near magnetic saturation. The initial reduction in quality factor gives rise to increased losses of the mechanical oscillation as observed by [21]. These losses are attributed to the energy spent for the magnetization change induced by inverse magnetostriction.

The amorphous magnetostrictive phase was heat treated in a magnetic field, as described in the methods section, in order to induce a magnetic easy axis, as pointed out in Figure 1a. Thus the maximum magnetoelastic response is obtained when a magnetic field or strain is applied along the long axis of the cantilever. Amorphous FeCoSiB is known for high magnetostriction coefficient of about 30 ppm [22], as well as soft magnetic properties, resulting in a favorably high piezomagnetic coefficient. The employed AlN shows a strictly linear displacement-voltage characteristic as published previously [4, 23], thus it will linearly convert the excitation signal into displacement and subsequently into stress.

The change in magnetization by the periodically induced piezoelectric strain leads to a change of the magnetic flux within the coil, leading to an induced voltage by the relation [24] , extended as Eq. 1

$$U_{ind} = -N\frac{d\phi}{dt} \propto \int_V \frac{dM}{d\sigma_m}\frac{d\sigma}{dE}\, dV \quad \text{Eq. 1}$$

Where U_{ind} the induced voltage, N number of coil turns of the pickup coil, φ magnetic flux density, t the time, M the magnetization, σ_m the stress in the magnetic phase and E the electric field present in the piezoelectric material.

Qualitatively, at no applied field the magnetization is free to be governed by the piezoelectrically exerted strain, wherein the applied stress can be viewed as an uniaxial anisotropy acting on the magnetization configuration. The magnetization change alone does not necessarily lead to an induced voltage signal, as the net magnetization change within the volume can sum to zero. At the field of minimum quality factor it is expected to experience a maximum of directed change (direction given by applied magnetic field) in magnetization, hence a maximum amplitude of induced voltage is observed. At even higher magnetic fields the magnetization is increasingly governed by the energy of the applied magnetic field, rendering losses low. It is worth noting that there is a mismatch of 0.6 Oe between the maximum of induced voltage (Figure 4a) and the minimum of the quality factor at a field magnitude of 2.2 Oe (Figure 4b). This mismatch is attributed to have micro-magnetic origin, in that not every strain mediated magnetization change will contribute to the measured voltage signal in the pickup coil. The quality factor of the T2 mode is nearly fivefold of the F1 flexural mode at equal magnetic bias field, indicating that the dominant loss mechanism at ambient pressure conditions for the aspect ratio (length/width) of about 10, is limited due to the motion of its large surface area against the quasi viscous ambient atmosphere [19]. On the other hand the quality factor of flexural vibrations is known [25] to rise with increasing mode number, giving evidence to a high mode of torsional or flexural vibration.

In order to obtain an idea of the mechanical form of vibration, an estimation of the oscillation mode T2 is necessary. From (Eq. 1) and [17] , by a simple analytical estimation, it follows that the 15th flexural mode of vibration, has a frequency of $f_{f,15} = 493.4\ \mathrm{kHz}$ which is as close as 5 % to the measured frequency of 520.7 kHz. Equally, the 19th torsional mode has a frequency according to [17] $f_{t,19} = \frac{2n-1}{2}\frac{1}{l}\frac{b}{a}\sqrt{\frac{G}{\rho}}$ of $f_{t,n=19} = 18.5 \cdot 28.4\ \mathrm{kHz} = 525.4\ \mathrm{kHz}$, where n denotes the mode number, G

the shear modulus of 50.9 GPa [16] and ρ the density, b and a the beam thickness and with, respectively. This mode is as close as 0.7 % to the measured value. It has to be noted that intuitively it should not be possible to excite a flexural vibration of such high order modes nor a torsional vibration, using a simple plate capacitor arrangement without having a patched, electrode design on the piezoelectric film.

In order to clarify the dominating mechanical oscillation, mechanical vibration measurements were performed. Figure 5 shows a line scan along the long axis of the cantilever, at approximately one quarter of its width. Choosing one quarter of the width proved to give a clear signal of the expected oscillation maxima along the long axis. The mechanical phase of the T2 oscillation shows a nodal point, where the phase is reversed and the oscillation amplitude reaches zero at a length of roughly 16 mm, which corresponds to about 70 % of its free length. The total number of oscillation maxima at 2 mm, 5 mm, 8.5 mm 11.3 mm, 14.2 mm as well as 17.9 mm and 20.5 mm, totaling seven phase bumps. This is in good qualitative agreement to the findings of van Rensburg [26] for a flexural mode of the 15th order. The oscillation period is approximately 3 mm for the first five maxima. The high noise near the clamped end, below 1 mm as well as the maximum at 22.7 mm at the very tip, are considered as artifacts caused by the low signal amplitude and the finite laser spot size interacting with the free edge of the cantilever, respectively. Figure 6 gives a 3-dimensional representation of the oscillation magnitude as well as its phase. The asymmetry of the phase towards the center line, clearly evinces a mixed mode of oscillation, comprising most likely torsion and flexing of the beam. Possibly they coincide and the combination is responsible for a large change in magnetic flux density und thus leads to a pronounced induced voltage of up to 140 mV.

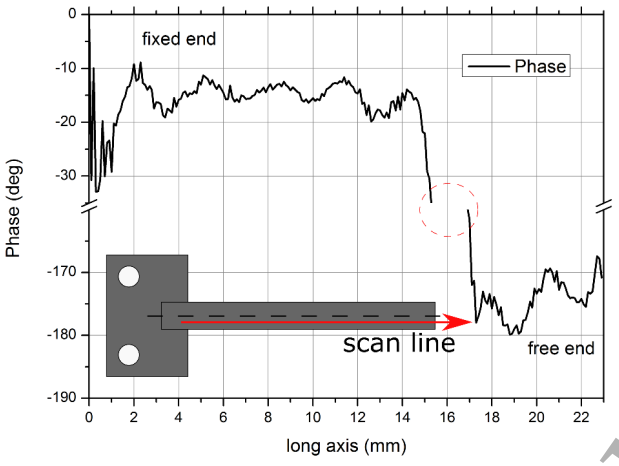

Figure 5: Vibration measurement showing the mechanical phase of the cantilever beam under piezoelectric excitation at the T2 resonance frequency of 520700 Hz. The cantilever is scanned along the long axis at about one quarter of its width, as indicated on the inset sketch, the dashed line shows the center line. At 70 % of its length (indicated by the dashed circle) there is a nodal point where the amplitude (not shown) drops to zero and the phase is effectively reversed. In total seven maxima can be observed along the cantilever line.

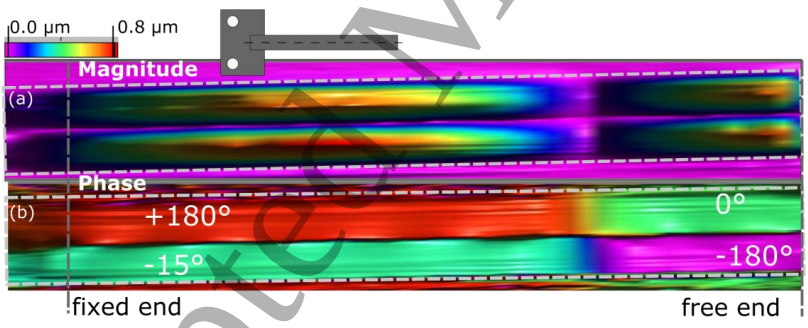

Figure 6: Vibration measurement of the cantilever beam under piezoelectric excitation in the T2 resonance frequency of 520720 Hz. The dashed lines indicate the cantilever outlines, the outer areas stem from the rigid sample stage. The measurements are comprised of line scans along the short axis with a step size of 50 µm, a step size of 500 µm towards the long axis. (a) Shows the Magnitude, corresponding to the displacement as measured by the lock-in amplifier. No displacement is measured along the center line, as well as at a nodal line at 70 % of the length, along the short axis. (b) Shows the phase of the oscillation. Most prominent is a phase reversal between the left and right side of the center line, which again occurs near the free end at 70 % length. A ripple, corresponding to phase variations, along the long axis is visible.

Measurements to estimate the magnetic sensitivity towards low frequency magnetic fields were performed by placing the assembly, shown in Figure 1, into a shielded environment, a magnetic saturation field of about 50 Oe was applied prior to the measurements. A slowly varying sinusoidal test signal at 200 mHz at several amplitudes is applied using an additional coil. No dc bias field is present during this measurement. The piezoelectric phase of the magnetoelectric composite is driven with a carrier signal amplitude of 3 Vpp at 520.7 kHz and the induced voltage signal of the pickup coil is recorded by a lock-in amplifier. The amplifier was set to a filter of 18 dB/oct and a -3dB point of 6.27 Hz. Switching off the carrier signal did not lead to any measurable voltage signal at the magnetic signal frequency. Figure 7 shows the frequency domain representation of the recorded time series in order to estimate the sensor resolution. The average noise around the carrier signal amounts to -143.7 dBV or 65 nVrms. A sinusoidal magnetic test signal with an amplitude of 7.07 nTrms results in a voltage amplitude of 377 nVrms, leaving a signal-to-noise margin of 5.8, resulting in a minimum detectable field of 1.2 nT.

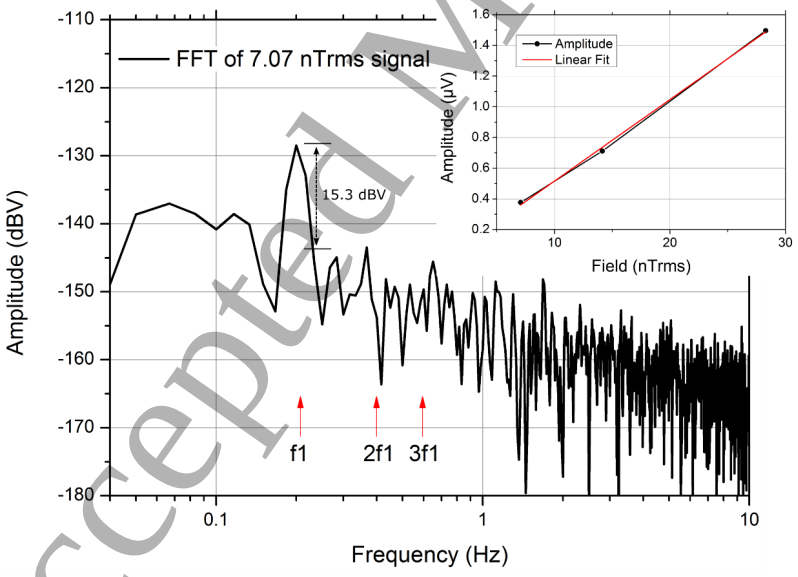

Figure 7: Measurement showing an FFT to estimate the noise margin of a slowly varying sinusoidal test signal of 200 mHz with an amplitude of 7.07 nTrms. Linearity is inferred by the absence of

13

harmonic components at 2f1 and 3f1. A signal margin towards the noise floor of 15.3 dBV corresponds to a resolution of 1.2 nT. The inset shows the signal linearity for three different test signal amplitudes.

Conclusion

Concluding, this study reports on measurements of converse magnetoelectric interactions by combining mesoscale thin film cantilever beams with pickup coil readout, a method classically applied to macroscopic laminate magnetoelectric composites [27], [28]. Apart from the first and second flexural modes of oscillation exploited in previous studies [23, 29], two high order modes at 515.7 kHz and 520.7 kHz were found to induce voltages up to 500 mV and 140 mV, respectively. The mode at 520.7 kHz follows harmonic induction characteristics, as well as high magnetic field dependency of the induced voltage, giving an initial slope of 2290 V/T. Vibrational measurements are in good agreement with analytic estimations as well as literature, indicating that both the 15th flexural mode and/or the 19th torsional mode might be the active modes of this oscillation. A corresponding measurement towards small DC magnetic fields demonstrates a linear resolution of 1.2 nT at 200 mHz in the absence of a magnetic bias field. Our first study on this arrangement of ME composites makes this approach to low frequency fields already as good as AMR sensors [11]. Furthermore, this kind of arrangement is well suited for use in sensor arrays.

Acknowledgements

The authors would like to thank the German Research Foundation (Deutsche Forschungsgemeinschaft, DFG) who funded this work under Collaborative research centre SFB1261 “Biomagnetic Sensing”.

Special thanks to B. Spetzler for fruitful discussions concerning mechanical oscillations and to P. Durdaut for discussions about the magnetic resolution measurements.

References

[1] Trolier-McKinstry S and Muralt P 2004 *Journal of Electroceramics* **12** 7–17

[2] Quandt E and Ludwig A 1999 *Journal of Applied Physics* **85** 6232–7

[3] Nan T, Hui Y, Rinaldi M and Sun N X 2013 *Scientific reports* **3** 1985

[4] Yarar E, Hrkac V, Zamponi C, Piorra A, Kienle L and Quandt E 2016 *AIP Advances* **6** 75115

[5] Hiltunen T *et al* 2014 *The Journal of neuroscience : the official journal of the Society for Neuroscience* **34** 356–62

[6] Kwon J S, O'Donnell B F, Wallenstein G V, Greene R W, Hirayasu Y, Nestor P G, Hasselmo M E, Potts G F, Shenton M E and McCarley R W 1999 *Arch Gen Psychiatry* **56** 1001

[7] Petrie J, Gray D, Viehland D, Sreenivasulu G, Srinivasan G, Mandal S and Edelstein A S 2012 *Journal of Applied Physics* **111** 07C714

[8] Mermelstein M D 1992 *IEEE Trans. Magn.* **28** 36–56

[9] Dong S, Zhai J, Li J and Viehland D 2006 *Appl. Phys. Lett.* **88** 82907

[10] Burdin D, Chashin D, Ekonomov N, Fetisov L, Fetisov Y and Shamonin M 2016 *J. Phys. D: Appl. Phys.* **49** 375002

[11] Stutzke N A, Russek S E, Pappas D P and Tondra M 2005 *Journal of Applied Physics* **97** 10Q107

[12] Yarar E, Salzer S, Hrkac V, Piorra A, Höft M, Knöchel R, Kienle L and Quandt E 2016 *Appl. Phys. Lett.* **109** 22901

[13] Hrkac V, Lage E, Köppel G, Strobel J, McCord J, Quandt E, Meyners D and Kienle L 2014 *Journal of Applied Physics* **116** 134302

[14] Jahns R, Knöchel R, Greve H, Woltermann E, Lage E and Quandt E 2011 Magnetoelectric sensors for biomagnetic measurements *Medical Measurements and Applications Proceedings (MeMeA), 2011 IEEE International Workshop on* pp 107–10

[15] Cleveland J P, Manne S, Bocek D and Hansma P K 1993 *Review of Scientific Instruments* **64** 403–5

[16] Hopcroft M A, Nix W D and Kenny T W 2010 *J. Microelectromech. Syst.* **19** 229–38

[17] Reinstaedtler M, Rabe U, Scherer V, Turner J A and Arnold W 2003 *Surface Science* **532-535** 1152–8

[18] Gates R S, Osborn W A and Pratt J R 2013 *Nanotechnology* **24** 255706

[19] R. N. Candler, H. Li, M. Lutz, W. T. Park, A. Partridge, G. Yama and T. W. Kenny 2003 Investigation of energy loss mechanisms in micromechanical resonators *TRANSDUCERS, Solid-State Sensors, Actuators and Microsystems, 12th International Conference on, 2003* 332-335 vol.1

[20] Lochon F, Dufour I and Rebière D 2005 *Sensors and Actuators B: Chemical* **108** 979–85

[21] Zabel S, Kirchhof C, Yarar E, Meyners D, Quandt E and Faupel F 2015 *Appl. Phys. Lett.* **107** 152402

[22] Kwang-Ho Shin, Mitsuteru Inoue and Ken-Ichi Arai 2000 *Smart Materials and Structures* **9** 357

[23] Hayes P *et al* 2016 *Appl. Phys. Lett.* **108** 182902

[24] Fetisov Y K, Petrov V M and Srinivasan G 2007 *J. Mater. Res.* **22** 2074–80

[25] van Eysden C A and Sader J E 2007 *Journal of Applied Physics* **101** 44908

[26] van Rensburg NFJ and van der Merwe A J 2006 *Wave Motion* **44** 58–69

[27] Bichurin M I, Petrov V M and Petrov R V 2012 *Journal of Magnetism and Magnetic Materials* **324** 3548–50

[28] Dong S, Li J F, Viehland D, Cheng J and Cross L E 2004 *Appl. Phys. Lett.* **85** 3534–6

[29] Piorra A, Jahns R, Teliban I, Gugat J L, Gerken M, Knöchel R and Quandt E 2013 *Appl. Phys. Lett.* **103** 32902

3.1 Conclusion

Using these U1 and U2 called mechanical modes requires less excitation amplitude, while still leading to stronger modulation of the magnetostrictive phase than offered by the first flexural mode, previously presented in section 2 on page 25. Inherently using high frequency modes, the available bandwidth is increased from about 4 Hz to at least 200 Hz, see section 4. Signals of very low frequency of 200 mHz were readily detected using U2 mechanical mode in conjunction with pickup coil readout. High carrier amplitudes on the order of Volts are required in order to achieve high performance.

3.2 Vibrometry Study

In order to shine light onto the mechanical side of those high frequency vibration modes, measurements using a high speed vibrometer *Polytec UHF-120* at the IFW[2] during a field trip to Dresden were performed. For these measurements the PCB mounted silicon die is fixed on a X-Y sample stage in a flipped fashion as to have the vibration information directly from the magnetostrictive layer, as shown in figure 3.1a. The vibrometry setup is magnetically unshielded. The exact details of the investigated composite are given in [Hay+18]. The laser spot diameter is less than 10 µm using a 5x lens, performing an areal scan using a grid of 109x9 points leads to a spacing of 270 µm as shown in figure 3.1b. Fortunately it was possible to scan the complete cantilever length of about 22 mm without refocusing, which is needed for samples which are not entirely planar on the sample stage. Multicarrier vibrometry measurements employing a vector signal generator *Rohde & Schwarz SMBV100A* allows to retrieve a complete out-of-plane displacement spectrum containing 6400 FFT lines with known phase relation for each point of the defined measurement grid, unfortunately the control software limited measurements to frequencies above 100 kHz. The span for this FFT was set to 100 ... 800 kHz, resulting in a linewidth of 156.25 Hz, the excitation voltage is constant per FFT line. Displacement spectra of the points 1,2 and 3 indicated on the measurement grid in figure 3.1b are shown in figure 3.2 on page 57. In these spectra every peak corresponds to a mode of oscillation, more precisely its out-of-plane component at that specific geometric location and frequency. Point 3 may be regarded as the most characteristic location as it corresponds to the central point of the free cantilever end. Point 1 and 2 are arbitrarily chosen, off-axis points in order to gain a broad comparison of the overall displacements within the scan range. Averaging information over those geometric points was disregarded because this is believed to yield unphysical information.

[2]Leibniz-Institut für Festkörper- und Werkstoffforschung

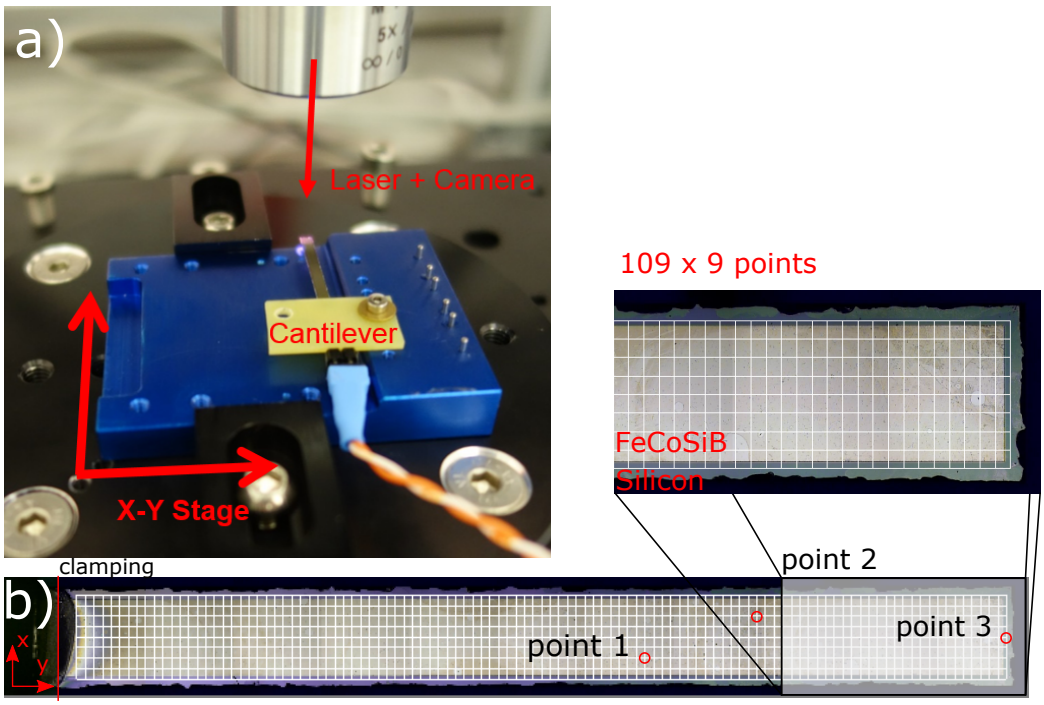

Figure 3.1: Laser Scanning Vibrometry. a) Setup showing ME cantilever mounted to an X-Y stage. The piezoelectric AlN is connected to a vector signal generator. b) Camera image of the full cantilever with superimposed grid, intersections indicate measurement points. Clamping to the PCB is on the left, the first data point is taken about 500 µm away from the clamping. The borders of the cantilever seem rough, during wafer dicing this side faces the chuck towards which a height margin is kept, hence leading to random fractures of the remaining 30 µm of Silicon. The indicated points 1, 2 and 3 are used for further analysis.

The information extracted from those three points qualitatively conveys the same message in that the four peaks at 516.25 kHz, 522.5 kHz, 533.4 kHz and 548.75 kHz are oscillations showing the strongest out-of-plane contributions, these oscillations are called U1 to U4 oscillation. The first two, U1 and U2 oscillations show an order of magnitude higher displacements than U3 and U4 mode. Any other modes show again at least an order of magnitude reduced displacements. U1 achieves a peak displacement of 4.35 nm at its tip end and an associated mechanical quality factor of about 1400 in unshielded conditions. U2 mode is similar, showing a Quality factor of 1200, U3 and U4 modes are about half 550 and 660, respectively.

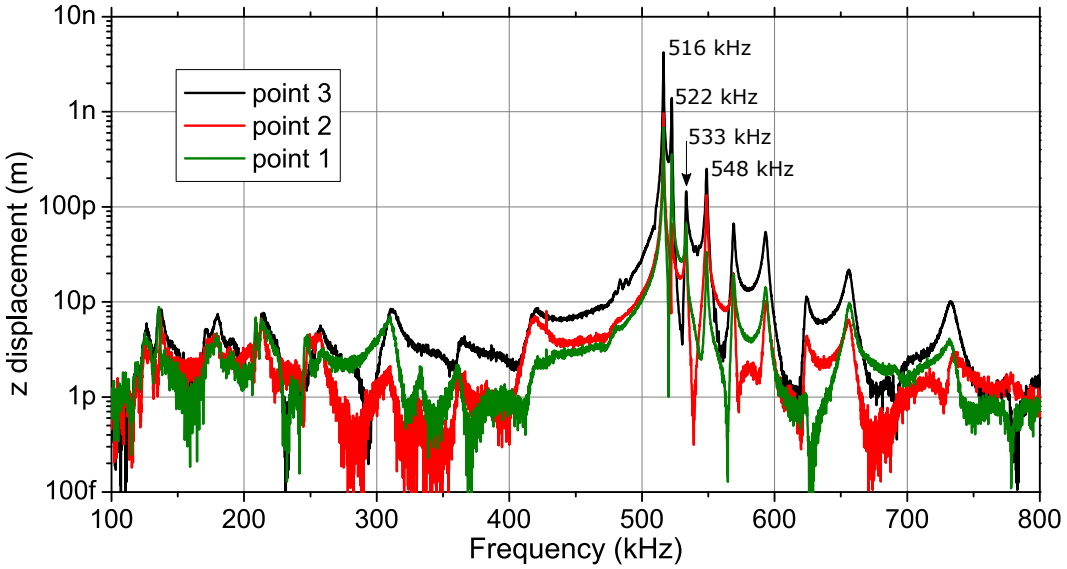

Figure 3.2: Displacement spectrum taken from the points indicated in figure 3.1b. Point 3 represents the tip of the cantilever, the other two points 2 and 1 are randomly chosen to demonstrate the validity of the spectrum concerning the entire vibration.

The exact deformation shapes extracted from measurements to these four modes are illustrated as contour plots in figure 3.3 on the next page, the color code indicates displacement, red and blue associated to maxima with opposing sign. Between adjacent displacement maxima nodal lines can be observed, where the displacement is necessarily zero, this holds true for the short (x) as well as the long (y) cantilever axis. The first mode is the fundamental U oscillation and has no nodal lines parallel to its x-axis.

A y-axis line scan along the center of the cantilever for U1 oscillation mode is shown in figure 3.4 on page 59. The displacement along the y-axis increases towards the free end, as is indicated by the dashed line fit for a parabola. Note that the scales differ by seven orders, so this parabolic flexion leads to vanishingly small resulting stress. Furthermore, a superimposed oscillation along the y axis, is revealed in displacement as well as its phase information. There are seven periods of a flexural oscillation overlaying this primary oscillation, creating about 200 pm ripple peaks. However, the straightforward

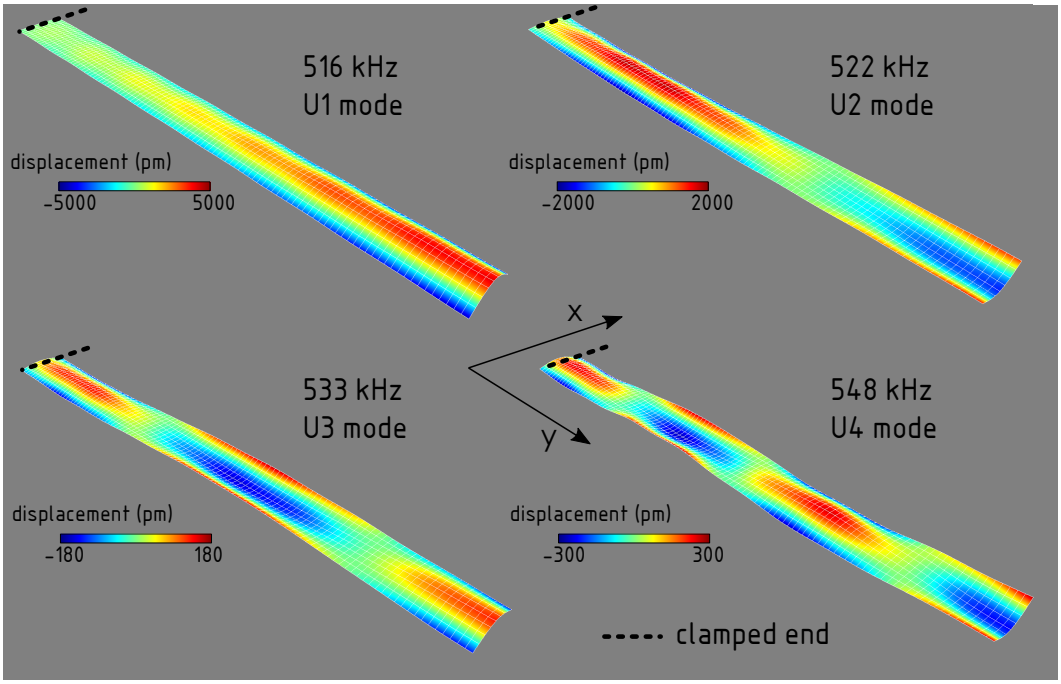

Figure 3.3: Contour representations taken from vibration spectroscopy measurements, as indicated in figure 3.2 on the previous page. Four vibration modes showing by far strongest out-of-plane displacements, all members of the U mode family, have main oscillation components about the short cantilever axis. Nodes in the mechanical displacement form between red and blue regions. Note the strongly decreasing value of the scale.

deduction that this stems from the 8th flexural oscillation being simultaneously active is misleading, as this resonant frequency would amount to only about 140 kHz.

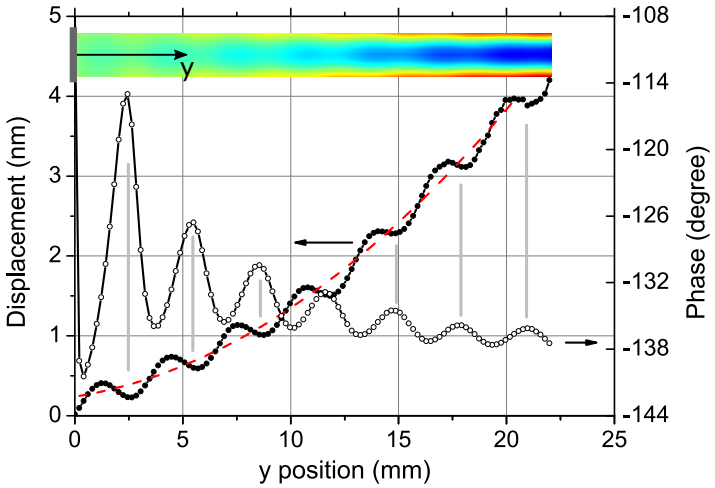

Figure 3.4: Linescan for the U1 mode. Scan line along the center of the cantilever showing the rms displacement and its phase relative to the excitation. A nearly linear increase in displacement towards the free end is visible. A pronounced ripple along the length is visible, showing seven periods of oscillation, seen in displacement as well as phase.

Figure 3.5 on the next page shows the same analysis for the second strongest, U2 mode, indicating its maximum displacement of about 1.75 nm at already 7 mm distance off the clamping. Noteworthy is the existence of a mechanical node at about 70 % of the cantilevers length, at which the oscillation phase is reversed, leading to displacement pointing along the opposite z direction. U3 and U4 mode exhibit two and three such nodal lines along x axis, respectively. Furthermore, this investigation of a central line for oscillation mode U2 also indicates presence of the same flexural ripple as found in figure 3.4, it is slighly obscured by the scaling.

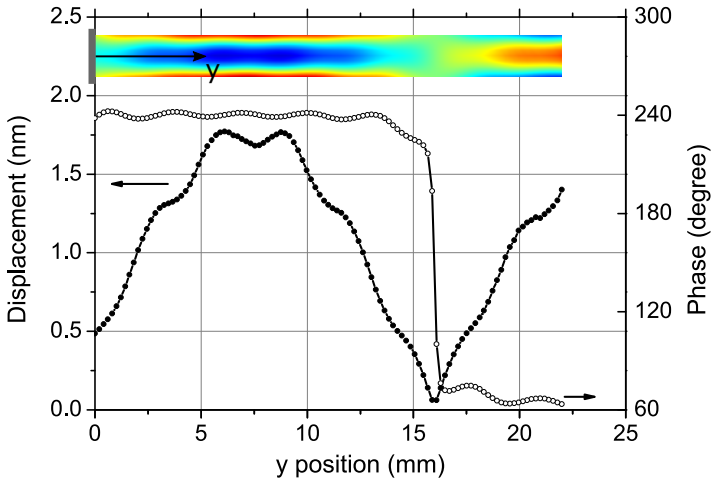

Figure 3.5: Linescan for the U2 mode. Scan line along the center of the cantilever showing the rms displacement and its phase. The maximum displacement is already reached at about 7 mm or 30 % of the free length. A phase reversal occurring at a node located at about 16 mm or 70 % of the free length leads to a sign change in the displacement.

3.3 Mode Analysis using Finite Element Simulations

As the analytical description and therefore modelling of the U mode family is not straightforward, simple Finite Element Method (FEM) simulations using *Abaqus CAE 2018* were performed. The simulations were carried out using a single slab of 350 µm thick silicon material assuming the silicon substrate dominates the mechanical response, since active layers are negligibly thin. These mode analysis simulations were performed irrespective of a piezoelectric material, thus they indicate the presence of a mechanical mode but not necessarily its practical excitability. A rectangular area on one face of the composite was fixed by a boundary condition, similar to gluing the composite to a PCB in the experiment. Figure 3.6 on the facing page shows the U mode family from U1 at 517.3 kHz to U4 mode at 556.7 kHz, for constant geometry with a thickness $t = 350\,\mu\text{m}$ a width $w = 2.38\,\text{mm}$ and a length $l = 25\,\text{mm}$, nominally matching the experiment. The color code shows the Mieses stresses red according to strong tensile stress, deep blue being maximum compressive. Compared to the vibrometry measurement shown in figure 3.3 on page 58 the deviation between experimentally determined and simulated resonance frequencies is very small, being largest at 1.6 % for U4 mode resonance. The experimentally observed ripple pattern along the length of the cantilever (figure 3.4) also appears in the simulation results for all identified U modes. The geometric parameters of width and composite thickness play a crucial role for the U mode resonance frequencies, intuitively thicker substrates leads to higher frequencies as the restoring force is stronger. Equally, one may expect a larger width to relax the resonance frequency to lower values, since the curvature involved in the

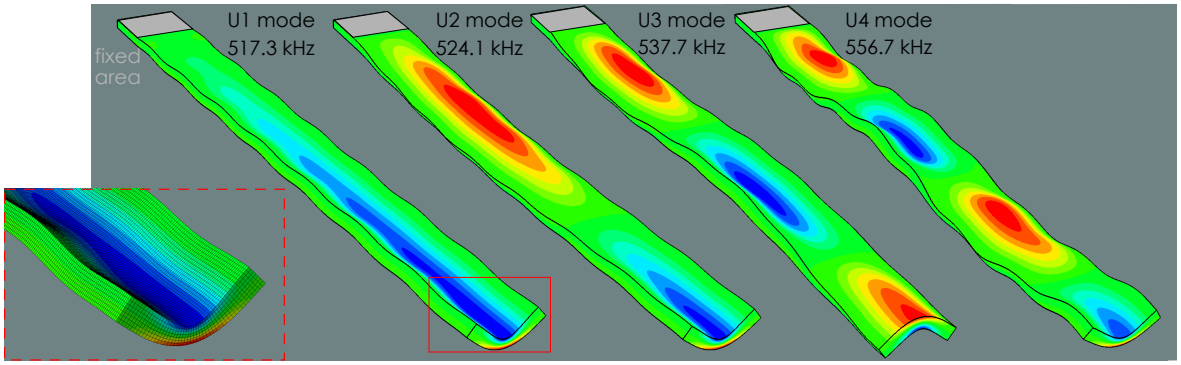

Figure 3.6: FEM simulation of the U mode family and their respective resonance frequencies rising with the number of occurring mechanical nodes. Color code shows von Mieses stress; red tensile, blue compressive. The indicated area is rigidly fixed by boundary condition. The inset shows a homogeneous mesh consisting of 50 µm cubes.

oscillation needs not to be as large. Figure 3.7 shows simulations of the U1 and U2 mode frequency for the variation of (a) width and (b) thickness of a composite with otherwise constant geometry, the mentioned qualitative intuitions are confirmed. A weak parabolic fit matches the resulting data well. The substrate width strongly influ-

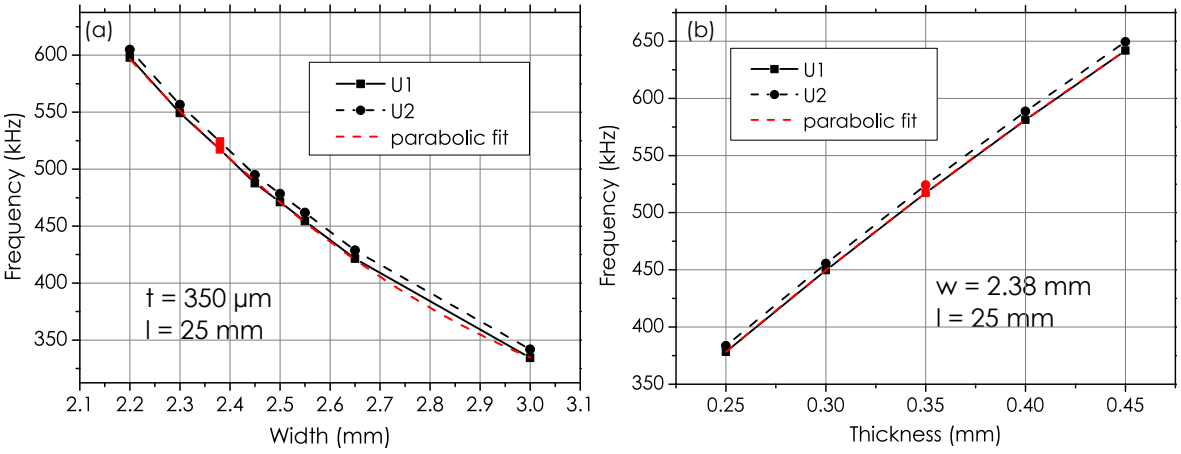

Figure 3.7: FEM results showing U1 and U2 mode resonance frequency for (a) varying composite width (b) varying composite thicknesses. Remaining parameters are kept constant at values matching experiments. Red data points indicate the experimentally studied geometry.

ences the resulting resonance frequency, a change of 30 % already shifts the resonance frequency by nearly 200 kHz. Fortunately in this work the two critically frequency determining dimensions of width and thickness are exclusively determined by precision machinery and thus only spread within tight limits. The manually controlled parameter of free-standing cantilever length is rather uncritical as simulation results confirm in figure 3.8 on the following page. In the interval of 21 mm to 29 mm length the frequency shift is of oscillatory nature and does not deviate by more than 1.2 %. Finally,

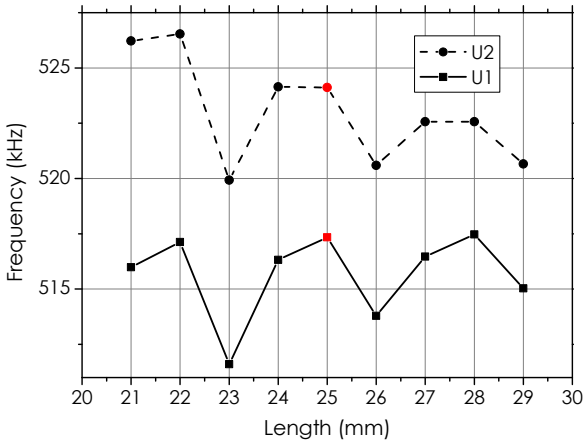

Figure 3.8: FEM results showing U1 and U2 mode resonance frequency for varying cantilever lengths. An oscillatory behaviour is found. Red data points represent experimentally found data.

an impedance measurement across eight nominally equal samples shows only minute deviation of 0.7 % for the resonance frequency of the U1 mode and 0.9 % for the U2 mode resonance frequency, the phase of the measurements is presented in figure 3.9. The quality factors for U1 mode lie at about 1600 one sample being the exception showing a q of only 960.

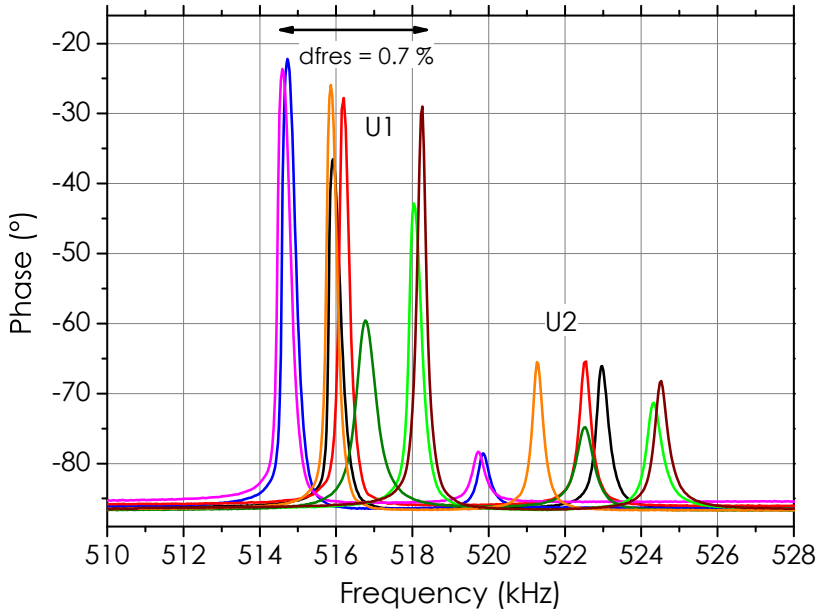

Figure 3.9: Phase measurements on the piezoelectric phase of eight cantilevered samples showing their electromechanical response. The samples are nominally identical. U1 mode shows pronounced phase changes of up to 60 °, whereas U2 mode shows about 20 °. The variance in resonance frequency for U1 mode does not exceed 0.7 %.

3.4 Local Induction Study

This chapter attempts to gain insight to the converse magnetoelectric part and correlate it with the purely mechanical measurements. A strong experimental collaboration with Dr.-Ing. Alexander Teplyuk enabled the results of this section. For this purpose a small coil with about $N \approx 20$ windings mounted on a movable shaft and directly connected to a lock-in amplifier (*HF2LI, Zürich Instruments*), whereas the excitation output is connected to the piezoelectric phase and the pickup coil is fed into the high impedance signal input. The resonance frequency of the local pickup coil is in the range of several MHz, thus within the employed range its response is linear. A *MATLAB* script sets the positioning of the coil by a stepper motor in increments of 500 µm and records an amplitude and phase sweep for each position along the cantilever. The small sliding coil as well as a mounted cantilever sample is shown in figure 3.10 on the next page.

The piezoelectric AlN is excited with a voltage of 1000 mV for this study. Figure 3.11 on page 65 shows the locally induced coil voltage as the composite is excited by a frequency sweep of fixed amplitude, U1 and U2 mode at approximately 517.9 kHz and 524.2 kHz are visible in all traces. At about 8 mm from the clamping, the induced voltage of U2 mode exceeds that of U1 mode. This can be understood by comparison of the mechanical displacement line scan for the U2 mode, given in figure 3.5, at 7 ... 8 mm the displacement is maximum. Moving the coil about 11 mm away from the

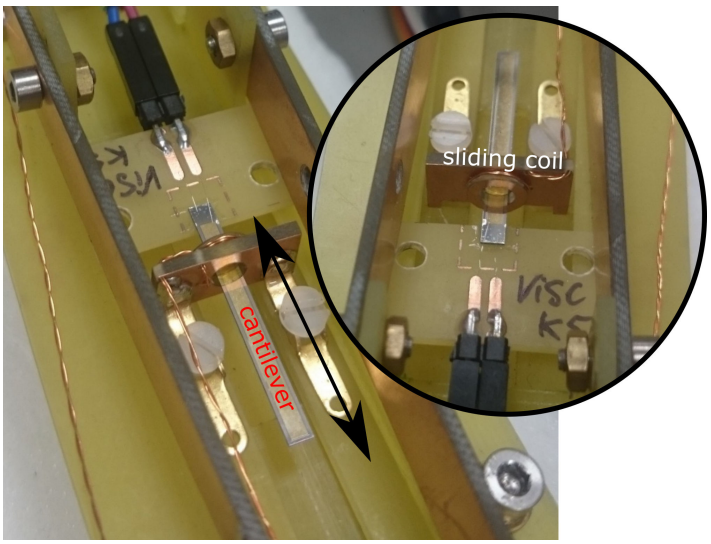

Figure 3.10: Assembly holding a tiny, slidable coil of 4 mm inner diameter with 20 windings entirely made of FR4 material. The shaft (located below) allows the coil to move along the y axis of the cantilever as indicated by the arrow, enabling local pick up of flux changes.

fixed end leads to approximately equal induced voltage amplitude for U1 and U2 mode. This finding is in good agreement with the measured displacement of roughly 1.5 nm for both modes at 11 mm in figure 3.4 and figure 3.5. As the cantilever is homogeneous with respect to its cross-section an equal displacement will result in an equal stress acting. At 18 mm, towards the free end of the cantilever the induced voltage of U1 mode clearly dominates the sweep response, making U2 only faintly visible. For this last measurement there is a phase difference of about 70 ° between both oscillations, this phase difference agrees with mechanical measurements.

Analogous to the mechanical line scans for U1 and U2 mode presented in figure 3.4 on page 59 and figure 3.5 local induction scans were performed, the results of which are shown in figure 3.12 on page 66. Figure 3.12a U1 mode induction amplitude monotonically increases until reaching a maximum of 410 µV around 18 mm, from here the amplitude decays rapidly, extending into free space past the cantilever tip at 20.5 mm. The total phase change is less than 10 °. For U2 mode figure 3.12b induced voltage the situation changes, as the absolute maximum exceeding 300 µV is already reached from 7 ... 9 mm. Then at about 17.5 mm the induced voltage reaches a minimum associated with a phase reversal of the induced voltage at the tip region. A second maximum with opposing phase is found close to the free end.

U1 mode may be read out by using a simple long pickup coil employing constant or slightly modified winding density. Using the same coil for U2 mode will lead to partial cancellation of the induced voltage due to their antiphase relation. Having a mechanical node, U2 mode requires either one simple pickup coil up to the nodal line at about

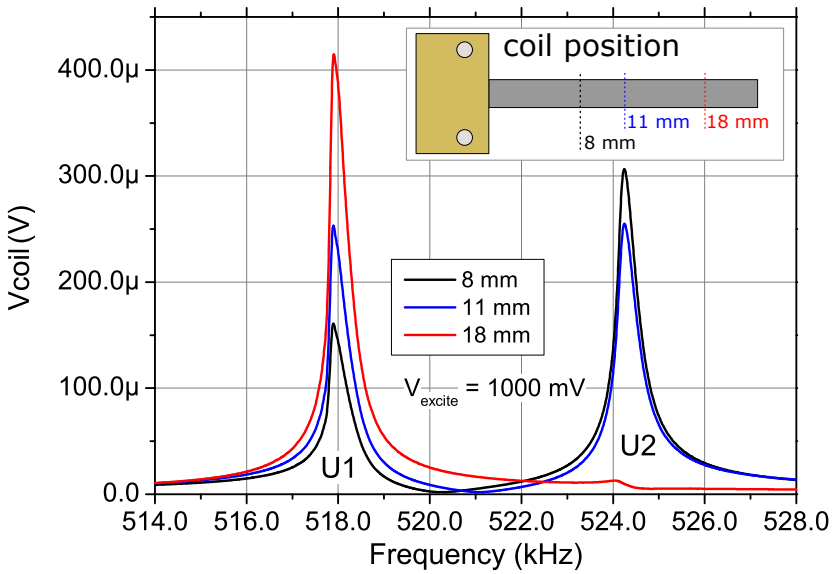

Figure 3.11: Frequency sweeps revealing U1 and U2 oscillations using a local induction coil at three characteristic positions. 8 mm, about first third, 11 mm corresponding to the center and close to its free end at 18 mm. The induced coil voltage varies depending on the position of the coil and the prevalent oscillation mode.

17 mm or two individual pickup coils in order to compensate for the antiphase signal which is generated. Likewise, U3 and higher modes would require two pairs of pickup coils for 0 ° and 180 ° oscillations. These may either be passively connected as to not cancel the individual signals and subsequently amplified using a single amplifier or separately amplified and summed in a second stage. However, it is likely that a large amount of separate windings will deteriorate the signal, because the magnetic flux in a high permeability material is not sharply localised.

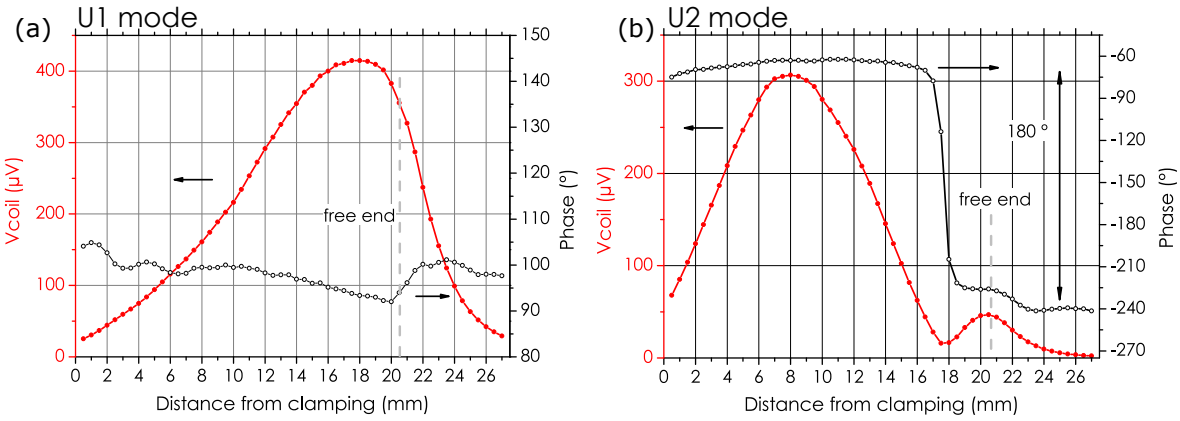

Figure 3.12: Local induction coil amplitude and phase of U1 and U2 oscillations along the long cantilever axis. The piezoelectric excitation amplitude is 1000 mV. (a) U1 mode induction amplitude monotonically increases until reaching a maximum of 410 µV around 18 mm. The induced voltage amplitude decays rapidly in free space past the cantilever tip at 20.5 mm. (b) U2 mode induced voltage reaches a absolute maximum from 7 ... 9 mm exceeding 300 µV. At about 17.5 mm the induced voltage reaches a minimum associated with a phase jump which reverses the polarity of the induced voltage at the tip region.

3.5 Micromagnetic Investigation

Extensive magneto-optical Kerr effect (MOKE) imaging was performed on the magnetostrictive phase of the ME composites to gain deeper comprehension of the micromagnetism and consequently about sources of magnetic noise. The MO imaging was performed in close collaboration with the Nanoscale Magnetic Materials Group of Prof. Dr.-Ing. Jeffrey McCord. The presented images and results are obtained from an amorphous, magnetically annealed single layer FeCoSiB, details of which are found in [Hay+18] and [Hay+19]. MOKE imaging was performed in two different modes of operation, (a) statically and (b) time-resolved (TRMOKE). In both operation modes the piezoelectric phase was electrically excited to match one of the mechanical resonances of interest. The details of static mode are earlier explained in section 2.

An alternating magnetic field decaying over several periods is directed along the y axis in order to reach a technically demagnetised state only governed by the present uniaxial anisotropy, which main contribution is given by the thermally induced anisotropy K_u, which lies along the short axis of the cantilever. The direction of MO sensitivity lies along the same axis, thus the dark/light contrast is derived only towards this axis. Uniform, alternating stripe domains form in the central region of the film, in order to reduce the contribution to magnetostatic energy. Figure 3.13a shows the situation after such a decay, the magnetic domains alternately lie along the anisotropy axis. A closeup from the region indicated by the dashed box is shown in figure 3.14, the average domain

width is about 50 µm which is commonly found in annealed amorphous films [Urs+20]. If U1 mode resonance is excited with an amplitude of 600 mV, as in figure 3.13b, already a strong contrast blurring at the free end appears. This blurring indicates strong magnetisation changes which are not in sync with the shutter, thus averaging its contrast to grey. Between the strongly blurred and the contrast rich region, a transition region forms, where very large, temporally stable domains appear. The domains in the transition region are large, on the order of 500 µm, giving evidence for the absence of anisotropies, or at least locally, strongly reduced effective anisotropy. On the left of the transition region there is no evidence for changes in the magnetic domain state, whereas the resolution towards microscopic phenomena is limited using this overview observation method. If the excitation voltage is further increased to 1400 mV, this transition region is shifted towards the center as presented in figure 3.13c. A fine stripe contrast seems reappearing in the center of the region with strong remagnetisation highlighted by the dashed square at about 3/4 of the length.

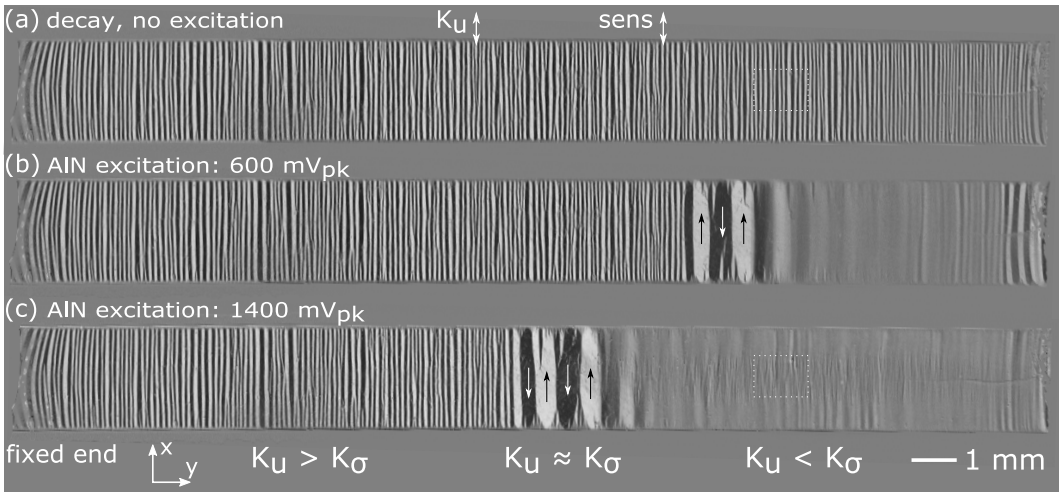

Figure 3.13: MOKE overview showing a complete domain view on the magnetoelastic phase and the effect of piezoelectric excitation in U1 mode on the magnetisation. The MO sensitivity lies parallel to the anisotropy, as indicated. (a) after magnetisation decay domains follow the uniaxial anisotropy K_u alternately in stripe fashion. (b) A piezoelectric excitation voltage of 600 mV leads to three principal regimes appearing. The oscillation causes a time variant stress induced anisotropy K_σ competing with K_u. (c) Upon further increase of the excitation voltage, these principal regimes are pushed further towards the clamping. Indicated in the far region, a fine stripe contrast reappears in the central third of the cantilever width.

Analogous to the treatment of U1 mode oscillation, in-operando MOKE studies were performed using the same sample excited in its U2 mode resonance, this is depicted in figure 3.15. Figure 3.15a is again the decayed state shown as reference, figure 3.15b shows the domain scape for a piezoelectric excitation of 1750 mV. As already indicated by displacement line scans in figure 3.5 on page 60 and local induction coil studies

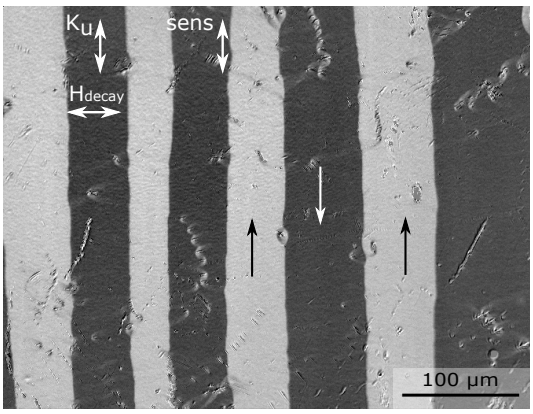

Figure 3.14: MOKE microscopy image after magnetic decay transverse to anisotropy direction, showing characteristic stripe domain pattern of annealed amorphous FeCoSiB. Image taken from representative central region.

figure 3.12 on page 66 a significant amount of stress is present in the first third of the cantilever near the fixed end. This stress acting on the magnetisation leads to strong blurring near the fixed end, as well towards the tip end, in line with findings concerning local induction measurements discussed in section 3.4. A transition region is again present exhibiting wide, stable domains up to 500 µm width. Note that higher excitation is needed for comparable effect magnitude in U2 mode than is neccessary for U1 mode, this compares well with data on displacement as well as local induction magnitudes. U1 mode seems to be more efficiently excited than U2 mode. Other members of the U mode family were not found by sweeping excitation frequency while performing static MOKE as shown, even under strong excitation conditions. Efficient excitation of higher U modes may not be possible using the given plate capacitor geometry.

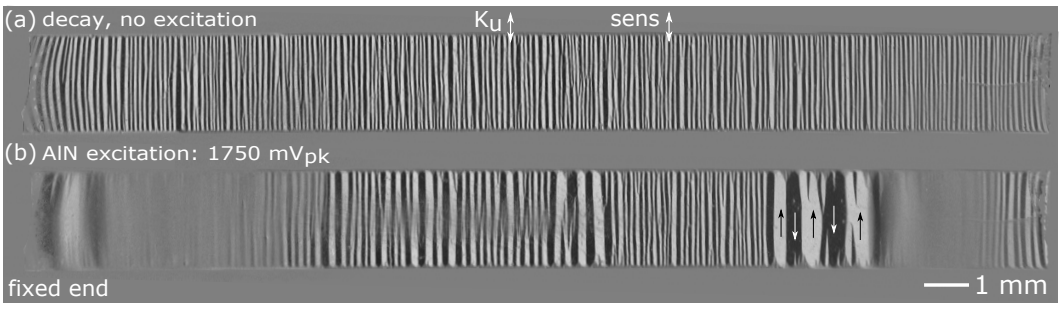

Figure 3.15: MOKE overview showing the magnetoelastic effect of piezoelectric excitation in U2 mode on the magnetisation. (a) reference image after magnetic decay (b) U2 excitation with 1750 mV excitation amplitude. Strong magnetoelastic activity is observed near the clamping and towards the tip.

3.6 Magnetoelastic Modulation

For the purpose of illustration this section will deal with magnetoelastic modulation using exclusively homogeneous in-phase stress, this best resembles U1 mode oscillation near the cantilever's free end. For U2 resonance mode (or even higher order U modes) which are mechanically more complex involving mechanical nodes and associated regions of opposing phase and thus require a more elaborate treatment, the underlying assumptions stay valid. Schematically figure 3.16 depicts a film of positively magnetostrictive material and its domains of uniform magnetisation M having a slightly misaligned uniaxial anisotropy K_u under periodic mechanical stress σ. (a) For no externally present magnetic field $H_{ext} = 0$ the magnetisation will tilt under maximum tensile stress and be stabilised towards its initial orientation for maximum compressive stress. The overall magnetisation in the direction of the coil axis will cancel out because of alternating tilting with opposing direction, ideally leading to zero induced voltage. If H_{ext} has a non-zero value along the coil axis, as in (b), the symmetry is broken and the magnetisation periodically follows the direction governed by even a small external field. The overall magnetisation will thus point along one direction on the coil axis, leading to finite voltage being induced. At maximum compressive stress the situation qualitatively resembles the one for compressive stress of (a).

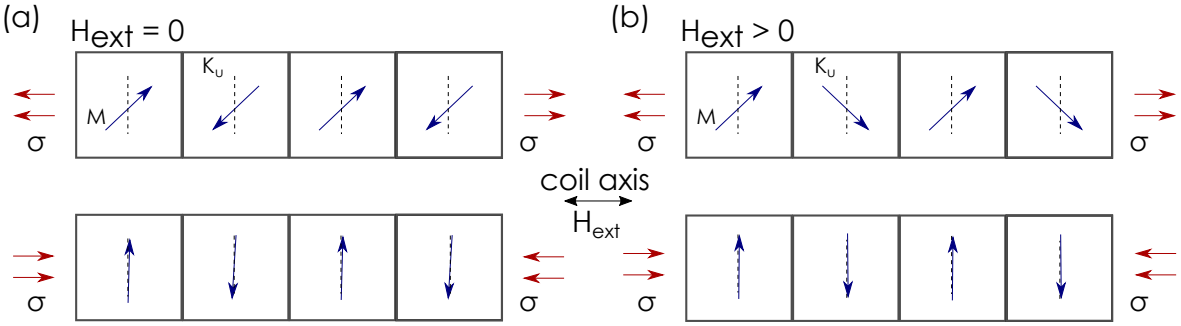

Figure 3.16: Qualitative picture of periodic stress σ acting on magnetic domains of magnetisation M in a positive magnetostrictive material. An induced uniaxial anisotropy K_u at slightly misaligned right angle towards the axis of external magnetic field H_{ext} is present. (a) Oscillation extremes for the case of no external field $H_{ext} = 0$. M tilts in interleaved fashion upon tensile stress, reducing total energy by closing stray fields. The cumulative magnetisation along the coil axis ideally amounts to zero. (b) A finite H_{ext} applied leads to a preferred tilting of M resulting in non-zero magnetisation within the coil. Based on [Liv82].

3.6.1 Simple Picture

In this section a simple model using micromagnetic equations and some assumptions will lead to a clearer understanding of the induced coil voltage. The model is simple

Table 3.1: Physical parameters used for magnetic modelling.

Symbol	Value	Unit	Comment
M_s	1.12 (1.4)	$^{MA}/_{m}$ (T)	Saturation magnetisation
H_k	880	$^{A}/_{m}$	Anisotropy field
K_u	620	$^{J}/_{m^3}$	Thermally induced anisotropy, uniaxial
K_{zee}	$\propto H_{ext}$	$^{J}/_{m^3}$	For FeCoSiB, at 1 Oe is 112 $^{J}/_{m^3}$, unidirectional
K_σ	$\propto \sigma$	$^{J}/_{m^3}$	Stress induced anisotropy, uniaxial
λ	30 ppm	-	Saturation magnetostriction along long axis
σ	$\propto {}^{1}/_{R}$	Pa	Piezo generated stress, from radius of curvature R

and limited to a single domain with constant susceptibility within $H_{ext} < H_k$, thus magnetostatic contributions by sample shape and associated magnetic domains are not considered, recent work considering such interactions is presented by [Ber+14]. The working hypothesis for this magnetoelastic modulation scheme is the interplay between the time invariant anisotropy K_u (equation (3.1)), the time varying stress induced anisotropy K_σ (equation (3.2)) and the externally applied magnetic field H_{ext}, which is related to a proportional Zeeman energy K_{zee} (equation (3.3)).

$$K_u = \frac{\mu_0 H_k M_s}{2} \tag{3.1}$$

$$K_\sigma = \frac{3}{2}\lambda\sigma \tag{3.2}$$

$$K_{zee} = \mu_0 H_{ext} M_s \tag{3.3}$$

For the assumption that $f(K_\sigma) >> f(H_{ext})$ the mechanical osciallation frequency is much higher than any external magnetic field, H_{ext} is assumed time invariant.

Livingston [LML82] proposed a model for magnetoelastic interactions in transversely annealed amorphous ribbons, this is adapted to the present case of a substrate dominated mechanical oscillator and associated periodic stress on the attached magnetostrictive thin film. Dealing with positively magnetostrictive materials as in case of FeCoSiB, tensile stress ($\sigma\lambda > 0$) has the effect of lowering the anisotropy along the stress axis, by $-\frac{3}{2}\lambda\sigma$, the case of compressive stress ($\sigma\lambda < 0$) on the contrary leads to $+\frac{3}{2}\lambda\sigma$, an effectively increased anisotropy along the stress axis. The mechanical oscillation leads to periodic sign changes of the stress imposed on the film, two basic cases have to be considered, measurements of these are depicted in section 4 Fig. 2d.

High excitation

The first case considers high piezoelectric excitation making the piezoelectrically induced K_σ dominantly strong in magnitude. Model calculations are presented in figure 3.17 on the following page, depicting lobes of K_{eff} around the cantilever in order to illustrate the force acting on the magnetisation for several instants within one period of oscillation. Due to twofold symmetry of this simple case, there are always two equivalent positions of highest anisotropy e.g. lowest total energy, only one case is explained. In the first half cycle a situation arises where tensile stress is present, peaking at $+K_{\sigma,max} \approx 33\,\mathrm{MPa}$ directed along the existing K_u direction thus increasing total anisotropy, the marker shows a resulting magnetisation angle of 88.5 °. Note the slight inclination towards the right, caused by an externally applied magnetic field of anisotropy K_{ext}. As the time dependent anisotropy is lowered to $0.5K_{\sigma,max}$ the resulting angle is 87.6 °. At zero crossing, the anisotropy contribution by stress is zero, thus only the external field acting on the uniaxial anisotropy leads to an angle of 84.8 °. As the sign of the stress changes, the effective anisotropy is lowered until reaching a critical compressive stress value for σ of $-13.76\,\mathrm{MPa}$ where the anisotropies exactly cancel out at $-K_{\sigma,crit}$, resulting in $K_{eff} = 0\,{}^{J}/_{m^3}$. At this point the film is infinitely soft magnetic ($\mu_r = \infty$), theoretically. The associated lobe is solely determined by the external field direction, hence its maximum being at exactly 0 °. From here the problem only shows one distinct maximum. Upon increasing the compressive stress magnitude the direction of magnetisation remains unchanged at 0 °. This is shown for $-0.5K_{\sigma,max}$ and $-K_{\sigma,max}$ for the sake of completeness.

A schematic time domain view of the stress is given in figure 3.18 on page 73 relating the actual mechanical oscillation to the portion effectively acting on the magnetisation in terms of changing the magnetisation direction. About 36 % of the oscillation time is cut off as the stress exceeds the critical value, leading to longitudinal magnetisation at 0 °. The stress along the short axis of the cantilever is inversely proportional to the radius of curvature, as discussed in [Hay+19]. This results in the center region of the cantilever being far more stressed than the regions where the magnetic film ends, this is especially visible in the FEM stress contour maps shown in figure 3.6. This brings implications as the above stated model does not hold for regions where film stress relaxation occurs through formation of magnetic closure domains, as is the case for the film edge.

Furthermore, this resulting curvature along the short axis is also a function of distance towards the fixed end, as can be derived from figure 3.4 on page 59. A rather exotic experimental observation is shown in figure 3.19, where a cantilever composite was strongly excited at 9000 mV that the piezoelectric excitation lead to mechanical fracture of the entire composite, resulting in a crack along it's center line, exactly where

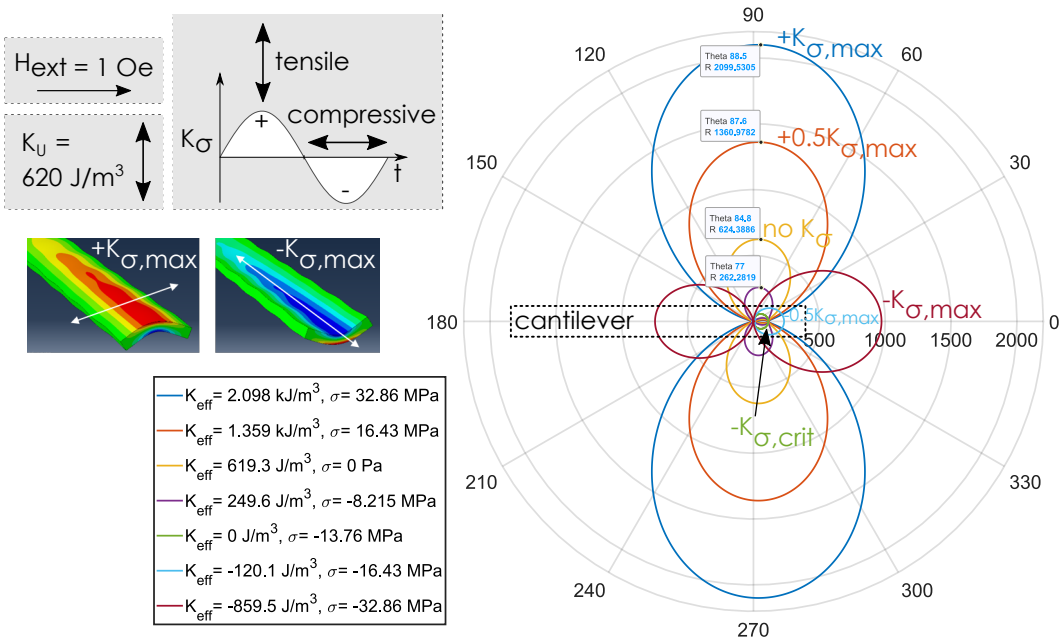

Figure 3.17: Schematic representation of the highly symmetric magnetic anisotropy landscape (K_{eff}) for the case of strong piezoelectric excitation (3500 mV) and an external field of 1 Oe. The radial axis gives the effective anisotropy for different values of K_σ occurring during one period of oscillation. The magnetisation will be forced to always point along the maxima of the anisotropy lobes. For the case of strongest tensile stress, $+K_{\sigma,max}$ adds to the already present K_u, forming the largest lobe, forcing the magnetisation to lie at an angle of 88.5 °. The slight inclination is caused by the external magnetic field pushing towards 0 °. At the zero crossing of K_σ only K_u persists, leading to a small lobe pointing to 84.8 °. Upon sign change of K_σ, the compressive stress regime is entered, thus countering K_u, leading to a situation where the effective anisotropy is diminished. At a compressive stress value of 13.76 MPa the anisotropies exactly cancel out, the required energy density is denoted $-K_{\sigma,crit}$, this lobe is essentially only defined by the external magnetic field, thus it is shifted by the associated Zeeman energy.

highest stress would be expected. Astonishingly, the aluminium nitride phase did not experience simultaneous dielectric breakdown, however its electrical capacitance lowered somewhat.

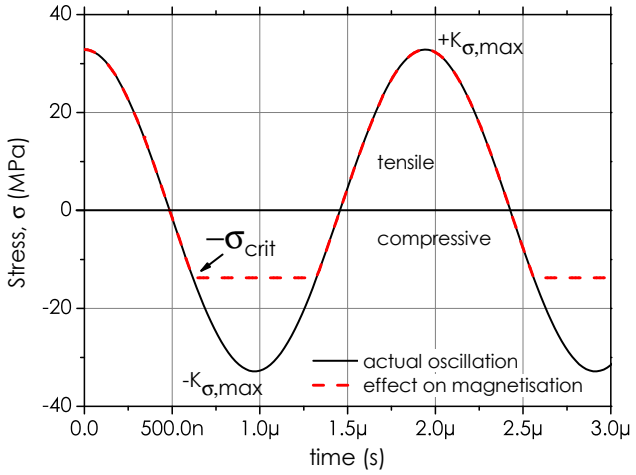

Figure 3.18: Calculated time evolution of the stress (σ) in U1 mode at the center of the cantilever using high excitation voltage. The effect of the stress induced anisotropy on the magnetisation is capped at $-K_{\sigma,crit}$, leading to practically no change in the induced coil voltage and wasting about 36 % of one oscillation.

Figure 3.20 relates the presented model to an in-operando time-resolved MOKE study, involving an external magnetic field H_{ext} of 1 Oe as well as strong piezoelectric excitation. The numbers 02 to 102 refer to selected frames captured within one period of U1 mode oscillation. Given that the MO sensitivity axis is aligned vertical, parallel to K_u one can observe strong contrast for the stress induced changes of the principal domain configuration. Frame (2) shows the situation for maximum tensile stress, see plot, contrast rich stripe domains are visible, as in this case K_u and K_σ add up and yield a high K_{eff} . The inset plot shows a strongly bimodal distribution with equal intensities, indicating well aligned uniaxial behavior. Towards (28), where the stress is nearly zero the difference to (2) is subtle, as the K_u takes over, the domains are still forced along the easy axis, a slight growth indicates lower uniaxial anisotropy. Frame (37) shows clear tilting of secondary domains under the compressive stress. This image is taken close to $-K_{\sigma,crit}$, thus secondary stripe domains are formed within the still prevalent primary domains, as indicated by small arrows. As a result, the distribution plot shows less contrast and a grey shift, because the magnetisation is no longer interleaved in strong 180 ° fashion anymore. Frame (52) shows a perfect gaussian grey tone distribution, indicating that the magnetisation at this stage is aligned along the axis of external field under maximum compressive stress $-K_{\sigma,max}$, thus yielding no contrast. In frame (78) a fine forest of domains reappears, as the dynamic K_σ is released to zero at this point. In (86) the domains rapidly grow again under the increasing tensile force, enhancing the effect of K_u. (102) finalises the stress oscillation cycle, in which a complete remagnetisation is achieved. Note that when comparing frame (28) to (78) it shows a much wider domain contrast of about 25 µm in contrast to about 10 µm wide

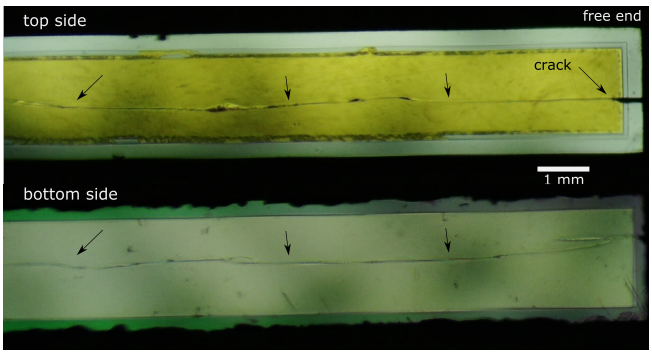

Figure 3.19: Light microscopy image of the tip region of a fractured ME composite, excited in U1 resonance at 9000 mV_{pk}. The piezoelectrically induced fracture leads to mechanical failure through the entire 350 µm thick silicon substrate, as seen by the crack propagating along the center line of the composite, top and bottom side. Dielectric breakdown of the 2 µm AlN layer did not occur. This is supplemental information taken from [Hay+19].

domains in (78). These observations give rise to asymmetry in this process of periodically competing energies, naively, superposition and time invariance of energies is assumed. The predictions of the model are not entirely fulfilled, as would be expected, in depth modelling including domain effects and time variant energy superposition is required to enhance the level of detail of the model. However, start (02) and end (102) of one oscillation show precisely the same domain configuration, as the image, resulting from a subtraction (and inverted) of (02) and (102) shows no sign of domain outlines (scratches are visible and minor speckle developed with measurement time). When performing modulation in U modes, using very large excitation (or carrier) amplitudes leads to disproportionately strong noise increase as shown and discussed in [Hay+19]. Thus from experimental observations, it is necessary to optimize the increase in magnetic sensitivity with a simultaneous decrease in noise in order to define a working point in terms of magnetic signal-to-noise ratio.

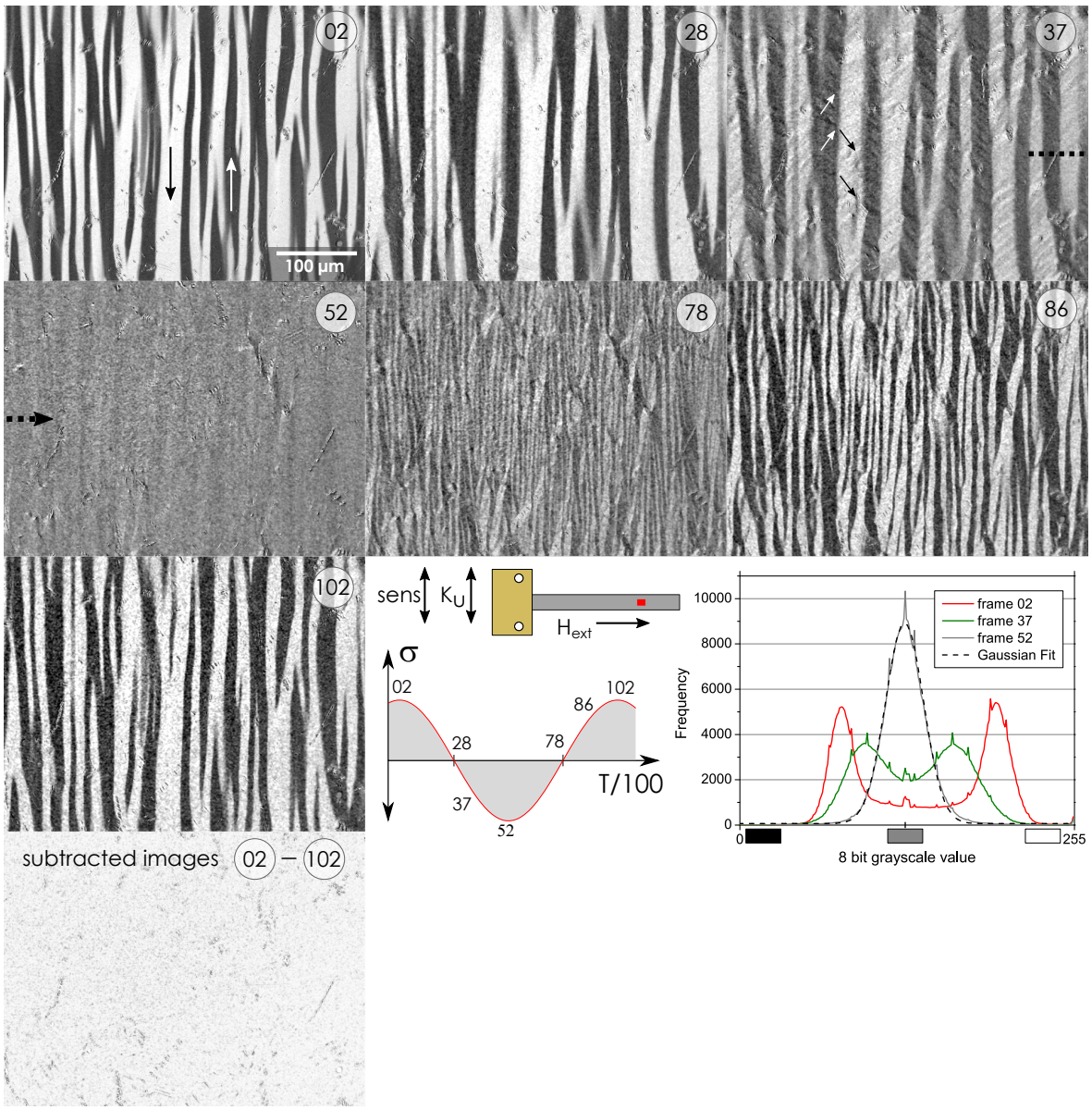

Figure 3.20: Time resolved MOKE images taken in-operando within one period of U1 mode oscillation, excited at 1400 mV_{pk}. One oscillation period is split into 100 frames, which are each averaged 160 times in order to yield enhanced contrast. An external field H_{ext} of 1 Oe is present. Between (2) and (28) lowering of tensile stress along the sensitivity direction leads to a subtle widening of the domains. Upon reaching (37) a strong tilt away from the sensitive axis leads to contrast degradation, the principal domain walls persist, however a fine buckling domain pattern is created. At (52) strong compressive stress leads to magnetisation pointing horizontal (following H_{ext}), as a consequence contrast is completely lost. As stress magnitude is lowered again, (78) a very fine forest of domain with less than 10 µm width begins to reappear. Under the effect of growing tensile stress domain wall density is lowered again in (86). A subtraction of frame (02) from (102) shows no geometric domain features (apart from some increased image noise due to thermal drift). This proves that the initial domain configuration is recovered throughout a complete oscillation cycle. The imaged region is indicated by the red square in the inset schematic, using a 20x objective. The histogram plot shows how the strong bimodal contrast distribution of (2) is pushed towards a value of 127 or 50 % gray through (37) yielding a near perfect Gaussian distribution centered at 127 in (52).

Low excitation

In the following the case for low, more realistic excitation and a smaller external field is discussed and compared, as above with time resolved MOKE imaging performed under the same conditions. Figure 3.21 shows the anisotropy landscape for the case of about 500 mV piezoelectric excitation and an external field of 500 mOe. In this case the stress induced anisotropy K_σ is again time dependent, K_{zee} resulting from the external field and the induced anisotropy K_u are time invariant. For sufficiently small values of excitation, the stress is unable to reach a value in which it overcomes K_σ thus overcompensating the existing easy axis. In the case of maximum tensile stress, again the induced anisotropy K_u is strengthened, resulting in a K_{eff} of nearly $950\,{}^{J}/_{m^3}$, resulting in a magnetisation tilt of about 88.3 °. When K_σ is lowered to half its maximum value, the magnetisation is tilted another 0.4 ° towards the long axis of the cantilever. Even upon reaching the opposite extreme case of maximum compressive stress at $-\sigma, max$ of about −7.2 MPa, the K_{eff} stays positive, because the critical stress $-\sigma, crit$ is not reached. In this case the magnetisation finds its energetic minimum at 84.5 ° under the force of the external field, which now has largest effect on the magnetisation, because the effective anisotropy K_{eff} is lowest, only about half of the value of the induced anisotropy.

An associated time resolved MOKE study is presented in figure 3.23 on page 79, in this case the direction of magneto-optical sensitivity is set to lie parallel to the long cantilever axis and also H_{ext}. The large horizontal stripes 80 ... 100 µm of low MO contrast indicate the primary domains, in between which bloch domain walls show an alternating bright white and black contrast. The images are selectively taken in order to represent the extreme points of one oscillation period. (23) Is close to $-\sigma_{max}$, thus maximum compressive stress is acting this stress is far below $-\sigma_{crit}$, hence slanted secondary domains form within the primary domains. This way the magnetisation is altered without perturbation of the primary domain pattern, similar to figure 3.20(37). (70) Shows the effect of the maximum tensile stress σ_{max}, the primary domain pattern remains, the contrast of slanted secondary domains vanishes. (118) Shows the end of one full oscillation cycle relative to (23), an image calculated by substracting both and inverting leads to only noise remaining. A skip or position change of the primary domain walls would be highly visible in the difference image.

An estimate of the required power is made by means of an impedance spectrum showing U1 and U2 mode, in figure 3.22 on page 78. Roughly assuming about 300 Ω for U1 mode, at 500 mV excitation voltage allows a power estimation by $P = \frac{U^2}{R} = \frac{250\,\mathrm{mV}^2}{300\,\Omega}$ leading to a power consumption of less than ≈ 200 µW for its electrical modulation.

These two presented scenarios demonstrate that the magnetisation in the ME composite can be modulated using only piezoelectrically induced stress, anywhere from

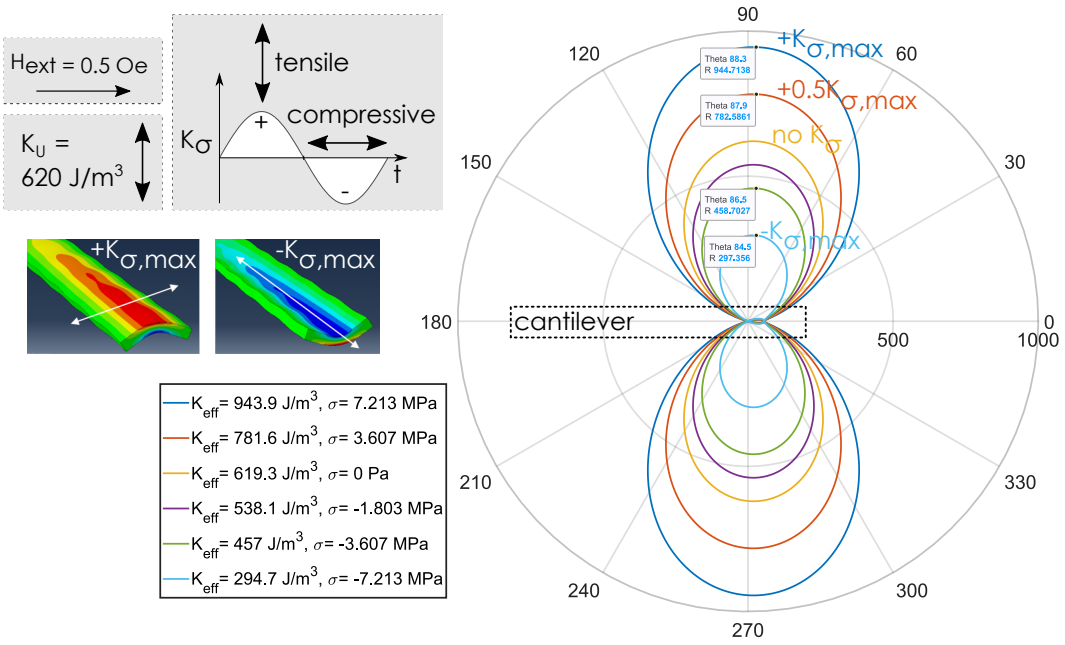

Figure 3.21: Schematic representation of the highly symmetric magnetic anisotropy landscape (K_{eff}) for the case of low piezoelectric excitation (350 mV) and an external field of 500 mOe. The radial axis gives the effective anisotropy for different values of K_σ occurring during one period of oscillation. The magnetisation will be forced to always point along the maxima of the anisotropy lobes. Unlike the case presented in figure 3.17, the stress induced anisotropy K_σ has a magnitude of $324\,{}^{J}/_{m^3}$ which is roughly half the magnitude of the uniaxial anisotropy K_u with $620\,{}^{J}/_{m^3}$, thus it never being able to dominate the direction of the magnetisation. A continuous modulation of the effective anisotropy K_{eff} takes place.

moderately to dominantly, even causing the entire composite to fracture. When comparing the predictions and MOKE experiments with the conditions actually present when the composite is in use as a sensor employing the converse ME effect, the case for low excitation gives the best signal-to-noise ratio. When reviewing the high excitation case (figure 3.20(37) and (52)), deep modulation of the micromagnetic energy landscape leads to loss of favourably occupied domain pinning centers and thus strong primary domain wall mobilisation, known to induce random voltage spikes in the pickup coil surrounding the composite. In the case of low excitation the primary domain configuration remains throughout a cycle, however modulation of the K_{eff} [3] leads to somewhat tilting of magnetisation by gradual secondary domain effects caused by the externally applied unidirectional forces i.e. H_{ext}. In this case the magnetisation vectors are slightly tipped by the external field, but without avalanching large intrinsic noise sources. Using the simple model, this avalanche can be expected at an external stress of approximately 13.8 MPa or an excitation of about 750 mV, which is on the order of the experimentally observed value of about 220 mV [Hay+19]. Of course this

[3] And thus of course also H_a, the anisotropy field.

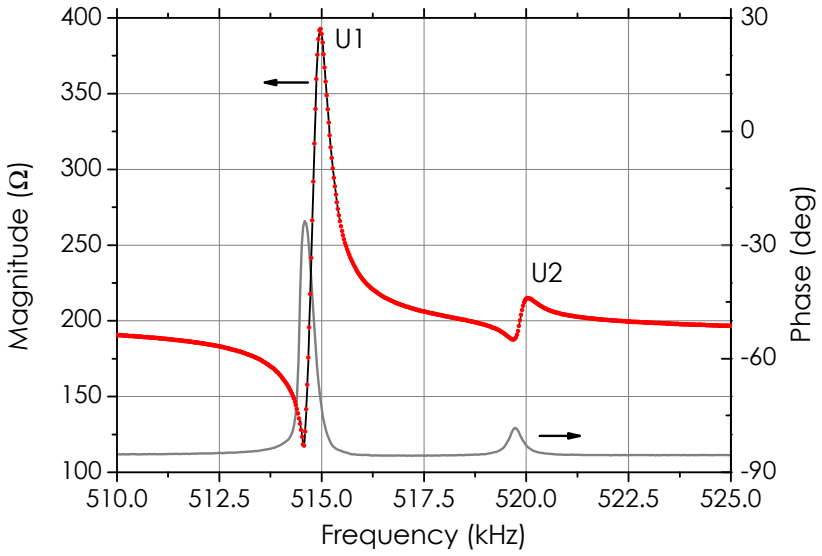

Figure 3.22: Typical impedance spectrum taken directly from the piezoelectric phase, showing U1 and U2 mode at an excitation amplitude of 500 mV. Depending on the exact frequency, a resistance of about 300 Ω results for U1 mode, about 200 Ω for U2 mode.

is just a very crude estimation, as any additionally present stress stemming from deposition, mounting and handling of the composite can lead to deviations from this value. Equally external magnetic fields at arbitrary angles, even on the magnitude of a few µT can alter this value.

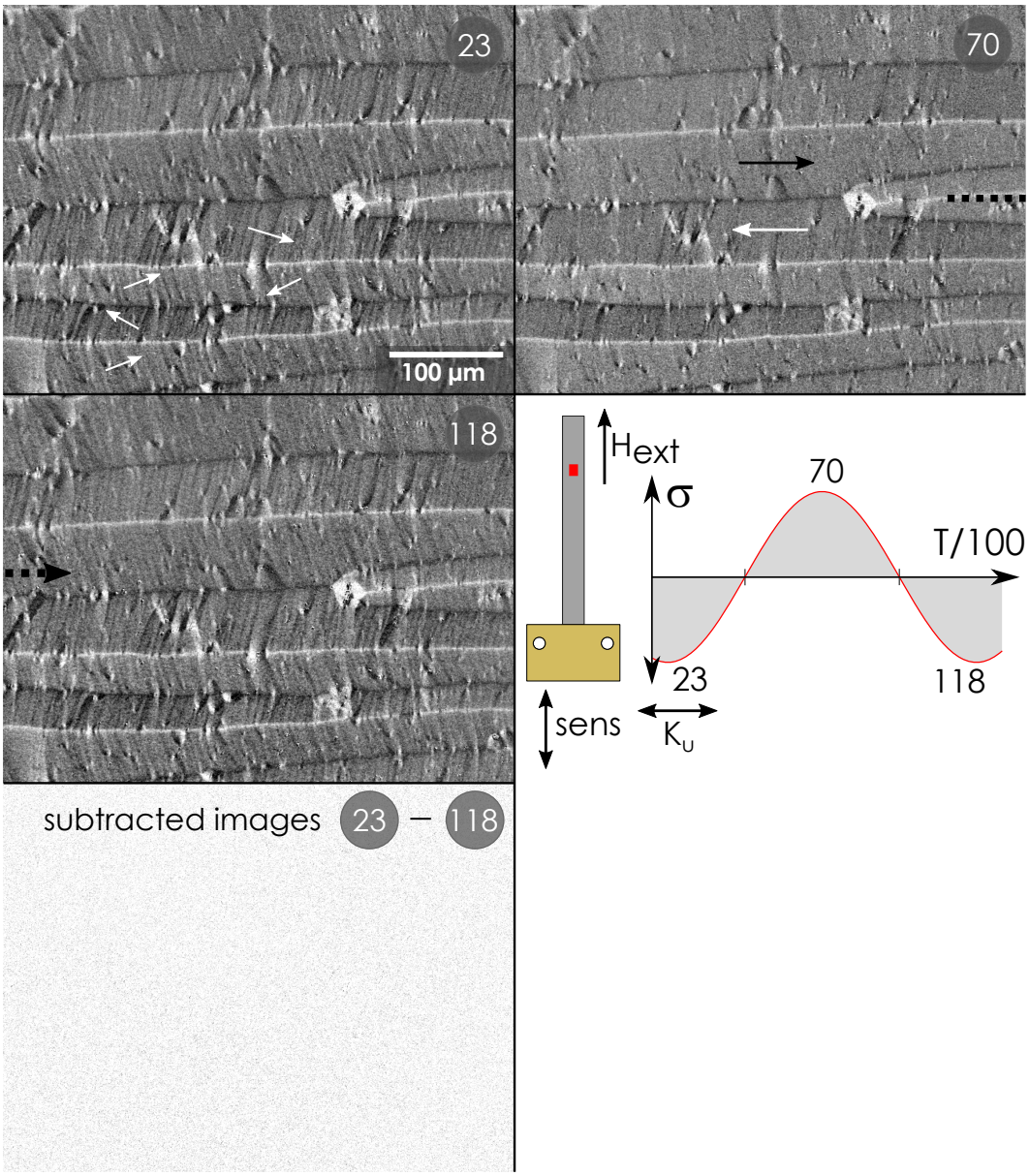

Figure 3.23: Time resolved MOKE imaging showing magnetisation evolution though one U1 mode oscillation period, in this case the sensitivity is aligned vertically, perpendicular to K_u. The external field H_{ext} of 500 mOe is aligned vertically. (23) Tilting of small domains within the rather large, horizontal, primary domains can be observed, as maximum compressive stress is reached. (70) shows the effect of maximum tensile stress along the horizontal axis, the primary domain walls do not move under this oscillation. (118) showing again maximum comprssive stress acting on the magnetisation. A subtraction of two extreme images from one period (23) and (118) shows no difference in the obtained domain pattern. One oscillation period is split into 95 frames, which are each averaged 160 times in order to yield enhanced contrast. The red rectangle in the cantilever sketch indicates the position of the MOKE images.

3.6.2 Induced Voltage

Figure 3.24(inset) graphically illustrates the situation involving a static magnetic field H_{ext} in which a coil is periodically waving by a small angle $d\phi$. This physically has the same effect as waving a fixed magnetisation vector within a coil by $d\phi$ in a time dt, basically necessary for induction is consequently $U_{ind} \propto \frac{d\phi}{dt}$.

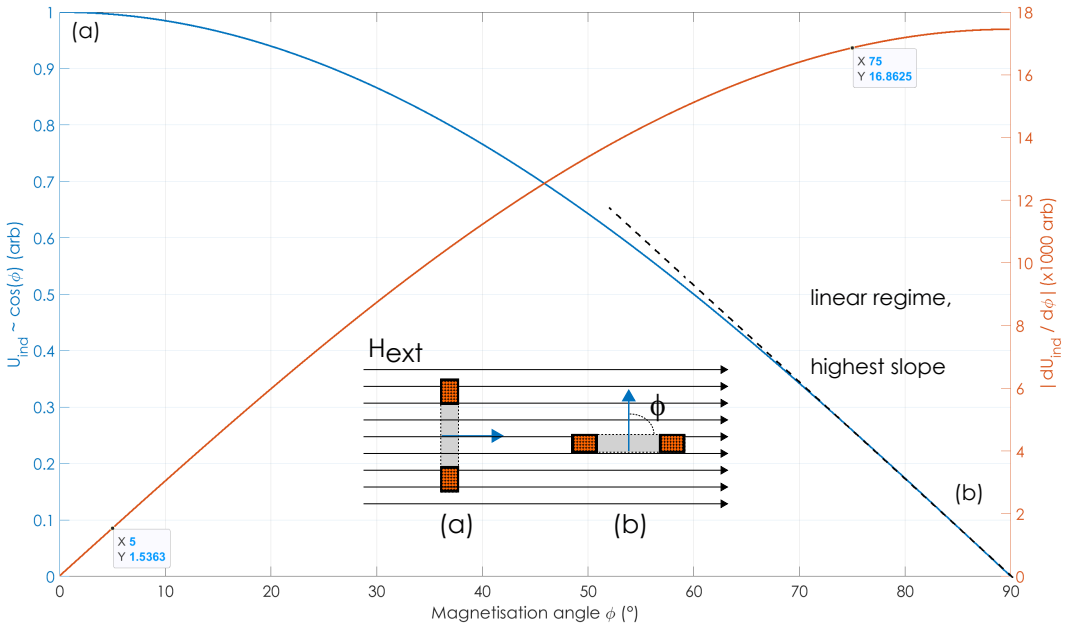

Figure 3.24: Voltage induced in a coil for two extreme orientations of the external magnetic field H_{ext} towards axis of the coil (ϕ, blue arrow), as well as its derivative, sine function (red trace). Region (a) maximum number of field lines are picked up by the coil, induced voltage is highest. Small misorientations lead to little effect on the induced voltage. Point (b) induced voltage is ideally zero, even smallest changes in orientation lead to strong induced voltage. A voltage is only induced if either ϕ is jittering within a time dt or H_{ext} is varying within time dt.

Following

$$\Phi = \vec{B}\vec{A} = BAcos(\phi) \tag{3.4}$$

Φ is the magnetic flux resulting from magnetic field B acting through the cross-section area of the magnetic film A, guiding essentially all flux lines. The graph indicates an essential fact concerning the application of the composite resonator as a sensor, it requires a high change of induced voltage U_{ind} by an external field rather than only a high induced voltage caused by the magnetisation oscillation itself. So the point of highest induction is clearly given by point (a) as $cos(\phi) \approx 1$, this corresponds to the magnetisation lying along the long cantilever axis, as discussed in section 3.6.1. However, the external magnetic field has the effect of altering the magnetisation angle by a small additional $d\Phi$, the slope in the vicinity of (a) is minimum, figure 3.24, red

trace. Region (b) on the contrary leads to lowest induced voltage, but altering the magnetisation angle (coil angle as in the example) even faintly, $cos(\Phi) \gg 0$, the slope of the induced voltage is a factor of 12 larger. Additionally, region (b) offers high linearity of $U_{ind}(\Phi)$, as indicated by the dashed line.

Using equation (3.5) and the angle change $d\phi$ obtained from simplified simulations within one U1 oscillation period $dt \approx {}^{1}/_{500\,\mathrm{kHz}} \approx 2\,\mu\mathrm{s}$ one can vaguely estimate the order of magnitude of the induced voltage U_{ind}. The associated $K_{\sigma,max}$ is $165, {}^{J}/_{m^3}$. The resulting difference in magnetisation angle evoked by $K_\sigma(t)$, within the boundaries of $\phi(K_{\sigma,max}) - \phi(K_{-\sigma,max})$ results in a periodic magnetisation tilting of $\approx 3/100\,°$. For this purpose a simulation using a static magnetic field of $1\,\mu\mathrm{T}$ and an excitation of $100\,\mathrm{mV}$ was performed, assuming an initial magnetisation angle of $\phi = 90\,°$, as shown in figure 3.24 on the preceding page, case (b). The change of induced voltage with respect to the magnetisation angle near case (b) is constant within $75 \ldots 90\,°$, as indicated by the dashed line, thus only the differential plays a role.

The self-resonance of the coil has a quality factor of about $Q \approx 160$, the number of its windings $N \approx 750$ [Hay+19]. B is the saturation polarisation of the thin film, a value of $1.4\,\mathrm{T}$ or $1.1\,{}^{\mathrm{MA}}/_{\mathrm{m}}$ is usually obtained. A is the cross-section of the magnetic material $4 \times 10^{-9}\,\mathrm{m}^2$, because (i) The relative permeability of the air surrounding the composite within the coil is constant in any case; (ii) The amorphous magnetic material has a very large μ_r compared to air, so that even taking the much greater cross-section of the coil into account, the strong flux conductivity of the magnetostrictive film cross-section dominates the flow through the coil.

$$U_{ind} = NAQB\frac{d\cos(\phi)}{dt} \approx 170\,\mathrm{mV}_{pk} \approx 120\,\mathrm{mV}_{rms} \tag{3.5}$$

Although this estimation is very crude the order of the resultant voltage magnitude resembles the experimental value of $40\,\mathrm{mV}$ shown in figure 3.25a (anhysterestic curve) reasonably, given the fact that the voltage is calculated for one point of quite high K_σ, resulting in threefold overestimation of the experimental value obtained. The result is especially insensitive to the unknown initial angle of magnetisation, of $90\,°$, assuming the same tilt around an initial angle of $80\,°$ yields a difference in induced voltage of only $1.3\,\%$, because the slope of the cosine is nearly constant.

As presented in the simulations, the energy landscape is highly symmetrical with respect to the externally applied field, this is resembled by the measurement shown in figure 3.25a, indicating high linearity of the induced voltage towards the field around zero field, irrespective of saturation direction. At $\pm 5\,\mu\mathrm{T}$ the induced voltage nearly reaches zero, this happens when the magnetisation is forced to $\phi = \pm 90\,°$ by the external field. Without hysteresis, this would occur at exactly zero field as shown by

the calculated anhysteretic trace. The overt hysteresis caused by the domains in the experiment leads to a lagging of the magnetisation with respect to the applied field, its magnitude given by the dynamic coercivity[4], which is 5 µT in the shown case. As expected, upon flipping of the magnetisation vector at $\phi = \pm 90\,^\circ$ within the coil, the sign of the induced voltage is reversed for angles larger than 90 ° (figure 3.24) or smaller than 270 °, thus the phase of the induced voltage magnitude jumps, figure 3.25b.

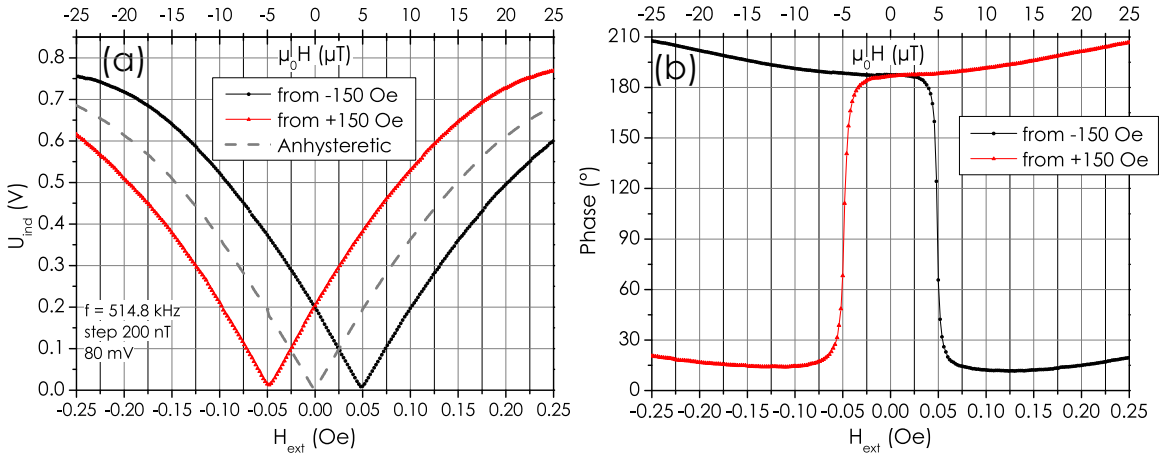

Figure 3.25: Coil induced voltage in U1 mode resonance for an excitation amplitude of 80 mV as function of external magnetic field H_{ext} coming from respective saturation. (a) Large linear regime in the vicinity of zero showing a sensitivity of about 40 kV/T. Hysteresis leads to a dynamic coercivity at ±5 µT, where the induced voltage reaches nearly zero. Calculated anhysteretic response is given as mean value, shown by the dashed line. Taken from section 4. (b) Phase of the induced voltage. Clearly, a phase reversal by 180 ° occurs at coercivity. The phase sensitivty is about 200 M°/T sharply around 5 µT and about 700 k°/T around zero field, two orders of magnitude lower.

[4]This value depends on the excitation conditions as well as the mechanical mode.

Chapter 4

Publication: Converse Magnetoelectric Composite Resonator for Sensing Small Magnetic Fields

In this article the U1 mode resonance is employed and its performance towards AC as well DC fields at no additional bias field is assessed. Linearly increasing sensitivity is limited by a disproportionate rise in near carrier noise at high excitation voltages, leading to an optimum operation range of piezoelectric excitation. Furthermore, tuning of the pickup coil to match the mechanical U1 resonance in order achieve very large sensitivities on the order of $60\,^{\mathrm{kV}}/_{\mathrm{T}}$ is successfully introduced.

Own contributions to the following article[1]

- ▷ measurement scripts and measurements (large fraction)
- ▷ numerical simulations (large fraction)
- ▷ fabrication and tuning of the composite resonator (large fraction)
- ▷ interpretation of results (large fraction)
- ▷ writing of the manuscript (large fraction)

As also stated below next publication under 'author contributions'.

Material from: *P. Hayes et. al., Converse Magnetoelectric Composite Resonator for Sensing Small Magnetic Fields, Scientific reports. 9, 16355 (2019), doi:10.1038/s41598-019-52657-w.*

[1] this information is required by regulations

www.nature.com/scientificreports

SCIENTIFIC REPORTS
nature research

OPEN

Converse Magnetoelectric Composite Resonator for Sensing Small Magnetic Fields

P. Hayes[1], M. Jovičević Klug[1], S. Toxværd[2], P. Durdaut[2], V. Schell[1], A. Teplyuk[2], D. Burdin[3], A. Winkler[4], R. Weser[4], Y. Fetisov[3], M. Höft[2], R. Knöchel[2], J. McCord[1] & E. Quandt[1*]

Magnetoelectric (ME) thin film composites consisting of sputtered piezoelectric (PE) and magnetostrictive (MS) layers enable for measurements of magnetic fields passively, i.e. an AC magnetic field directly generates an ME voltage by mechanical coupling of the MS deformation to the PE phase. In order to achieve high field sensitivities a magnetic bias field is necessary to operate at the maximum piezomagnetic coefficient of the MS phase, harnessing mechanical resonances further enhances this direct ME effect size. Despite being able to detect very small AC field amplitudes, exploiting mechanical resonances directly, implies a limitation to available signal bandwidth along with the inherent inability to detect DC or very low frequency magnetic fields. The presented work demonstrates converse ME modulation of thin film Si cantilever composites of mesoscopic dimensions (25 mm × 2.45 mm × 0.35 mm), employing piezoelectric AlN and magnetostrictive FeCoSiB films of 2 µm thickness each. A high frequency mechanical resonance at about 515 kHz leads to strong induced voltages in a surrounding pickup coil with matched self-resonance, leading to field sensitivities up to 64 kV/T. A DC limit of detection of 210 pT/Hz$^{1/2}$ as well as about 70 pT/Hz$^{1/2}$ at 10 Hz, without the need for a magnetic bias field, pave the way towards biomagnetic applications.

Magnetic field sensors are employed in a variety of industrial and electronic device applications, apart from widespread applications like linear position determination or shaft rotation speed sensing (applications where Hall effect and AMR sensors are suited for) there are applications where the magnetic field itself needs to be determined precisely. This holds true for geomagnetic sensing[1] for mineralogical and navigational purposes[2], magnetic anomaly detection (MAD)[3] and remote sensing applications[4]. An emerging field, requiring much higher spatial resolution and compact sensor dimensions, is the contactless imaging or monitoring of biological entities using the magnetic field component of bioelectric currents[5]. This biomagnetic field was unveiled by early studies, proving the concept using giant pickup-coils[6] later by sensitive yet very complex to operate SQUID magnetometers[7]. Finally, Wikswo[8] coined the term "Nondestructive testing of humans" more than two decades ago.

The signals emitted from humans in form of magnetic stray fields are of very low amplitude, cardiac signals show amplitudes on the order of 10…100 pT, whereas brain signals are typically one to two orders of magnitude lower[8]. The permanent field of the earth is about six orders of magnitude higher, thus imposing a requirement towards dynamic range. The frequencies of interest range from DC to below 1 kHz[5,8], which is typically the ELF (extremely low frequency) to VLF (very low frequency) frequency regime.

Many available low-cost, high volume sensor technologies (e.g. Magnetoresistive (xMR) or Hall effect sensors) incrementally improve in performance yet to reach the threshold of being a viable candidate for widespread convenient biomedical sensing operation. Optically pumped magnetometers (OPM) as well as fluxgate magnetometers are promising candidates for the detection of biomagnetic signals. However, despite their room temperature operation and DC field capability they unfortunately exhibit bandwidth and scalability limitations[9], respectively. In magnetoencephalography (MEG) applications the use of multichannel arrays is anticipated in order to extract useful information[8,10], thus imposing stringent spatial constraints on any proposed sensor system. xMR[11] are very promising as they can readily be produced in volume, but yet suffer from excessive 1/f-noise levels[12]. Using flux concentration measures in order to enhance magnetometer sensitivity has proven quite effective[13,14] but inherently brings a delicate trade-off between sensitivity and spatial resolution.

[1]Institute for Materials Science, Kiel University, Kiel, 24143, Germany. [2]Institute of Electrical and Information Engineering, Kiel University, Kiel, 24143, Germany. [3]MIREA - Russian Technological University, Moscow, 119454, Russia. [4]IFW Dresden, SAWLab Saxony, Dresden, 01171, Germany. *email: eq@tf.uni-kiel.de

Continuing efforts of bringing magnetoelectric (ME) devices towards applications[15,16], especially as sensing elements for most demanding weak fields[17] in biomagnetic signals are being made[18,19]. By exploiting mechanical resonance enhancement of the direct magnetoelectric effect, the sensitivity can be vastly enhanced for magnetic fields coinciding to the mechanical resonance[20,21], at the expense of the sensor's bandwidth. This straightforward approach is completely passive, thus scoring by simplicity, however, low frequency fields are intrinsically tedious to detect. By actively modulating the composite magnetically[22,23], electrically[24] or utilizing the delta-E effect[25] one can up-convert off-resonance signals and thus benefit from resonances and be sensitive in the low frequency regime of interest. Using high frequency surface acoustic wave (SAW) sensors incorporating magnetostrictive material can similarly up convert the magnetic signal by phase modulation[26].

In this study the converse ME effect in a thin film composite is exploited, exciting a high mechanical resonance mode showing a large vibration amplitude. The signals are detected by a pickup coil which is tuned in order to match its electromagnetic resonance with the excited mechanical resonance of the composite cantilever. Vibrometry measurements give insight to the nature of the mechanical oscillation, leading to periodic magnetisation modulation. The system performance towards small amplitude, low frequency magnetic fields as well as noise behaviour is analysed.

Methods/Experimental

Thin film ME composites based on silicon are fabricated at Kiel Nanolaboratory using standard microelectromechanical systems (MEMS) cleanroom processes including magnetron sputtering and photolithography. Both active layers, aluminium nitride (AlN) and amorphous iron–cobalt–silicon–boron (FeCoSiB) with a thickness of 2 µm are deposited on adjacent sides of a 350 µm thick double side polished silicon wafer. The FeCoSiB layer is RF magnetron sputtered at 200 W from a 200 mm target (FHR Anlagenbau GmbH, Germany) with a nominal composition of $(Fe_{90}Co_{10})_{78}Si_{12}B_{10}$ at an argon pressure of $6*10^{-3}$ mbar, using a vonArdenne CS730s cluster sputtering tool. After subsequent depositions of 200 nm material, a pause of 10 minutes allows for cooling and prevents crystallization of the deposited material caused by plasma heating. To promote adhesion to the silicon and prevent ambient oxidation of the alloy, it is sandwiched between thin $<$10 nm sputtered tantalum layers. The highly textured PE AlN is deposited by reactive magnetron sputtering with nitrogen using a pulse DC source, details are extensively given in[27]. A platinum layer of 80 nm below the AlN serves a dual purpose of seeding the crystal growth as well as to enable electrical contact to the bottom electrode. A top electrode consisting of sputtered chromium (10 nm) and gold (80 nm) functions as a top contact in the PE plate capacitor arrangement. Electrical access to the buried bottom electrode is ensured by partial wet chemical etching of the AlN, for this standard photolithography is used in conjunction with phosphoric acid (H_3PO_4) at 80 °C for 20 minutes. The wafers are diced into 25 mm × 2.45 mm dies, which are then heat treated at 270 °C on a hot plate in ambient atmosphere in a magnetic field of 800 Oe directed along the short axis, provided by large permanent magnets. Finally, the silicon dies are bonded to a FR4 PCB board using cyanoacrylate glue thus creating a cantilever structure. The contacts are wire bonded to the carrier PCB. The formed AlN plate capacitor holds a capacity of 1.7 nF off-resonance. Magneto-optical Kerr effect (MOKE) microscopy is performed with a large view polarization sensitive microscope and high power LED illumination, allowing magnetic domain visualization of the magnetic layer. The exact configuration and working principle is described by McCord in[28]. Mechanical characterisation was performed in unshielded environment using a vibrometry system (Polytec, Model UHF-120) and a 5x objective lens, the multicarrier signal in vibration spectroscopy was provided by a vector signal generator (Rhode & Schwarz, Model SMBV100A). The electrical characterization is carried out in a magnetically and electrically shielded environment comprising a multilayer mu-metal cylinder (Aaronia, Model ZG1), further details are given in[29]. The magnetic test field is delivered using a calibrated cylinder coil in conjunction with a low noise AC and DC current source (Keithley, Model 6221), saturation fields are provided by a bi-polar power supply (Kepco, BOP). Analysis of the sensor system, with respect to excitation and readout is performed using a high frequency lock-in amplifier (Zurich Instruments, HF2LI).

Results and Discussion

The fabricated composite is immersed into a coil, which is wound on a polymeric bobbin using 750 windings of 110 µm thick enamelled copper wire. This assembly is in close proximity to a battery powered amplifier board, Fig. 1a. The coil length spawns about 75 percent of the free standing length of the cantilever beam, as is found to be optimum using search coil magnetometers[30], excluding edge inhomogeneities and local demagnetisation effects of the magnetic core. The copper enclosed area of the coil is 32 mm^2, the core cross section is 0.005 mm^2. Using a trimmer capacitor (3…30 pF) in parallel to the coil, its resonance frequency can be tuned downwards, in order to match the excited mechanical resonance. A similar approach has been implemented in fluxgate magnetometers[31,32], essentially acting as a measure of low noise signal amplification. Figure 1b displays the equivalent circuit schematically. The ME composite forms the input port and is indicated as a radiative capacitor, its high frequency resonance is excited by the internal generator of a lock-in amplifier. The ME composite is inductively coupled to the coil, which is tuned using C_{tuner}, buffered by a low noise operational amplifier in unity gain configuration (OPA627 of Texas Instruments or LT1128 of now Analog Devices International proved well suited) in order to decouple the resonant circuit from subsequent readout electronics, i.e. the lock-in amplifier. The voltage V_{coil} is fed to the digital lock-in amplifier for synchronous demodulation. Figure 1c shows the system frequency response, denoting the mechanical resonance of interest U mode (UM) at about 515 kHz, which is constant in both traces, whereas the coils self-resonance is about 12 kHz lower in de-tuned and coinciding to UM in the tuned case, leading to increased overall gain. The air coil resonance exhibits equivalent circuit parameters of $R_{coil} = 31$ Ohm, $C_{coil} = 47$ pF and $L_{coil} = 1.16$ mH, which were determined using an Agilent 4294 A assuming a series RLC circuit, using $Q_{coil} = 1/R_{coil} * (L_{coil}/C_{coil})^{1/2}$ resulting in a coil resonance quality factor of $Q_{coil} \sim 160$. Depending on the state of the magnetic material which is introduced into the coil, the Q_{coil} will decrease. The name U mode

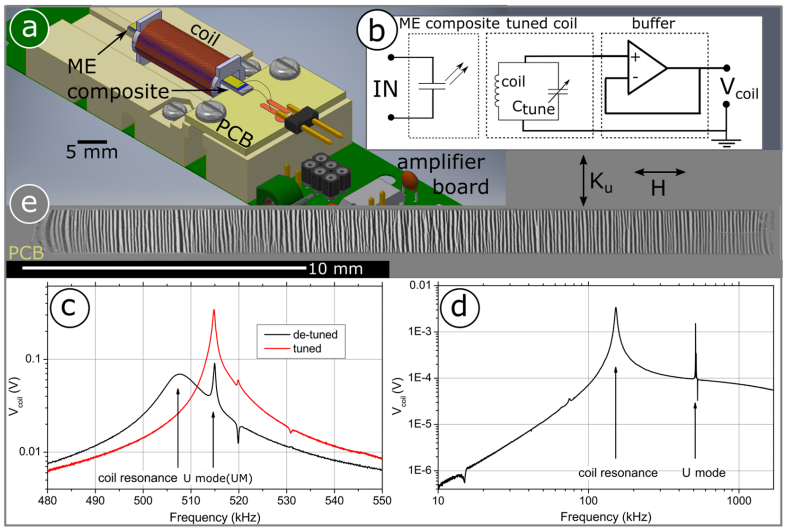

Figure 1. Sensor setup and tuning. (**a**) Schematic representation of the setup mainly consisting of a composite immersed in a pickup coil. The PE plate capacitor forms the input, the tuned pickup coil followed by an amplifier forms the output. (**b**) The circuit depicting the ME composite as a radiative capacitor structure. The signal is induced in the resonant coil, the current is buffered by a low noise unity gain buffer amplifier. (**c**) Frequency response analysis. Pickup coil self-resonance (Q~150) and mechanical resonance frequency (Q~1000), denoted UM. In the de-tuned case, and tuned in order maximize voltage output of the sensor. (**d**) Wide frequency response showing the major effect of the coil resonance and two sharp voltage peaks corresponding to mechanical resonances. (**e**) Large-view MOKE microscopy image showing the full length of the cantilevered composite after magnetic field decay. The magneto optical (MO) domain contrast of the magnetization is directed along the short axis, which is the thermally induced magnetic easy axis, denoted by K_u. *H* indicates the direction of applied magnetic fields, consequently along the magnetically hard axis. The left side is fixed to the PCB.

stems from the fact that a strong U-shaped curvature along the short cantilever axis is formed, as the reader will shortly find out. This U mode mechanical resonance is much sharper, holding a *Q* factor nearly an order of magnitude higher of Q_{UM} ~ 1000, tuning does not have to be overly accurate in order to benefit from this resonance convolution. Figure 1d gives a wider view frequency response, revealing only the broad coil self-resonance and two mechanical resonances at about 515 kHz and minor activity at 520 kHz. The resonance mode present at 520 kHz was previously studied under high driving conditions (order of Volts), obtaining a DC resolution of 1.2 nT at 200 mHz[33].

The U mode proved to be most sensitive to small magnetic fields when excited moderately. Figure 1e shows a MOKE image of the magnetoelastic FeCoSiB thin film on the cantilever, the axis of magnetooptical (MO) sensitivity being vertical. The alternating stripe contrast reveals alternating magnetisation forming due to magnetostatic energy reduction. The orientation of the magnetic domains shows a high degree of orientation along the short cantilever axis, following the thermally induced easy axis of magnetisation, denoted K_u. The observed in-plane stripe-like domains show a rather uniform width of about 60 µm throughout the length of the cantilever. Such a domain structure is typical for thin amorphous films exhibiting low total anisotropy[28] after magnetic annealing. Externally applied magnetic test fields are directed orthogonally to the sample's magnetic easy axis, denoted by *H*. In this axis a maximum of magnetoelastic coupling is achieved (Supplemental, Fig. S1). Mechanical clamping is located on the left as indicated. A distortion of the stripe pattern stemming from local magnetoelastic interaction can be seen there, as well as near the free end of the cantilever.

In order to exactly determine the shape of the mechanical U mode of oscillation and gain further insights into the high frequency (out-of-plane) electromechanical spectrum, high speed vibrometry measurements were performed. Figure 2a shows a vibrometry scan of the cantilevers FeCoSiB film surface, piezoelectrically excited at 514.8 kHz with an amplitude of 100 mV. (Supplemental, Vid. S2) The overlay grid indicates the 981 points of measurement; a colour code indicates the out-of-plane displacement relative to the plane of rest. The principal UM oscillation bends symmetrically along the short axis (*x*-axis), this gives rise to the very high resonance frequency of about 515 kHz compared to widely studied flexural modes[33,34], typically present in the audio frequency regime for mesoscopic silicon structures of millimetre dimensions. The dominant oscillation loss mechanism

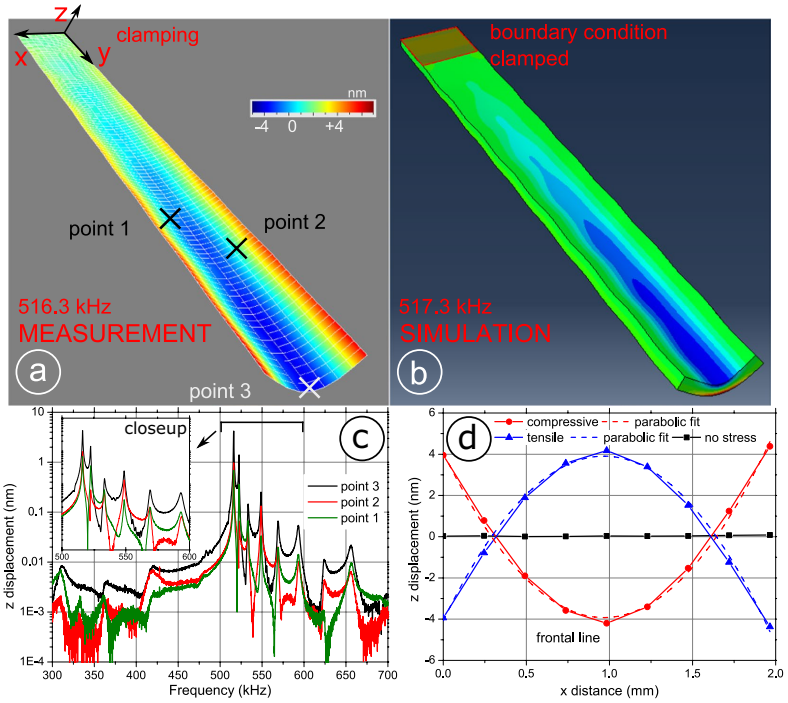

Figure 2. Mechanical oscillation mode analysis. (**a**) Vibrometry measurements of the piezoelectrically excited ME composite, indicating a bending motion along the x (short) axis at a frequency of 514.8 kHz, a high order bending oscillation is superimposed along the *y*-axis. (supplemental video online). (**b**) Qualitative FEM mode analysis simulation of a simple slab sillicon cantilever beam, clamped on one side as indicated, using the physical dimensions of the experiment. Color code gives mises stresses. (**c**) Displacement spectra of the ME composite obtained by multi carrier vibrometry reveals broadband mechanical out-of-plane activity spectra, shown for three different cantilever positions as indicated in a) Inset shows that the mechanical displacement in the U mode is by far domonating. (**d**) Displacement along the *x*-axis at the tip of the cantilever, showing the extremes of one cycle of motion, leading to alternatingly compressive and tensile stress in the magnetostricitve film.

of flexural modes in long cantilevers lies in air damping[35,36], thus seldom exceeding a *Q* of few 100 in ambient atmosphere. Due to much less displaced air molecules, this U mode shows inherently less damping, thus leading to a higher value of *Q* than that of low order flexural modes. The maximum displacement along the long *y*-axis amounts to about 25 nm, when excited by 100 mV, thus the resulting curvature contributes marginally to magnetoelastic effects. However, the deflection amplitude towards the free end reaches about 30 nm peak-to-peak displacement along the front most x-line which is about one tenth the cantilevers length, thus giving rise to a vastly increased curvature and accompanying strong magnetoelastic coupling. Note the ripple pattern along this axis, indicating a possibly simultaneously excited high order flexural mode[33]. The frequency of the U mode oscillation deviates by less than 0.7% through a set of five samples, irrespective of the rather large variance introduced by manual die mounting using adhesive glue. The high curvature along the *x*-axis leads to a very pronounced stress induced anisotropy (K_σ), uniaxially acting on the magnetostrictive material. This anisotropy is periodically changing its sign, leading to a directionality change of K_σ. For tensile stress of the film along the short axis, this results in K_σ being parallel to the thermally induced anisotropy K_u, leading to the addition of these two uniaxial anisotropies. While compressive stress leads to a configuration where K_σ lies along the *y*-axis of the cantilever, thus being orthogonal to K_u, which is quantified using Eq. (1). Where H_k, μ_0 and M_s are the anisotropy field, the permeability of vacuum and the saturation magnetisation, respectively;

$$K_u = \frac{H_k \mu_0 M_s}{2} \tag{1}$$

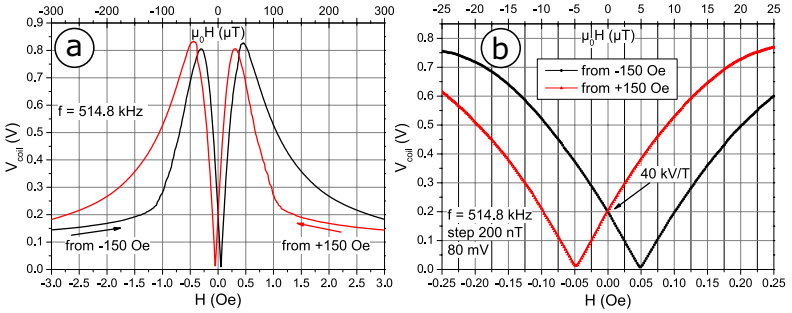

Figure 3. Coil voltage after the buffer amplifier, at the resonant frequency for a drive amplitude of 80 mV with respect to an externally applied field *H*. (**a**) Maximum induced voltage reaches above 800 mV at a field of 0.45 Oe, coming from opposite saturation. At high external fields the induced voltage drops to near zero. Towards zero field the induced amplitude decreases dramatically down to zero at the coercivity. (**b**) Close-up revealing maximum field sensitivity of 40 kV/T at zero bias field. A phase reversal ocurs at the coercive field of 5 μT.

K_u acts along the *x*-axis of the cantilever, for values of $H_k = 880$ A/m and $M_s = 1.12$ MA/m a value of 620 J/m^3 is obtained.

Figure 2d shows an *x*-axis line scan along the tip of the cantilever, for both extreme cases of oscillation as well as its resting position, along with a parabolic fit matching the shape. Using simple bending analysis after Ohring[37] Eq. (2) and the parameters gained by the parabolic fit of the measured tip curvature, an estimate of the piezoelectrically induced uniaxial stress (σ_{piezo}) can be made. For the data of an excitation level of 100 mV, a radius of curvature (R) along the *x*-axis at the free end of the cantilever of about 8.1 m is obtained, while the substrate to film thickness ratio of $t_s = 350$ μm to 2 μm, respectively, makes the film negligibly thin. Therefore following

$$\sigma_{piezo} = \pm\frac{Et_s}{2R} \tag{2}$$

where E is the Young's modulus of 169 GPa, of the Silicon substrate[38] a peak piezoelectrically induced stress of 3.7 MPa at 100 mV of excitation is estimated. From here, K_σ can be derived, depending on the sign of the piezoelectrically induced stress σ_{piezo} and assuming an isotropic magnetostriction (λ_{iso}) of 30 ppm.

$$K_\sigma = \frac{3}{2}\lambda_{iso}\sigma_{piezo} \tag{3}$$

For an excitation amplitude of 100 mV a value for the elastic energy density K_σ of 165 J/m^3 is generated at the tip. This is one quarter of the value of K_u meaning the ferromagnetic energy landscape is modulated, yet magnetisation reorientation is not expected. The addition of the two energy densities in the case of tensile stress may lead to domain wall motion already below the energy equilibrium of K_σ and K_u. Exciting the resonance at very high amplitudes in one case even lead to fracture through the entire composite along the centre of the *y*-axis, without facing dielectric breakdown (Supplemental, Fig. S3). Mermelstein *et al.*[39] studied a magnetoelastic ribbon under stress oscillations and found that the magnetic sensitivity thereof scales with λ_{iso}/H_k^2. This ideally demands material having a low anisotropy field, thus a being very soft magnetic, yet magnetostricitive for highest sensitivity.

Vibrational spectroscopy obtained by piezoelectrically exciting multiple frequencies while recording the out-of-plane mechanical activity, on any point of the sample surface, shown in Fig. 2c. The excitation amplitude for these spectral measurements lies below 1 mV per FFT line, because the total power is divided by the number of FFT lines. However, linearity of excitation amplitude with respect to the resulting displacement magnitude is verified up to about 500 mV. The three traces belong to different points on the cantilever surface, as indicated in Fig. 2a. Qualitatively the three spectra show the same principal peaks owing to mechanical resonances, though the excursion amplitudes differ. *Point 1* and *Point 2* are randomly chosen points on the cantilever surface in order to illustrate the validity of the aforementioned. The black trace shows the spectrum belonging to the centre of the tip, denoted *point 3*. The UM resonance mode at 516.3 kHz reveals the highest oscillation amplitude, nearly four times the excursion of the second largest resonance, located at 522.5 kHz. Additional resonances found at 548.8 kHz and 533.4 kHz excurse by at least an order of magnitude lower. Note that this mechanical measurement reveals six clearly distinguishable resonance peaks between 500 and 600 kHz. These resonances are absent in the converse magnetoelectric measurements as shown in Fig. 1d. This may have at least two reasons. First, the magnitude of the stress induced anisotropy is not sufficient to modulate the effective anisotropy, hence only little or no current is induced in the pickup-coil. Second, the mechanical modes are highly symmetric (or to a large extent), leading to effective cancellation of the induced current by nodal points leading to out-of-phase currents within the coil.

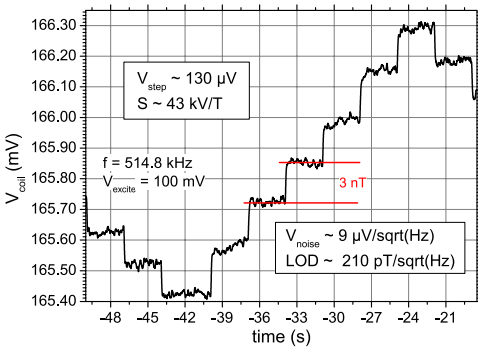

Figure 4. Magnetic staircase signal response, a DC magnetic field step of 3 nT is changed in staircase fashion every 3 seconds. The coil voltage at the modulation frequency changes, giving rise to a DC sensitivity of 43 kV/T. The standard deviation on the steps is about 10 µV, taking into account the noise equivalent bandwidth of the lock-in amplifier, the noise is estimated to be 9 $\mu V/Hz^{1/2}$.

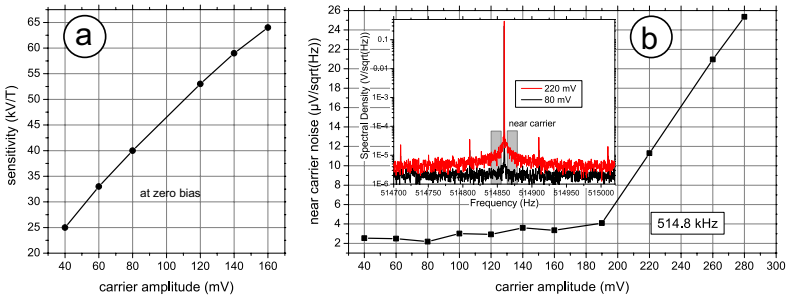

Figure 5. Sensor sensitivity and noise dependence on the applied carrier amplitude. (**a**) The sensitivity at zero field increases nearly linear with increasing carrier voltage (**b**) near carrier noise average, within the low frequency range (<20 Hz) for several carrier amplitudes, two principal regimes are identified, below about 200 mV the noise increases only slightly, roughly doubling over the complete interval, above 200 mV the noise increases nearly sevenfold within 100 mV. (**b**) Inset, shows the noise spectra for 80 mV and 220 mV excitation case, indicating the regime of averaging. At 220 mV of excitation a pronounced pedestal appears as well as broadband noise increase.

A simple mechanical mode analysis was performed using Abaqus CAE 2018 using a uniform mesh size of 50 µm. As both active layers are expected to contribute only negligibly to the overall oscillation behaviour, making up only about 1% of the composite thickness, with no vastly differing Young's moduli, a simple slab of silicon material having the same geometric dimensions is modelled. In order to best mimic the experimental study, a density of 2.330 g/cm^3, a Young's modulus (E) of 169 GPa and a Poisson's ratio (ν) of 0.27 was chosen for silicon[38]. Figure 2b shows the modelled resonance mode shape found at a frequency of 517.3 kHz, which matches the experiment to within 0.5%. The asymmetric clamping, on a section of the magnetostrictively coated surface of the structure matches the experiment with a fixed boundary condition. The colour code shows relative stress, indicating maximum compressive strain (deep blue) on the top side and simultaneous tensile strain peaking (red) on the bottom, along the y-axis towards the free end (cf. Supplemental, Vid. S2).

The magnetoelectric sensor provides high dependency of the induced voltage towards low amplitude DC signals, which is presented in Fig. 3. Figure 3a shows the induced RMS coil voltage amplitude after the low-noise amplifier with respect to an externally applied field H. When coming from negative saturation the induced voltage reaches above 800 mV at −30 µT, to vastly decrease until it reaches coercivity at 5 µT, where a phase reversal of the induced voltage takes place. This is attributed to the effective magnetic anisotropy switching direction along the y-axis of the cantilever, leading to a change of magnetisation and therefore flux direction change within the coil. The obtained loop is highly symmetric with respect to the saturation direction, owing to precise magnetic

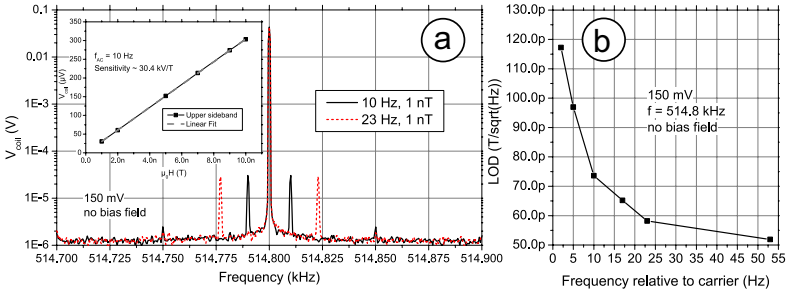

Figure 6. Spectral signal representation taken from behind the pickup coil amplifier. (**a**) Low frequency magnetic signals of 10 Hz and 23 Hz are applied by means of a cylindrical coil at an RMS amplitude of 1 nT. Sidebands form around the carrier due to amplitude modulation. Spurious power line frequency of 50 Hz is also up-converted. No DC magnetic field is present. (**a**) Inset coil voltage indicating the linearity of the modulation with respect to a sinusoidal test signal of 10 Hz at various field amplitudes, using a carrier amplitude of 150 mV. The slope reveals a sensitivity of 30.4 kV/T. (**b**) Limit of detection (LOD) for different test frequencies. An exponential growth in noise towards the carrier limits the performance.

annealing. At very high magnetic fields, where a saturation of the magnetic material is inevidable, the voltage output again drops to near zero.

Figure 4 shows the time-response of the induced coil voltage for a staircase of external DC fields changing every three seconds. The application of small fields relies on the linearity of the transfer function (Fig. 3b) given by the hysteretic behaviour of the amorphous magnetic material, and is well provided for fields through zero. A DC field sensitivity of 43 kV/T is obtained by dividing the output voltage step by the applied magnetic field step of 3 nT, corresponding well to the near-zero slope of Fig. 3b. The standard deviation of the signal on the steps gives rise to the noise floor, by taking into account the equivalent noise bandwidth (ENBW) settings of the lockin amplifier employing a 4th order filter, of about 9 μV/Hz$^{1/2}$, leading to an LOD of about 210 pT/Hz$^{1/2}$ at DC, for a signal-to noise ratio of 1.

From the mechanical (Q) and the frequency of vibration (f) a bandwidth (BW) can be estimated, within which the sensor will be able to detect signals above DC. For a $Q = 1000$ and $f = 515$ kHz, by using $BW = f/(2 \cdot Q)$ a low pass characteristic with a −3 dB point of 260 Hz can be estimated[40]. This corner frequency is well within the requirements for most biomagnetic applications.

The sensitivity towards magnetic fields is given in Fig. 5a, a nearly linear relation with increasing carrier amplitude is found. It can be thought of steepening the slope at zero bias field in Fig. 3b, consequently also leading to increased maximum induced voltages. Unfortunately, this near linear increase in sensitivity is not accompanied by a constant noise floor. Especially in the very low frequency regime of up to 20 Hz, of most interest for biomagnetic sensing, termed near carrier. As Fig. 5b reveals, this near carrier noise is divided into two distinct regimes, for a carrier amplitude below about 200 mV the noise near the carrier essentially doubles from about 2 μV/Hz$^{1/2}$ to 4 μV/Hz$^{1/2}$ for amplitudes ranging from 40 mV to about 200 mV. If the carrier amplitude is further increased, the noise reaches nearly 12 μV/Hz$^{1/2}$ at 220 mV, corresponding to a 20-fold slope compared to the former regime, this increase is by far dominating the benefit of an estimated sensitivity increase to about 85 kV/T at 220 mV. The noise increase in the near carrier regime is more than twofold compared to additional broadband noise (Fig. 5b, inset). This strong noise "pedestal" emerges due to up-conversion of low frequency noise and is connected to periodic magnetization processes within the magnetostrictive phase, leading to such an increase in low frequency noise[41–43]. This directly results in lower detection limits at low frequencies. The broadband noise increase may be attributed to white noise introduced by the emergence of eddy currents generated by excessive magnetization reorientation, initiated by stress anisotropy. Staying below a critical carrier voltage, in this case about 200 mV, will lead to modulation of the effective magnetic anisotropy but not lead to periodic magnetisation sweeping, thus avoiding strong noise contributions connected therewith[44].

Magnetic fields applied to the excited composite lead to an amplitude modulation at the excitation frequency, Fig. 6a shows typical output spectra. At 514.8 kHz the carrier amplitude is strongly present, corresponding to the U mode mechanical resonance, symmetric sidebands at $f + f_{AC}$ and $f - f_{AC}$ correspond to applied AC magnetic fields of 1 nT amplitude and frequencies of 10 Hz (solid) and 23 Hz (dashed). A spurious 50 Hz power line signal is also present symmetric to the carrier. The up-converted spectrum left and right of the carrier, contains the same informational content, hence why amplitude modulation has an inherent efficiency of 50%. The inset shows the linearity towards different AC magnetic field amplitudes. The slope of the fit equals a linear sensitivity of 30.4 kV/T, half of that given in Fig. 5a. Figure 6b shows the limit of detection (LOD) for different AC frequencies, exponentially improving from 117 pT/Hz$^{1/2}$ to 52 pT/Hz$^{1/2}$ at a frequency of 2 Hz to 53 Hz, respectively. The low frequency performance is limited by the up-conversion of 1/f noise.

Conclusion

A cantilevered mesoscopic ME structure was electrically excited in a mechanical resonance lying in the medium wave regime, at 514.8 kHz exhibiting a mechanical quality factor of about 1000. High speed mechanical vibration spectroscopy reveals that this oscillation leads to large out-of-plane displacements of the structure along its short axis and to high stresses coupled into the magnetostrictive phase. These prove sufficiently strong to alter the magnetic energy landscape by inverse magnetostriction. The observed mechanical U mode is verified by a FEM mode analysis, quantitatively finding a matching resonance frequency at 517.3 kHz, which is within 0.5% of the experimentally determined value. The simulation furthermore suites the experimentally determined deformation pattern.

If placed within a pickup coil the ME oscillator responds strongly to only very few of the determined mechanical vibration modes by sharp induced voltage peaks. The reason for this discrepancy between purely mechanical and converse ME measurements may lie in the fact that a large K_σ is necessary in order to make converse ME interaction effective. Most determined modes lead to weak K_σ and are therefore unable to energetically balance or overcome the statically present induced anisotropy. Furthermore, symmetry of mechanical oscillation modes may lead to spatially localised voltages generated along the structure, which may lie out of phase, effectively cancelling the inductive signal.

If the PE excitation (carrier) signal is set to match the mechanical resonance at 514.8 kHz, its induced voltage amplitude at the excitation frequency is modulated by external magnetic fields. The magnetic field sensitivity increases nearly linearly with carrier signal amplitude, reaching 64 kV/T at 160 mV. Conversely, the noise strongly increases once above an excitation voltage of about 200 mV, leading to excessive stress induced remagnetisation, accompanied domain wall propagation creating a dominant source of noise. Introduction of more sophisticated magnetic layers may lead to restrain of random domain wall motion, i.e. introducing an exchange biased interlayer has proven helpful[45,46]. A magnetic LOD of 210 pT/Hz$^{1/2}$ at DC is determined for a staircase test signal. For a 10 Hz signal an LOD of about 70 pT/Hz$^{1/2}$ was achievable, decreasing noise with distance to the carrier, leads to an LOD of about 50 pT/Hz$^{1/2}$ at 53 Hz. The presented setup enables array integration, as the pickup coil is operated entirely passive and no permanent magnetic bias field is required. Furthermore, a signal bandwidth of DC to 260 Hz meets the criteria of low frequency biomagnetic signals, additional improvement of the LOD is necessary in order to meet demands of biomagnetic signal amplitudes.

Received: 5 August 2019; Accepted: 21 October 2019;
Published online: 08 November 2019

References

1. Kowalska-Leszczynska, I. *et al*. Globally coherent short duration magnetic field transients and their effect on ground based gravitational-wave detectors. *Class. Quantum Grav.* **34**, 74002, https://doi.org/10.1088/1361-6382/aa60eb (2017).
2. Zhai, J., Dong, S., Xing, Z., Li, J. & Viehland, D. Geomagnetic sensor based on giant magnetoelectric effect. *Appl. Phys. Lett.* **91**, 123513, https://doi.org/10.1063/1.2789391 (2007).
3. Tumanski, S. *Handbook of Magnetic Measurements* (CRC Press, 2011).
4. Roux, A. *et al*. The Search Coil Magnetometer for THEMIS. *Space Sci Rev* **141**, 265–275, https://doi.org/10.1007/s11214-008-9455-8 (2008).
5. Sternickel, K. & Braginski, A. I. Biomagnetism using SQUIDs. Status and perspectives. *Supercond. Sci. Technol.* **19**, S160–S171, https://doi.org/10.1088/0953-2048/19/3/024 (2006).
6. Cohen, D. Magnetoencephalography. Evidence of Magnetic Fields Produced by Alpha-Rhythm Currents. *Science* **161**, 784–786, https://doi.org/10.1126/science.161.3843.784 (1968).
7. Cohen, D., Edelsack, E. A. & Zimmerman, J. E. Magnetocardiograms Taken Inside A Shielded Room With A Superconducting Point-Contact Magnetometer. *Appl. Phys. Lett.* **16**, 278–280, https://doi.org/10.1063/1.1653195 (1970).
8. Wikswo, J. P. SQUID magnetometers for biomagnetism and nondestructive testing. *Important questions and initial answers. IEEE Trans. Appl. Supercond.* **5**, 74–120, https://doi.org/10.1109/77.402511 (1995).
9. Ripka, P. & Janosek, M. Advances in Magnetic Field. *Sensors. IEEE Sensors J.* **10**, 1108–1116, https://doi.org/10.1109/JSEN.2010.2043429 (2010).
10. Koch, H. SQUID magnetocardiography. *Status and perspectives. IEEE Trans. Appl. Supercond.* **11**, 49–59, https://doi.org/10.1109/77.919284 (2001).
11. Stutzke, N. A., Russek, S. E., Pappas, D. P. & Tondra, M. Low-frequency noise measurements on commercial magnetoresistive magnetic field sensors. *Journal of Applied Physics* **97**, 10Q107, https://doi.org/10.1063/1.1861375 (2005).
12. Jander, A., Smith, C. & Schneider, R. pp. 1–14 (International Society for Optics and Photonics, 2005).
13. Paperno, E. & Grosz, A. A miniature and ultralow power search coil optimized for a 20 mHz to 2 kHz frequency range. *Journal of Applied Physics* **105**, 07E708, https://doi.org/10.1063/1.3072718 (2009).
14. Leroy, P., Coillot, C., Mosser, V., Roux, A. & Chanteur, G. An ac/dc magnetometer for space missions. Improvement of a Hall sensor by the magnetic flux concentration of the magnetic core of a searchcoil. *Sensors and Actuators A: Physical* **142**, 503–510, https://doi.org/10.1016/j.sna.2007.08.030 (2008).
15. Wang, Y., Li, J. & Viehland, D. Magnetoelectrics for magnetic sensor applications. Status, challenges and perspectives. *Materials Today* **17**, 269–275, https://doi.org/10.1016/j.mattod.2014.05.004 (2014).
16. Nan, C.-W., Bichurin, M. I., Dong, S., Viehland, D. & Srinivasan, G. Multiferroic magnetoelectric composites. Historical perspective, status, and future directions. *Journal of Applied Physics* **103**, 31101, https://doi.org/10.1063/1.2836410 (2008).
17. Palneedi, H., Annapureddy, V., Priya, S. & Ryu, J. Status and Perspectives of Multiferroic Magnetoelectric Composite Materials and Applications. *Actuators* **5**, 9, https://doi.org/10.3390/act5010009 (2016).
18. Nan, T., Hui, Y., Rinaldi, M. & Sun, N. X. Self-biased 215 MHz magnetoelectric NEMS resonator for ultra-sensitive DC magnetic field detection. *Scientific reports* **3**, 1985, https://doi.org/10.1038/srep01985 (2013).
19. Dolabdjian, C., Saez, S., Reyes Toledo, A. & Robbes, D. Signal-to-noise improvement of bio-magnetic signals using a flux-gate probe and real time signal processing. *Review of Scientific Instruments* **69**, 3678–3680, https://doi.org/10.1063/1.1149158 (1998).
20. Yarar, E. *et al*. Inverse bilayer magnetoelectric thin film sensor. *Appl. Phys. Lett.* **109**, 22901, https://doi.org/10.1063/1.4958728 (2016).
21. Dong, S., Zhai, J., Li, J. & Viehland, D. Near-ideal magnetoelectricity in high-permeability magnetostrictive/piezofiber laminates with a (2-1) connectivity. *Appl. Phys. Lett.* **89**, 252904, https://doi.org/10.1063/1.2420772 (2006).

22. Jahns, R., Greve, H., Woltermann, E., Quandt, E. & Knöchel, R. Sensitivity enhancement of magnetoelectric sensors through frequency-conversion. *Sensors and Actuators A: Physical* **183**, 16–21, https://doi.org/10.1016/j.sna.2012.05.049 (2012).
23. Petrie, J. *et al.* Shifting the operating frequency of magnetoelectric sensors. *Journal of Applied Physics* **111**, 07C714, https://doi.org/10.1063/1.3677840 (2012).
24. Hayes, P. *et al.* Electrically modulated magnetoelectric sensors. *Appl. Phys. Lett.* **108**, 182902, https://doi.org/10.1063/1.4948470 (2016).
25. Jahns, R. *et al.* Microelectromechanical magnetic field sensor based on Δ E effect. *Appl. Phys. Lett.* **105**, 52414, https://doi.org/10.1063/1.4891540 (2014).
26. Kittmann, A. *et al.* Wide Band Low Noise Love Wave Magnetic Field Sensor System. *Scientific reports* **8**(278), 4, https://doi.org/10.1038/s41598-017-18441- (2018).
27. Yarar, E. *et al.* Low temperature aluminum nitride thin films for sensory applications. *AIP Advances* **6**, 75115, https://doi.org/10.1063/1.4959895 (2016).
28. McCord, J. Progress in magnetic domain observation by advanced magneto-optical microscopy. *J. Phys. D: Appl. Phys.* **48**, 333001, https://doi.org/10.1088/0022-3727/48/33/333001 (2015).
29. Jahns, R. *et al. In 2011* IEEE Int*ernational Symposium on Medical Measurements and Applications*, pp. 107–110 (IEEE, 2011).
30. Tumanski, S. Induction coil sensors—a review. *Meas. Sci. Technol.* **18**, R31–R46, https://doi.org/10.1088/0957-0233/18/3/R01 (2007).
31. Ripka, P. Magnetic Sensors and Magnetometers. *Meas. Sci. Technol.*, **13**, 645, https://doi.org/10.1088/0957-0233/13/4/707.
32. Primdahl, F. The fluxgate magnetometer. *J. Phys. E: Sci. Instrum.*, **12**, 241, https://doi.org/10.1088/0022-3735/12/4/001.
33. Hayes, P. *et al.* Electrically modulated magnetoelectric AlN/FeCoSiB film composites for DC magnetic field sensing. *J. Phys. D: Appl. Phys.* **51**, 354002, https://doi.org/10.1088/1361-6463/aad456 (2018).
34. Guo, M. & Dong, S. A resonance-bending mode magnetoelectric-coupling equivalent circuit. *IEEE transactions on ultrasonics, ferroelectrics, and frequency control* **56**, 2578–2586, https://doi.org/10.1109/TUFFC.2009.1346 (2009).
35. Naeli, K. & Brand, O. Dimensional considerations in achieving large quality factors for resonant silicon cantilevers in air. *Journal of Applied Physics* **105**, 14908, https://doi.org/10.1063/1.3062204 (2009).
36. Kirchhof, C. *et al.* Giant magnetoelectric effect in vacuum. *Appl. Phys. Lett.* **102**, 232905, https://doi.org/10.1063/1.4810750 (2013).
37. Ohring, M. *Materials science of thin films. Deposition and structure*. 2nd ed. (Academic Press, San Diego, Calif., 2002).
38. Hopcroft, M. A., Nix, W. D. & Kenny, T. W. What is the Young's Modulus of Silicon? *J. Microelectromech. Syst.* **19**, 229–238, https://doi.org/10.1109/JMEMS.2009.2039697 (2010).
39. Mermelstein, M. D. Magnetoelastic amorphous metal fluxgate magnetometer. *Electronics Letters* **22**, 525–526, https://doi.org/10.1049/el:19860358 (1986).
40. Mertz, J., Marti, O. & Mlynek, J. Regulation of a microcantilever response by force feedback. *Appl. Phys. Lett.* **62**, 2344–2346, https://doi.org/10.1063/1.109413 (1993).
41. Zhuang, X., Lam Chok Sing, M. & Dolabdjian, C. Investigation of the Near-Carrier Noise for Strain-Driven ME Laminates by Using Cross-Correlation Techniques. *IEEE Trans. Magn.* **49**, 120–123, https://doi.org/10.1109/TMAG.2012.2220340 (2013).
42. Zhuang, X. *et al.* Sensitivity and Noise Evaluation of a Bonded Magneto(elasto) Electric Laminated Sensor Based on In-Plane Magnetocapacitance Effect for Quasi-Static Magnetic Field Sensing. *IEEE Trans. Magn.* **51**, 1–4, https://doi.org/10.1109/TMAG.2014.2356852 (2015).
43. Burdin, D. A., Chashin, D. V., Ekonomov, N. A., Fetisov, Y. K. & Stashkevich, A. A. High-sensitivity dc field magnetometer using nonlinear resonance magnetoelectric effect. *Journal of Magnetism and Magnetic Materials* **405**, 244–248, https://doi.org/10.1016/j.jmmm.2015.12.079 (2016).
44. Bittel, H. & Storm, L. *Rauschen* (Springer Berlin Heidelberg, Berlin, Heidelberg, 1970).
45. Jovičević Klug, M. *et al.* Antiparallel exchange biased multilayers for low magnetic noise magnetic field sensors. *Appl. Phys. Lett.* **114**, 192410, https://doi.org/10.1063/1.5092942 (2019).
46. Röbisch, V. *et al.* Exchange biased magnetoelectric composites for magnetic field sensor application by frequency conversion. *Journal of Applied Physics* **117**, 17B513, https://doi.org/10.1063/1.4913814 (2015).

Acknowledgements
The authors would like to appreciate rewarding discussions with Dirk Meyners. The authors would like to thank the German Research Foundation (Deutsche Forschungsgemeinschaft, DFG) who funded this work under Collaborative Research Centre SFB1261 "Magnetoelectric Sensors: From Composite Materials to Biomagnetic Diagnostics".

Author contributions
All authors interpreted the data, discussed the results, reviewed, and commented on the manuscript. E.Q., J.M., M.H., R.K. and Y.F. designed experiments and supervised the research. P.H. Designed the composite structure and designed and built coil assembly and amplifier. Designed and conducted measurements. Performed numerical simulations. Created artwork and plots. V.S. Fabricated the composites. S.T. Conducted measurements. P.D. Created MATLAB software code and interpreted measurements. M.J.K. Performed MOKE imaging and aided in result interpretation. A.T. Aided in design of amplifier board. D.B. Discussions interpreting data. A.W. and R.W. conducted Vibrometry measurements.

Competing interests
The authors declare no competing interests.

Additional information
Supplementary information is available for this paper at https://doi.org/10.1038/s41598-019-52657-w.

Correspondence and requests for materials should be addressed to E.Q.

Reprints and permissions information is available at www.nature.com/reprints.

Publisher's note Springer Nature remains neutral with regard to jurisdictional claims in published maps and institutional affiliations.

4.1 Conclusion

The U1 mechanical mode was studied using far lower excitation voltages than in a prior study using U2 mode (see section 3), resulting in an even improved performance. The LOD was determined in a low frequency range between DC and 53 Hz, showing an improvement towards higher frequencies as low frequency noise is left behind. A clear relation between noise generation and excitation amplitude was found, leading to an optimum between sensitivity and noise at moderate excitation voltage below 200 mV. This finding is in line the theoretical estimations presented in section 3.6.1.

4.2 Pickup Coil Tuning

Utilising a pickup coil for the detection of the converse ME signal offers potential intrinsic amplification by exploiting its self-resonance and subsequently buffering the output by a high impedance amplifier input as described in section 4 on page 83. This self-resonance frequency (SRF) is an effect occurring in any real electrical component originating from parasitic capacitances, inductances and resistances always existing, even if small. A pickup coil intuitively represents an inductor, its inductance L proportional to the square of the windings $\propto N^2$ presents its main purpose. But any long wire is associated with an ohmic resistance R. Finally, between many layers of insulated wire the least intuitive parameter forms, the inter-winding capacity C. Together they form the f_{SRF} given by equation (4.1). Note that this is actually independent of R,

$$f_{SRF} = \frac{1}{2\pi\sqrt{LC}} = \frac{1}{2\pi\sqrt{L(C_{coil} + C_{tune})}} \tag{4.1}$$

Pickup coils were wound using less turns, as would be necessary in order to match the mechanical resonance frequency of the ME composite, thus by introducing a trimmer capacitor C_{tune} in parallel to the coil it is possible to reduce the coil resonance without adding additional noise. Figure 4.1 on the facing page shows the effect of a small additional capacity C_{tune} on the SRF of the coil, even a small value of 20 pF leads to a lowering of the coil SRF by 90 kHz. The inset shows electrical parameters R, L and C of which values are determined using an *Agilent 4294A Precision Impedance Analyzer* and fitted using the indicated model of the coil. A large DC resistance R should be avoided, as it lowers the Q factor of the coil by $\propto {}^1/_R$. $V1$ is the excitation source and is used for simulation purposes in *LTspice* only. At elevated frequencies the skin effect plays a role, confining electrical conductivity towards the outer shell of a conductor and thus enlarging the impedance. In order to counter this effect at medium wave frequencies litz wire, a conductor made up of several insulated thin litzes, in order to

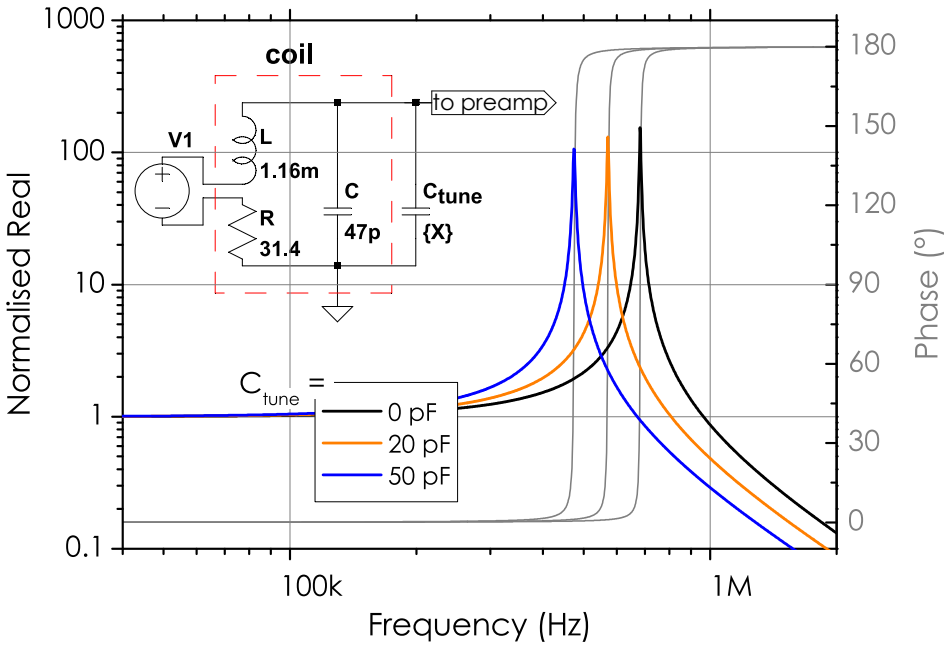

Figure 4.1: Simulation of coil self-resonance for different tuning capacities C_{tune} using *LTspice*, the untuned coil has a resonance frequency of about 680 kHz. A capacity as small as 20 pF is sufficient to lower the coil self resonance by 90 kHz. (inset) Shows the experimentally determined parameters obtained by impedance analysis.

increase the conducting shell area, is employed. In this work a single wire of about 100 µm diameter is used, this is well on the order of the skin depth for copper at an operation frequency of 500 kHz. The skin depth δ depends on the electrical resistivity ρ, the frequency ω, the permeability μ, by $\delta = \sqrt{\frac{2\rho}{\omega\mu}}$. Inserting numbers for copper at 500 kHz yields a depth of about 90 µm at which the current density has reached 37 % of its initial value on the skin.

Although tuning of the pickup coil strongly increases the sensitivity of the composite, as the mechanical and electrical resonances add up and deliver a strong amplification of the signal, this is also true for the noise within the same frequency band. Thus this method is well suited for amplifying the entire system noise into the µV range, lowering demands towards noise in following mixers and subsequent baseband A/D conversion.

Chapter 5

Recent Developments

5.1 Advanced Magnetostrictive Films Combined with U1 Mode Resonance

Recent developments within the CRC1261 lead to the implementation of exchange biased (EB) magnetostrictive films [Lag+12] [Röb+15]. Exchange biasing of magnetic films is not uncommon, usually it provides an elegant solution in order to set a working point for a device or sensor by imprinting a unidirectional anisotropy and thus avoiding otherwise necessary permanent magnets or additional electronics in order to set the working point. Two recent examples are provided by Lage [Lag+12] employing EB in order to set the working point in an ME composite maximizing $\alpha_{ME}(H_{ext=0})$; Tavassolizadeh [Tav+15] utilised exchange biasing in order to maximize the effect of strain on magnetic tunnel junctions at zero external bias field. In this work this additional unidirectional anisotropy acting on the magnetostrictive layer is used for the efficient suppression of magnetic noise, arising from various processes associated with uncontrolled remagnetisation processes and especially activity of domain walls [Jov+19]. There are many strategies of employing exchange bias, but fundamentally exchange bias is an interfacial effect which relies on an interface between antiferromagnet and ferromagnet, thus the strength of this anisotropy is primarily dependent on the distance i.e. the thickness of the ferromagnetic material deposited on a antiferromagnetic material [NS99]. There are certain limiting cases to this general rule, but these need not be taken into account in the discussed composite sensors. Likewise the thickness of the antiferromagent does not play such a critical role, unless a certain thickness of several nanometers is maintained [van+00]. For in-depth coverage on the exchange bias effect it is advisable to consult the aforementioned literature, the topic is too dense to be discussed in great detail, the focus here is limited to experimentally relevant aspects.

After [NS99] following relation will be of interest for the following;

$$H_{EB} \propto \frac{1}{t_{FM}} \tag{5.1}$$

Where, H_{EB} is the exchange bias field and t_{FM} is the thickness of the ferromagnetic film to be biased. Figure 5.1 schematically shows the effect of this unidirectional anisotropy on parallel and orthogonal magnetisation loops, (a) shows the paradigmatic picture arising if a loop is recorded parallel to the exchange bias direction, the loop shift H_{EB} is clearly visible. An ideal hard axis loop is found in (b), exactly as it would be expected for a uniaxial anisotropy of the same magnitude.

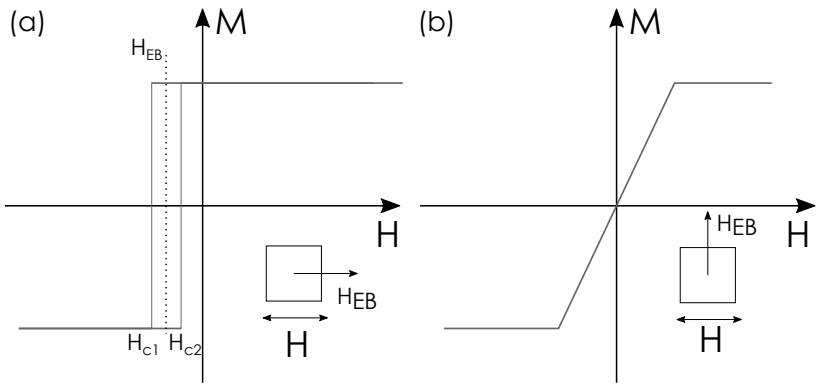

Figure 5.1: Ideal magnetisation curves showing the effect of only an exchange bias field H_{EB} on orthogonal sample orientations in an external field. (a) Bias parallel to the external field H, it effectively shifts the loop by H_{EB}. Two unsymmetrical coercive fields result, H_{c1} and H_{c2}. (b) Bias perpendicular to H, a common ideal hard axis loop results.

Figure 5.2 on the next page shows the MO domain images of a single FeCoSiB layer and of an EB layer stack in remanent state, (a) clearly alternating magnetic domain contrast is visible, as explained in figure 3.14 on page 68 (b) shows complete absence of magnetic domain contrast, only slightly shaded areas suggest either; a local rotation of magnetisation or a lower layer may locally exhibit opposite magnetisation direction thus lightening the MO contrast. In the first 50 µm from the edge vertically aligned closure domains form, which yield no contrast using horizontal sensitivity.

As stated, once having antiferromagnetic interlayers in place for the purpose of exchange biasing the adjacent soft magnetostrictive layers, a variety of design options are opened. Primarily by the deposition, where the thickness t_{FM} plays a crucial role (equation (5.1)) in tailoring the force of the bias on the magnetisation. For the simplest case exchange bias multilayer sensors undergo classic field annealing, which will align the H_{EB} parallel to K_u and lead to a straightforward situation in figure 5.1, termed parallel exchange bias (PEB). Secondarily, advanced thermal treatments come at no

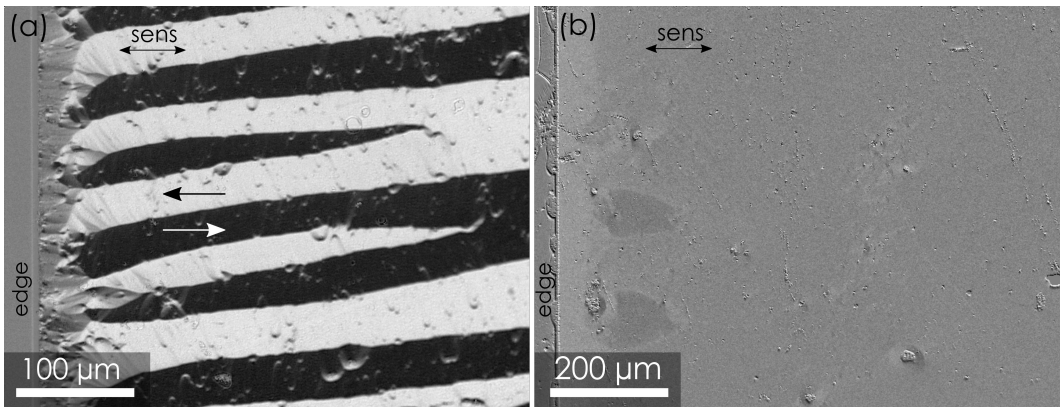

Figure 5.2: Magneto optic (MO) images of magnetostrictive layers in magnetic remanence, the film edge can be seen on the left. The MO sensitivity is set horizontal. (a) Alternating domain contrast as indicated follow the uniaxial anisotropy. About 50 µm inwards from the film edge closure domains lead to low contrast, as the magnetisation points vertically here. (b) Exchange biased film shows homogeneous contrast, no evidence of magnetic domain patterns. A slightly lighter contrast is visible towards the edge, this may stem from the lower layer pointing in opposite direction.

additional fabrication efforts and involve temperature as well as field time profiles in order to imprint arbitrary orientations of H_{EB} towards K_u. Thus, in order to avoid asymmetry and associated magnetic instability of PEB layer stacks, magnetic flux closure of adjacent multilayer films achieves higher stability of antiparallel stacks [Jov19], these sophisticated systems are termed anti parallel exchange bias (APEB) as a result the net magnetisation at remanence vanishes and ideally also the loop shift H_{EB}, because effects of adjacent layers cancel out for even layer counts. Jovicevic-Klug et al. further describes such advanced heat treatments on PEB and APEB layer systems in [Jov19].

Any EB layer system may have tremendous influence on the micromagnetic domain situation, a comparison of typical domain images of single layer FeCoSiB and an exchange biased multilayer system are shown in figure 5.2. A nearly perfectly homogeneous contrast is seen for the EB case in figure 5.2b, whereas figure 5.2a shows a forest of alternating domains with a pronounced closure domain regime towards the film edge. The main purpose of exchange bias multilayer systems in electrically modulated ME sensors is to facilitate reduction of magnetically generated noise, rather than biasing the MS layer to a specific working point. Further discussion about magnetic noise is given in section 1.2.2 on page 23. Therefore it should not be disregarded that the introduction of EB inevitably leads to an additional anisotropy which will, to some extent, add to existing anisotropies rendering the material magnetically harder i.e. increasing K_{eff}. For a larger K_{eff} the same piezoelectric excitation amplitude will lead to less $\frac{d\phi}{dt}$ within the coil, leading to reduced sensor sensitivity. A proportional shift of the ratio

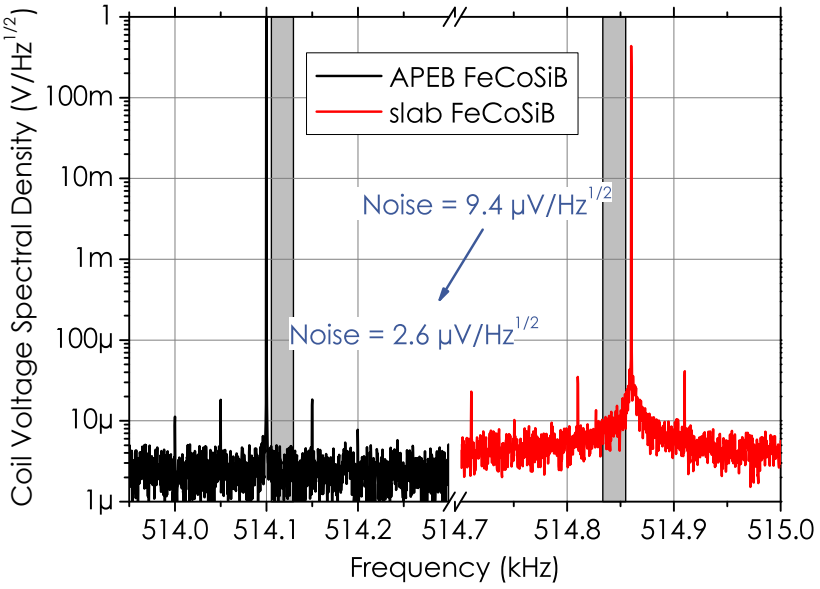

Figure 5.3: Coil voltage spectral density for two similar resonators excited at comparable excitation amplitude in U1 mode. Near carrier noise is averaged over the indicated region. Antiparallel exchange biased (APEB) FeCoSiB shows flat white noise around the carrier at 514.1 kHz, in contrast single slab FeCoSiB shows a 3.6-fold increased noise in carrier frequency (at 514.85 kHz) vicinity (i.e. at low signal frequencies).

of intrinsic sensitivity (i.e. signal) and generated noise misses the aim. Consequently an optimization task arises between elevated total anisotropy causing lower sensitivity while maintaining low magnetic noise contributions in order to effectively gain in signal-to-noise ratio. Figure 5.3 shows an exemplary comparison of the induced coil voltage noise density of two resonators excited at comparable levels in U1 mode with simple slab FeCoSiB and with Antiparalell exchange bias multilayer. The large peak is the excitation carrier, 50 Hz peaks and its harmonics are due to power line coupling, the noise floor in the vicinity of the carrier is averaged in the region from about 5 ... 30 Hz. This low frequency noise is dramatically decreased about 3.6-fold using the EB multilayer stack, especially the noise "pedestal" at low frequencies around the carrier is flattened when employing EB stacks. At larger frequencies from the carrier the effect of EB FeCoSiB is less, here the noise decrease is about twofold.

In the following, selected results of exchange biased samples are presented. Most promising of the investigated layer systems have even numbered FeCoSiB layers of 500 nm thickness.

EB-FeCoSiB

A sensor composite consisting of a total of 2 µm EB FeCoSiB made up of 4 repetitions of 500 nm amorphous FeCoSiB layers which are deposited onto the biasing stack consisting of Ta(5)/Cu(3)/Mn_3Ir(8) (values in nm). On the flipside of the composite 2 µm aluminium nitride used for excitation in U1 mode. The surrounding pickup coil is tuned to somewhat amplify the voltage induced near the mechanical resonance and simultaneously bandpass filter the output, see section 4.2 on page 94.

The shape of the bias curve shown in figure 5.4 resembles one of a sensor without exchange bias (section 4 on page 83 Fig. 3), showing significantly reduced hysteresis. The characteristic maxima at about 500 mOe remain as in the case of an unbiased composite, they occur at about one sixth the field value than previously reported by [Mer92]. Following towards smaller fields, a steep drop of induced voltage towards zero external field revealing the most sensitive region. Towards higher fields larger than 1 Oe the induced coil voltage rapidly drops (formerly U_{ind}), this is due to the magnetisation angle Φ being lowered towards the long cantilever axis with increasing H_{ext}, consequently wiggling the magnetisation (within a $d\Phi$) is less efficient, see figure 3.24 on page 80. Figure 5.5(a) shows a magnification of the situation presented in

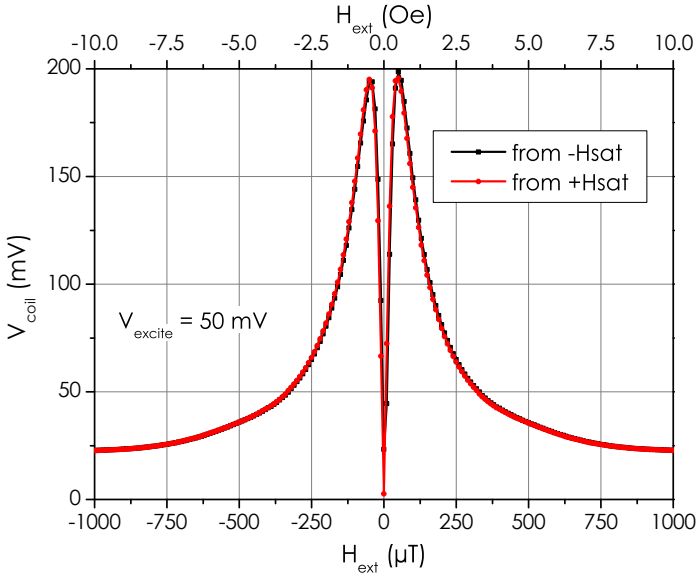

Figure 5.4: Induced voltage with respect to the external field H_{ext} using an excitation amplitude of 50 mV in U1 mode. Nearly no hysteresis is observed, as the two loops from opposing saturation directions match well.

figure 5.4 revealing some hysteresis as well as a wide linear range. Note that a much larger excitation voltage of 400 mV was used, although this poses an eightfold signal increase, the impact on the characteristic points of the curve remain minute. The linearity of the induced coil voltage (V_{coil}) with respect to H_{ext} extends from zero field

above typical earth's magnetic field magnitude at 25 ... 40 µT. Zooming even closer, (b) reveals the magnitude of hysteresis, as well as an asymmetry in the loop caused by the EB, given by the intersection of the traces at −750 nT. This asymmetry leads to two different sensitivities achievable after magnetic saturation, indicated in (b), when coming from negative saturation $-H_{sat}$ a zero field sensitivity of about 3.4 kV/T is obtained, when releasing the field from the opposing direction ($+H_{sat}$), a sensitivity of 9.3 kV/T, or a 2.7 fold increased sensitivity is achieved. The points in the amplitude

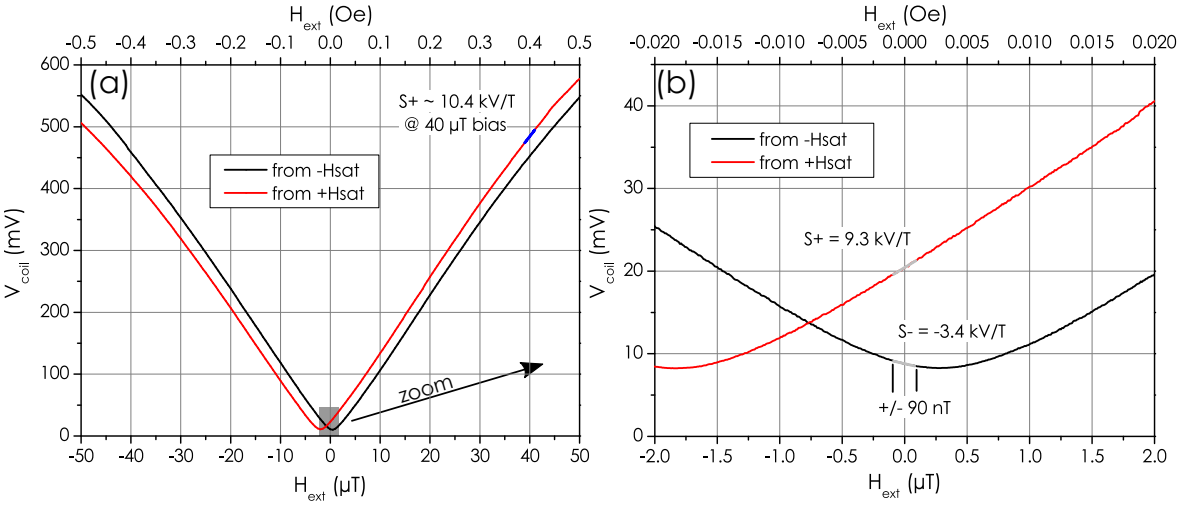

Figure 5.5: Induced voltage response showing the low field regime. The excitation voltage is 400 mV. (a) a wide linear range with high sensitivity, exceeding that of the earth's field magnitude. Hysteresis as well as a slightly shifted curve is revealed. (b) high resolution curve recorded in increments of 10 nT clearly shows that sensitivity depends on direction of prior magnetic saturation. The loop shift is caused by the EB.

response at −1.8 µT and 300 nT show minimum slope towards H_{ext}, in steps of 10 nT, consequently very low performance arises using the fundamental U1 mode in the close vicinity to these points. Figure 5.6 on the following page shines light on the phase response of the induced coil voltage, exposing a gradual phase reversal of nearly 180 ° as induced voltage is decreasing. The highest slope is found around the points of minimum amplitude sensitivity as indicated by dashed arrows. The slope obtained from the phase response is less susceptible to the direction of prior saturation, resulting in a difference of less than 5 % phase sensitivity. The phase sensitivity remains constant for even large variations of excitation amplitude. Figure 5.7a shows the influence of the magnetic saturation towards hysteresis and linearity of the sensor composite to exposed non-saturating, minor fields. Medium variations of the external field in the range of earth's magnetic field would be expected to regularly occur in an actual device application, for example upon device rotation within earth's permanent magnetic field. After initial magnetic saturation by a large field magnitude of 15 mT and return to remanence, a small, minor field loop is recorded from −20 ... 20 µT and back, this

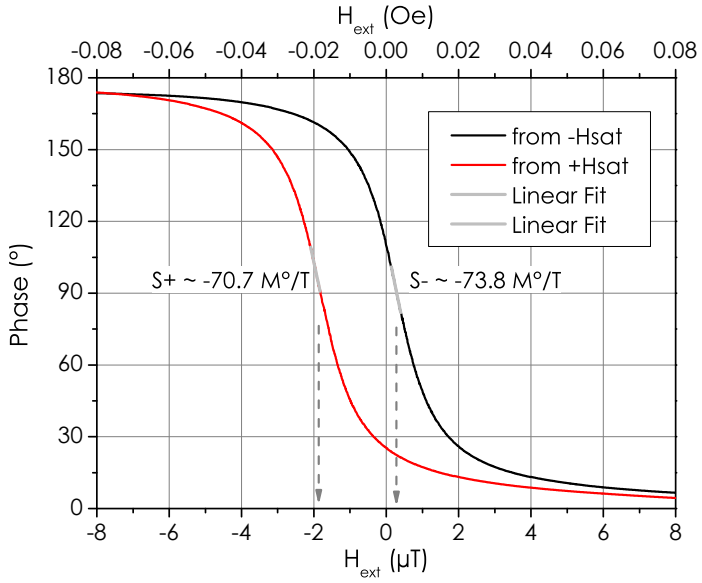

Figure 5.6: Phase response of the induced coil voltage with respect to external field H_{ext} at an excitation voltage of 400 mV. A phase sensitivity of up to 73.8 $^{\mathrm{M}^\circ}/_{\mathrm{T}}$ is found around 0.3 µT. The dashed arrows indicate the field values of minimum amplitude sensitivity as shown in figure 5.5. Grey lines give interval for linear sensitivity determination.

is done for both directions of initial saturation. The effect of the hysteresis persists throughout the loops, thus creating two distinct minor loops, whereas the loop derived starting from positive saturation shows much less amplitude sensitivity at zero external field. It is clearly seen that the hysteresis which each loop is undergoing is very small, thus leading to a maximum shift in the induced coil voltage of 2 mV. Figure 5.7b shows the case for prior negative saturation, at a smaller excitation voltage of 100 mV, indicating that the loops remain unaltered in shape and maintain linearity towards the exciting voltage amplitude, consequently the induced voltage at the plot extremes as well as the maximum sensitivity is exactly fourfold. The situation in (b) leads to low amplitude response around zero field, nevertheless it shows very symmetric coil voltage amplitude for a given field magnitude, however, the maximum of the phase sensitivity is now shifted to zero field. A so called staircase response is recorded in order to probe for small DC field performance. For this purpose the demodulated coil voltage is recorded as a time series while the external magnetic field amplitude is altered in a staircase fashion using a fixed delay time.

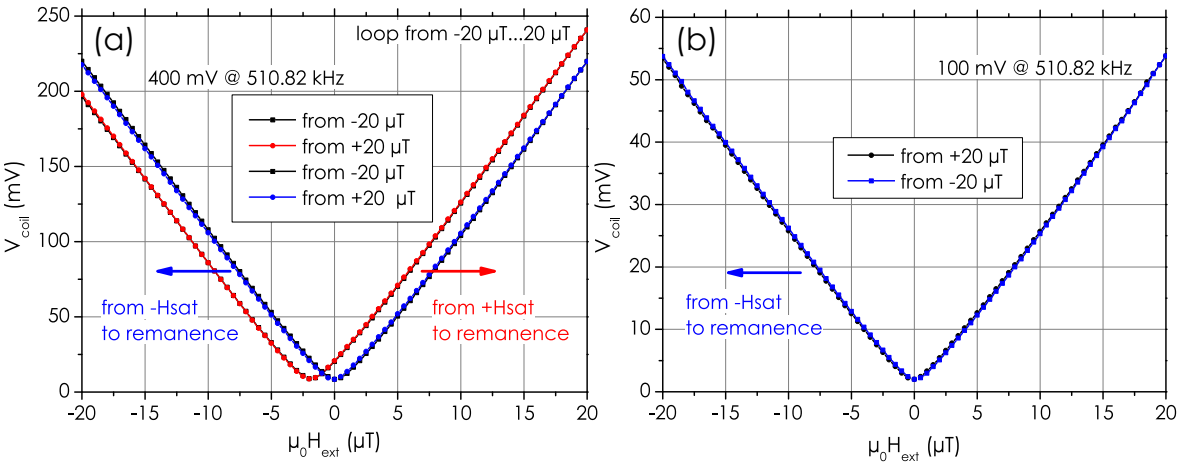

Figure 5.7: Minor field loops showing the influence of prior saturation in EB composites, loops are recorded from remanent state. (a) the loop shift is determined by the prior saturation direction, near no hysteresis is visible. Measurement performed using an excitation amplitude of 400 mV. (b) 100 mV excitation does not change the minor loop characteristics such as hysteresis, the induced voltage amplitude is decreased in proportionally to the excitation, mind the scale.

Figure 5.8 shows such a measurement for an excitation voltage of 400 mV in U1 mode. As a result the induced coil voltage is altered by about 100 µV for a field step of 2 nT leading to a DC sensitivity of S_{DC} =50 $^{\mathrm{kV}}/_{\mathrm{T}}$. The noise floor in this measurement is calculated by taking the mean noise value on a step, which corresponds to about 4 µV and dividing this by the noise equivalent power bandwidth (NEPBW) of the lock-in amplifier [Zur16]. The voltage noise density is calculated using the low-pass filter bandwidth f_{-3dB} and its equivalent to a perfect brick wall filter of infinite steepness characteristic f_{NEP}, thus $\frac{f_{NEPBW}}{f_{-3dB}}$ yields a dimensionless factor of 1.13 or in other words 13 % wider bandwidth results from the 4$^{\mathrm{th}}$ order filter than would have resulted for an ideal filter of the same corner frequency. This factor approaches a value of 1 with increasing filter orders, since the difference towards an ideally steep filter is decreased. In order to not produce strong overshoot upon transients provoked by the external magnetic field change, a rather wide filter bandwidth of 3.8 Hz or time-constant of 1.35 ms is used. Finally, the voltage noise is obtained by dividing the ripple of the induced voltage by the low-pass filter characteristics, yielding $N_{DC} \approx {}^{4\,\mu\mathrm{V}}/\sqrt{1.13 * 3.8\,Hz}$ a noise floor of about $2\,^{\mu\mathrm{V}}/\sqrt{\mathrm{Hz}}$. Dividing this DC noise floor N_{DC} by the DC sensitivity S_{DC} results in an LOD of about $40\,^{\mathrm{pT}}/\sqrt{\mathrm{Hz}}$ towards DC fields.

The signal dynamics in the presented measurement do not exceed 30 dB or 2.5 orders of magnitude, this is far lower than previously presented by [Don+06b] which is 45 dB or 3.5 orders of magnitude and three orders as reported by Srinivasan et. al. [SSP14]. The sensitivity is at least two orders of magnitude larger than the value of 400 $^{\mathrm{V}}/_{\mathrm{T}}$ reported by Dong et. al. The sensitivity published by Srinivasan et. al. of 500 $^{\mathrm{mV}}/_{\mathrm{T}}$ is less than

that of commercial hall sensors [SSP14]. AC magnetic signals lead to modulation of

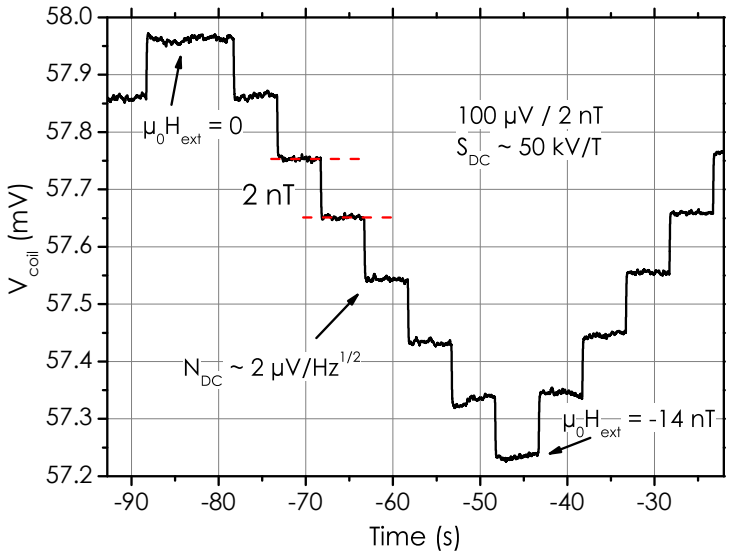

Figure 5.8: Staircase response. Time domain of induced coil voltage V_{coil} towards small field steps while excited at 400 mV in U1 mode. The external field H_{ext} is changed every 5 s by 2 nT. A change of about 100 mV per step leads to a DC field sensitivity S_{DC} of 50 $^{\mathrm{kV}}/_{\mathrm{T}}$. Calculating the standard deviation of the ripple on the steps leads to a noise floor of about $N_{DC} \approx 2\,^{\mu\mathrm{V}}/\sqrt{\mathrm{Hz}}$. Taking the ratio of the two leads to an LOD of 40 $^{\mathrm{pT}}/\sqrt{\mathrm{Hz}}$ at DC.

the carrier amplitude [Hay+19], i.e. the demodulated coil voltage as previously shown in the staircase response. The magnetic AC field frequency regime of prime interest for naturally occurring biomagnetic signals lies below about 150 Hz as discussed in section 1.1.2 on page 3. Hence, sinusoidal magnetic test signals of frequencies in the range of 1 ... 150 Hz established as common ground within the ME community in the recent decade[Wan+11],[Zhu+15b],[Gil+11],[Zab+16].

Figure 5.9a shows the spectral response taken from behind the coil amplifier upon application of a 10 Hz test signal of 2 nT_{rms} amplitude. The measurement procedure involving a high speed lock-in amplifier is described in further details in [Hay+19]. When Fourier transformed, the amplitude modulation (AM) leads to a spectrum showing two symmetric sidebands around the carrier excitation caused by the applied magnetic test field H_{AC} at $f_{res} \pm f(H_{AC})$. Calculation of the AC field sensitivity S is performed by dividing the sideband amplitude (of $V_{coil} \approx 67\,\mu\mathrm{V}$) by the amplitude of the calibrated test signal $\mu_0 H_{AC} = 2\,\mathrm{nT}$, yielding a sensitivity value of $S = 33.5\,^{\mathrm{kV}}/_{\mathrm{T}}$. This sensitivity S is inherently 50% smaller compared to the DC sensitivity S_{DC}, this is caused by the fact that both symmetric sidebands carry the same information, hence $S = \frac{S_{DC}}{2}\sqrt{2} = 35.36\,^{\mathrm{kV}}/_{\mathrm{T}}$. Comparing S_{DC} to S shows a minor discrepancy of about 5 %, this is likely caused by slightly differing working points. The sensitivity mainly

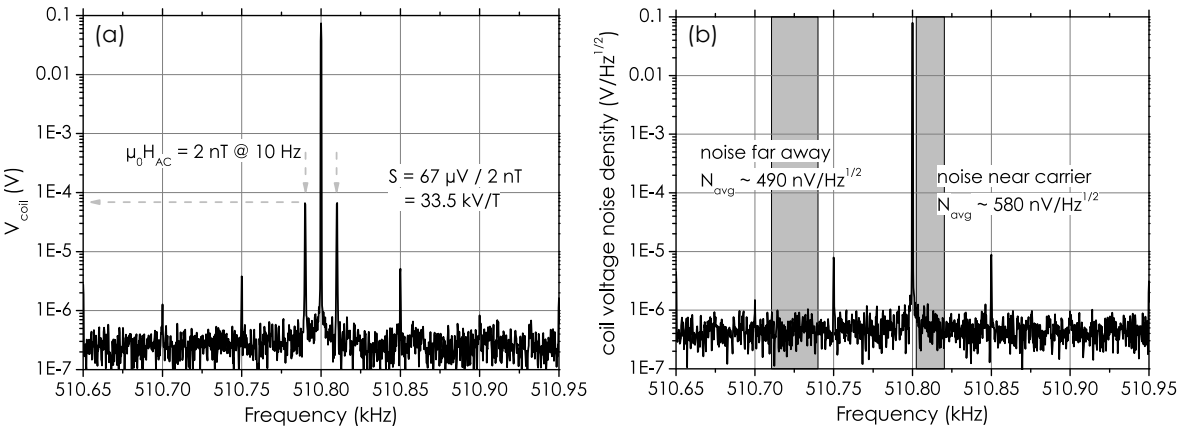

Figure 5.9: Sensitivity and noise towards a 10 Hz magnetic test signal in the frequency domain. (a) Coil voltage revealing symmetric sidebands around the carrier excitation at $f_{res} \pm f(H_{AC})$ containing the AC signal information. Spurious power line disturbances are located at $f_{res} \pm 50\,\mathrm{Hz}$ and $\pm 100\,\mathrm{Hz}$. Division of the sideband amplitude by the test signal amplitude leads to the sensitivity. (b) The noise floor around the excitation frequency reveals an average of about $580\,{}^{\mathrm{nV}}/\sqrt{\mathrm{Hz}}$ within $2 \ldots 20\,\mathrm{Hz}$ leading to an LOD of $17\,{}^{\mathrm{pT}}/\sqrt{\mathrm{Hz}}$, the noise reduces down to $490\,{}^{\mathrm{V}}/\sqrt{\mathrm{Hz}}$ at frequencies $> 20\,\mathrm{Hz}$ resulting in about $15\,{}^{\mathrm{pT}}/\sqrt{\mathrm{Hz}}$ at higher frequencies.

depends on the piezoelectric excitation amplitude, the amount of magnetic material present and the pickup coil characteristics as discussed in equation (3.5), the coil quality factor linearly amplifies the entire coil output, further details in section 4.2 on page 94.

Figure 5.9b shows the situation in terms of voltage noise density without any test signal active, enabling noise floor estimation. In close carrier vicinity $2 \ldots 20\,\mathrm{Hz}$ an average noise of $580\,{}^{\mathrm{V}}/\sqrt{\mathrm{Hz}}$ is found. Dividing this N_{avg} by the sensitivity leads to the LOD in terms of equivalent magnetic noise[1] of $\frac{N_{avg}}{S} = 17\,{}^{\mathrm{pT}}/\sqrt{\mathrm{Hz}}$. This value poses a fourfold performance increase towards single layer FeCoSiB exhibiting $70\,{}^{\mathrm{pT}}/\sqrt{\mathrm{Hz}}$ at 10 Hz [Hay+19].

The LOD comprises a trade-off between sensitivity maximisation and noise emergence, thus for a given sensor system the excitation amplitude is the most obvious parameter for optimisation. Figure 5.10a directly relates the resulting sideband amplitude or, if divided by the test signal amplitude, the sensitivity to the carrier amplitude. Initially a linear relation is found, from $50 \ldots 500\,\mathrm{mV}$ reaching highest sensitivity with $40\,{}^{\mathrm{kV}}/\mathrm{T}$ at 500 mV. A gradual decay of sensitivity sets in at a excitation voltage of about 600 mV. This decrease in sensitivity is expected to stem from mechanical non-linearities setting in at high drive amplitudes, effectively resulting in a shift of resonance frequency and thus leading to lowering of sideband amplitude without re-tuning the excitation

[1] This is often confused with "resolution", "detectivity" or "sensitivity limit" given in units of field.

frequency. This dynamic effect was previously found in similar ME structures by the author [Fet+18]. Nevertheless the near carrier noise evolution is shown in figure 5.10b showing a gradual increase up to an excitation amplitude of 500 mV from where a vast noise increase is observed, as a result the LOD is plotted showing an optimum at 400 mV excitation amplitude. The noise contribution at 600 mV overcompensates the sensitivity increase of 15 % towards the excitation level of 400 mV. Characteristically the curve shape resembles that obtained for simple FeCoSiB resonators of section 4 on page 83, starting gradual leading to exponential noise increase above about 500 mV.

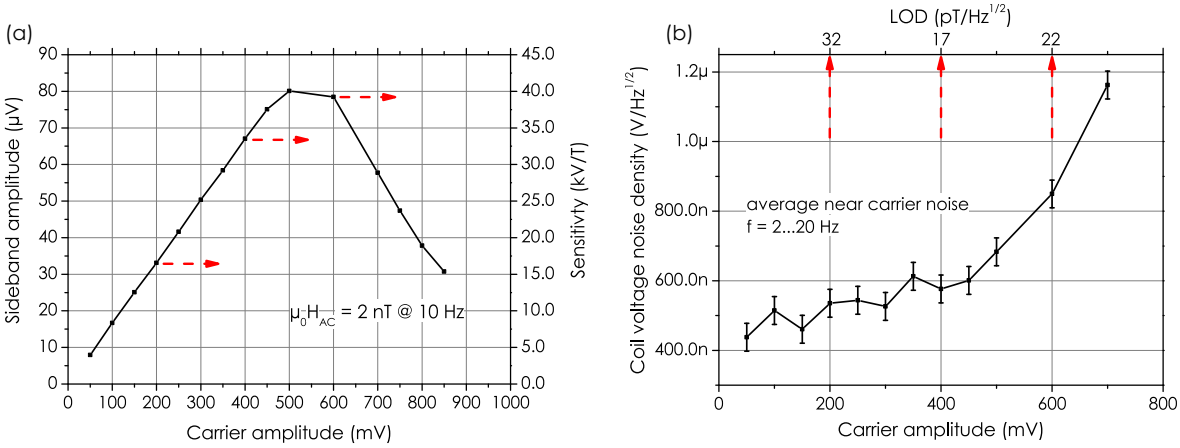

Figure 5.10: Magnetic field sensitivity for AC signals and near carrier noise evolution with carrier amplitude at an excitation frequency of 510.8 kHz. The red arrows indicated LOD values achieved for given carrier amplitudes, making 400 mV the best trade-off between signal and noise. (a) Sideband amplitude and resulting sensitivity for various excitation amplitudes. A linear increase up to a maximum at about 500 mV giving 80 µV or 40 $^{\mathrm{kV}}/_{\mathrm{T}}$ at 10 Hz. (b) Near carrier noise within 2 ... 20 Hz, indicating a strong noise increase above 400 mV. An optimum trade-off leads to lowest LOD of 17 $^{\mathrm{pT}}/\sqrt{\mathrm{Hz}}$ at 400 mV.

Figure 5.11 indicates constant sensitivity for magnetic test signals of frequencies between 33 ... 130 Hz at an amplitude of 2 nT.

Figure 5.12a shows the linearity towards the external magnetic field amplitude at a frequency of 10 Hz, a linear fit matches extremely well. At a magnetic field amplitude of 85 nT a second order mixing product at $f_{res} \pm 2f(H_{AC})$ emerges at an amplitude $730x$ lower than the fundamental signal amplitude, indicating slight distortion. Distortion is expected at large AC signal excursions leading to a local minor loops producing hysteresis, i.e. non-linearities in the magnetostrictive material.

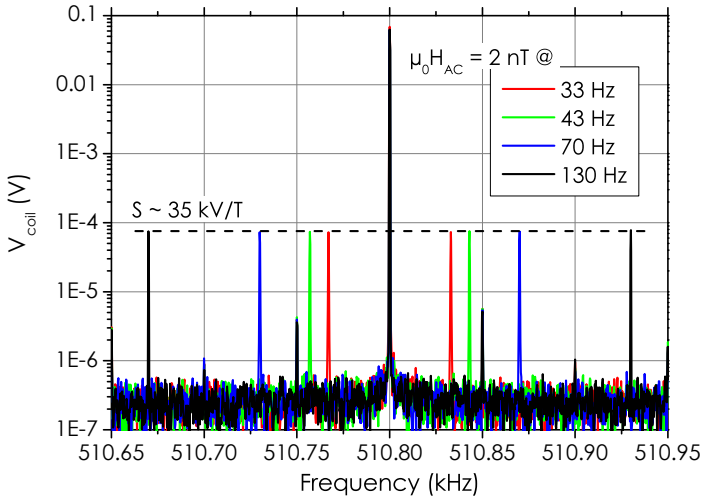

Figure 5.11: Amplitude spectra showing constant sensitivity of about 35 $^{\mathrm{kV}}/_{\mathrm{T}}$ for arbitrary magnetic test signals between 33 ... 130 Hz appearing symmetrically around the carrier at 510.8 kHz, demonstrating wide bandwidth. Spurious power line peaks at $f_{res} \pm 50$ Hz.

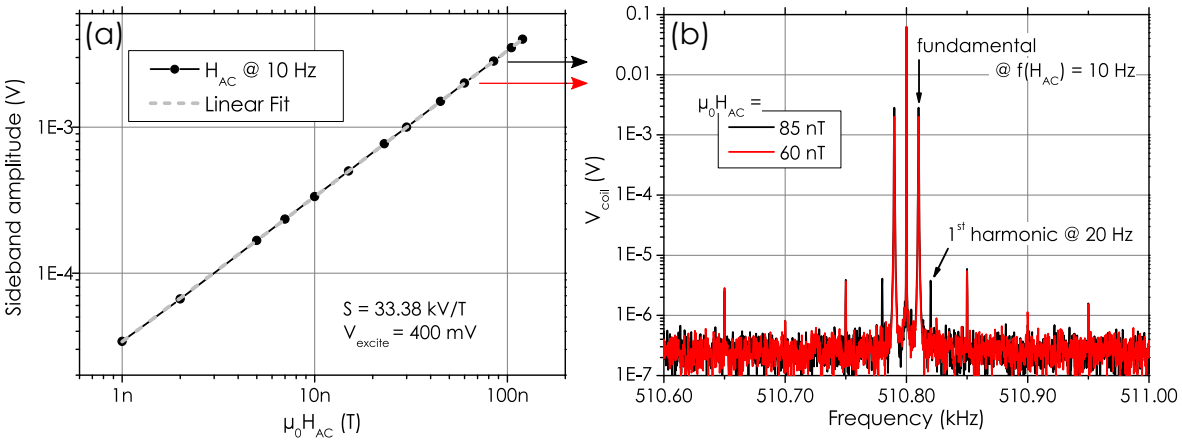

Figure 5.12: Linearity and distortion for an AC field of 10 Hz at various amplitudes. (a) strict linearity over more than two orders of magnitude from 1 ... 120 nT. The spectra for two amplitudes are given in (b) At a field amplitude of 85 nT a second order mixing product arises at the 1$^{\mathrm{st}}$ harmonic of the test signal at $f_{res} \pm 2f(H_{AC})$, which is not visible at lower amplitudes. Spurious peaks caused by power line coupling.

5.2 Human MCG Measurements

The measurement results presented in the previous section using APEB sensors were strongly encouraging as to dare a trial involving a healthy subjects' cardiac beat as test signal. A large magnetically shielded room (MSR) made by Vakuumschmelze (*Ak3B series*) is available at the Faculty of Engineering at Kiel University. The shielded volume is a cube of $2.4 \times 2.4 \times 3.0$ meters specified to be man accessible by a door and provide strong static magnetic field attenuation, leaving a residual field of less than 25 nT and even stronger attenuation towards AC magnetic fields, enabling magnetic measurements on patients. Magnetic reference signals were obtained at all times using commercial optically pumped magnetometers (OPM) by *QuSpin*. The employed OPMs are only operable at residual DC fields of < 50 nT, these are electronically compensated by using internal coils. After a static compensation procedure the device requires to remain stationary, its dynamic range is then limited to < 5 nT [Sha+18]. This constraint proved to be time consuming in practise as even trace DC magnetic fields from sources such as electrical connectors, screws or rivets on clothing required high compensation currents or entirely overloaded the built-in OPM compensation mechanism. The ferromagnetic FeCoSiB present on the ME composite fortunately required no special geometric clearances during the measurements. Further information about OPMs is to be found in section 1.1.3 on page 6.

For signal post processing purposes a two channel electrocardiography (ECG) signal was simultaneously recorded using a battery powered home built ECG amplifier simultaneously sampled by the lock-in amplifier. Figure 5.13a shows the healthy patient in the shielded facility, the OPM as well as ME sensor packages are in close vicinity to the chest at a distance as to allow breathing without making physical contact, on the order of two centimeters. The ECG electrodes are connected to the arms and the right leg. Figure 5.13b shows the ME sensor housing, hosting the resonator composite as well as its pre-amplifier in a copper cladded FR4 PCB box as to have the electrical shield on the inside, though the exterior being non-conductive and thus patient safe. Two 9 V supply batteries are enclosed in a separate electrically shielded box, as to avoid stray magnetic field emitted from the batteries. Calibration measurements using OPMs as well as an ME sensor within the MSR were performed to ensure operation at its working point and to verify the sensitivity of $9.3\,^{\mathrm{kV}}/_{\mathrm{T}}$ previously obtained and shown in figure 5.5 on page 101b. OPM measurements showed that the Z component, normal to the patients chest, gave the strongest amplitude at any of the tested positions. A point of strong Z amplitude on the patients chest was found and marked for subsequent ME measurements. The noise floor of the ME composite remained equal between the laboratory shielded Mu metal cylinder and the large MSR, this was verified and is

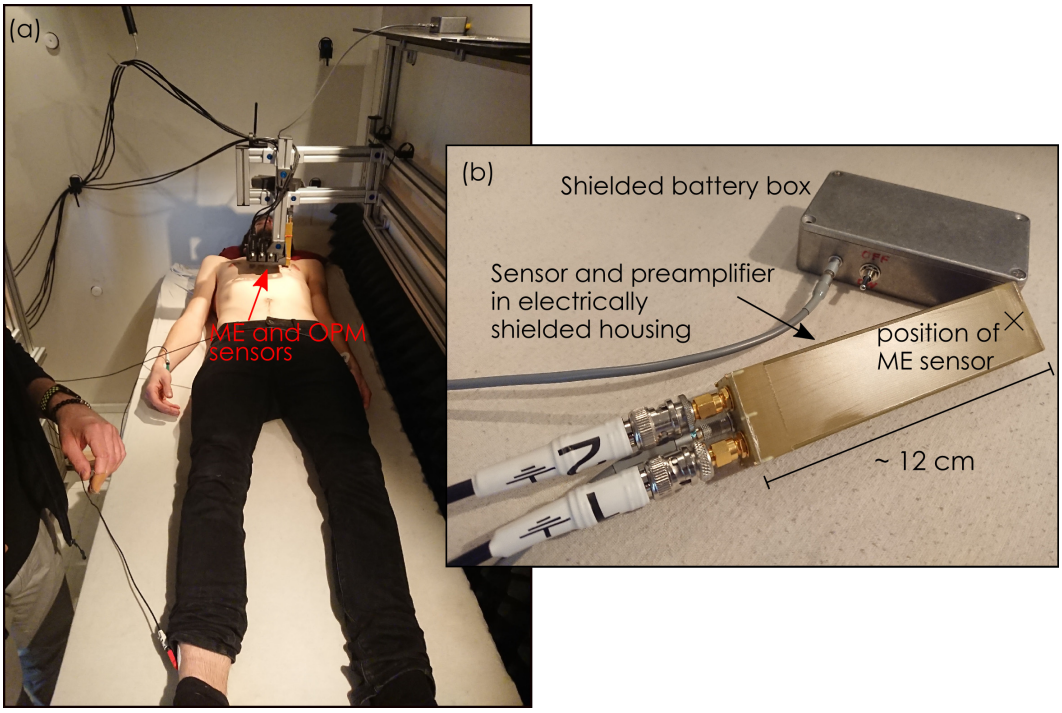

Figure 5.13: Magnetoelectric cardiac measurement setup involving a healthy subject and reference sensors in Kiel MSR. (a) Subject on patient bed, OPM as well as ME sensor mounted in close vicinity to the patients chest. ECG leads from arms and food as reference. (b) Sensor housing made from FR4 PCB material, inner copper cladding acts as electrical shielding, battery box separated by shielded cable to avoid static magnetic field emitted by batteries. Mechanical design and engineering by Dr.-Ing. Alexander Teplyuk.

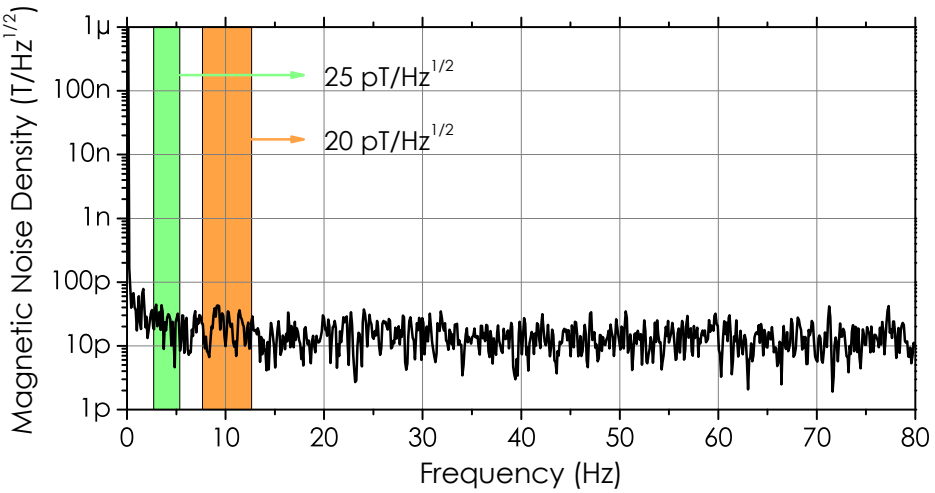

Figure 5.14: ME sensor magnetic noise floor within the MSR prior to cardiac measurements at an excitation amplitude of 400 mV. A LOD of 20 $^{\mathrm{pT}}/\sqrt{\mathrm{Hz}}$ at 10 Hz, slightly increasing to 25 $^{\mathrm{pT}}/\sqrt{\mathrm{Hz}}$ at 4 Hz was verified. Note absence of power line coupling.

displayed in figure 5.14, showing a magnetic noise density of $20\,^{\mathrm{pT}}/\sqrt{\mathrm{Hz}}$ in the vicinity of 10 Hz and about $25\,^{\mathrm{pT}}/\sqrt{\mathrm{Hz}}$ around 4 Hz within the large MSR. The ME sensor time

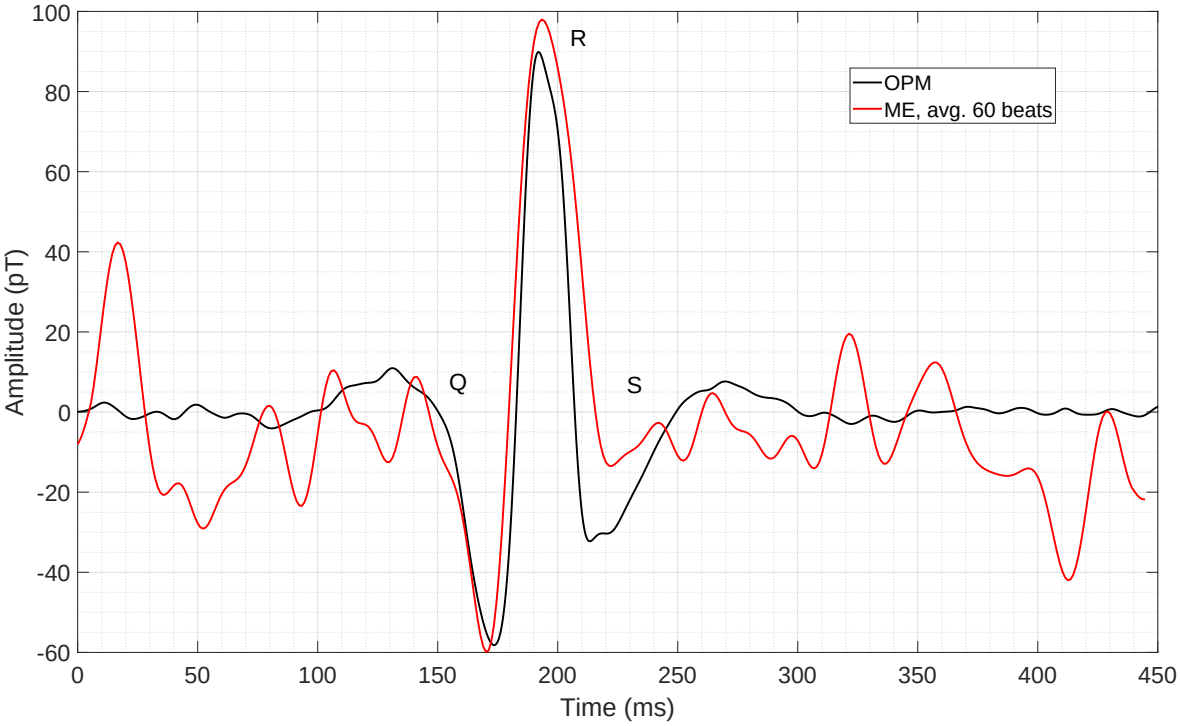

Figure 5.15: Human MCG recorded by OPM and ME sensor showing a QRS complex. The ME sensor signal was averaged over 60 beats, referenced by a synchronous ECG signal. OPM signal without averaging. The sensitivity of $S = 9.3\,^{\mathrm{kV}}/_{\mathrm{T}}$ was taken from prior measurements and matches that obtained by the reference OPM within 5 %. Signal processing performed by Eric Elzenheimer.

signal was averaged using the knowledge of the quasi periodic R-peaks determined by ECG, figure 5.15 displays the time signal overlay of ME as well as OPM sensor response for one QRS complex[2], the ME signal results from the unweighted average of 60 QRS sequences. A 4^{th} order highpass filter with a cutoff frequency of 1 Hz was applied without strong influence on the r-peak amplitude, in order to clean the signal from DC offset and drift. An upper limit was set by using a 4^{th} order lowpass filter with a passband below 125 Hz. The QRS sequences of ME as well as OPM were aligned in time, the amplitude was scaled according to the previously determined sensitivity of $9.3\,^{\mathrm{kV}}/_{\mathrm{T}}$, to obtain the magnetically measured QRS complex.

[2]Three waves stemming from heart muscle contraction, visually most prominent series of peaks in an ECG or MCG

Chapter 6

Summary & Outlook

Early studies using two piezoelectric layers of differing properties and one exchange biased magnetostrictive layer proved the principle of active electrical operation in section 2, removing the otherwise required magnetic driving coil. An already promising limit of detection of about $5\,^{\mathrm{nT}}/\sqrt{\mathrm{Hz}}$ at 2 Hz makes a good starting point for further research in this field of active magnetoelectric operation. This work has led to a patent filed under [Hay+20].

Ongoing studies, especially during a research stay at MIREA Moscow shed light from a different perspective, questioning the benefit of low frequency flexural resonances, which are associated with several drawbacks. If active operation of an ME composite is in place already, going to vastly higher frequency resonances such as the U2 mode readily improves detection limits and increases noise immunity. In section 3 the detection of about 1 nT at 200 mHz is demonstrated, which is of such low frequency that most biomagnetic signals of interest would lie above.

Additional research using strong in-house collaborations with the group of Prof. Dr.-Ing. Reinhard Knöchel (now led by Prof. Dr.-Ing. Michael Höft) as well as an external field trip visiting the IFW in Dresden, has brought deep insights to the microscopic, local picture of the converse magnetoelectric effect and the main differences between U1 and U2 mode, these findings are summarised in section 3.2.

In a long-standing collaboration with the group of Prof. Dr.-Ing. Jeffrey McCord, static as well as time-resolved MOKE was performed, presented in section 3.5. A simple semi-quantitative magnetoelastic model of piezoelectric stress acting on the magnetisation is proposed and is in good agreement with magneto-optical as well as induction measurements.

Going into deeper detail on the electronics side has led to the introduction of a resonantly tuned pickup coil, followed by a low-noise preamplifier buffering the signal,

resulting in a composite resonator exploiting U1 mode resonance. These novelties are filed for patent and pending at the time of writing. A leap towards actual biomagnetic application was achieved in section 4, exhibiting sensing performance of $70\,^{\mathrm{pT}}/\sqrt{\mathrm{Hz}}$ at 10 Hz and $210\,^{\mathrm{pT}}/\sqrt{\mathrm{Hz}}$ at DC, even using simple magnetic layer systems.

Combining the most promising high frequency U1 mode with advanced anti parallel exchange biased magnetostrictive multilayers enables unprecedented noise performance resulting in an LOD of $20\,^{\mathrm{pT}}/\sqrt{\mathrm{Hz}}$ at around 10 Hz. These laboratory scale results proved suitable for a demonstration recording of a human cardiac signal. This magnetically resolved QRS complex matching a reference signal was detected, using averaging through 60 beats, presented in section 5.2.

Future enhancements in order to accomplish realtime contact-less cardiac signal recording are within reach; both, in the area of analog and digital signal processing as well as on the materials engineering side. Finer tuning of the magnetic layer thicknesses in exchange biased multilayers will enable to optimally trade off signal for noise in order to achieve strongest converse magnetoelectric coupling associated to the lowest magnetic noise generation. Furthermore readout of the phase associated to the pickup coil signal, potentially reaching $73.8\,^{\mathrm{M}^\circ}/\mathrm{T}$ as presented in figure 5.6 may pose an additional channel for sensitive readout already at hand. Typically the highest phase sensitivity is found using a small but finite bias field for which a low-noise magnetic bias field source is necessary.

Adapted resonator geometries in order to best match the U mode resonance family may be advantageous, leading to a homogenisation of the piezoelectrically introduced stresses within the resonator, thus “activating” additional magnetic material.

Prospectively the localisation of electrically activated brain tissue in an application involving bipolar deep brain stimulation (DBS) may be feasible. The wideband artificial stimulation signal which is typically employed has a fundamental frequency on the order of 160 Hz and is strictly periodic, posing eased boundary conditions even for very small amplitudes of 1 pT.

6.1 Acknowledgements

My deepest gratitude to Prof. Dr.-Ing. Eckhard Quandt for giving me the fantastic opportunity to join and work in his group.
A group of excellent researchers holding broad expertise paired with a fleet of state of the art scientific tools and equipment always at hand. I very much enjoyed this nourishing ground supplying freedom and ability to pursue own pathways combined with guidance towards priorities.
I am grateful that he gave me the opportunity to be in place as a member of the DFG collaborative research centre (SFB1261); working within a multidisciplinary research environment offering broad competence throughout many disciplines, conveying a calming certainty that what is unknown among us, is at the actual verge of knowledge. Over a decade of excellent research has made Kiel University worldwide renowned in the field of thin-film composite magnetoelectrics.
Prof. Dr.-Ing. Reinhard Knöchel for steady support and always clear words.
Prof. Dr.-Ing. Ludger Klinkenbusch for giving me a lasting HiWi position in his group among a team of avid researchers and teachers. Dr.-Ing. Christian Möller and Dr.-Ing. Kai Körber gave me early insights into theoretical electrical engineering and brought me in touch with the Linux/Unix operating system.
Prof. Dr.-Ing. Helmut Föll for bringing technology and application from the early days into his lecture, painting the full picture from inter-atomic potential wells right up to marketing of a product, by this creating strong motivation in studenthood.
Dr.-Ing. André Piorra, Dr.-Ing. Enno Lage gave positive support and great guidance, especially in the beginning of my studies.
Ultima ratio, whenever I was deep down the rabbit hole, Dr.-Ing. Claas Theede always came up with an elegant solution and additional in-depth coverage.
Dr. rer. nat. Dirk Meyners, Dr.-Ing. Ali Tavassolizadeh and Eric Woltermann for giving me the opportunity of building and programming the first measurement setup of my life, which was of great use throughout my masters thesis and beyond.
Dr.-Ing. Till Jurgeleit, Dr.-Ing. Erdem Yarar, Volker Röbisch, Dr.-Ing. Christoph Chluba the old squad for an infinite amount of fruitful discussions. Dr. rer. nat. Christiane Zamponi for discussions concerning science on a broad perspective. Viktor Schell as my best master student, produced a host of only the softest magnetostrictive cantilever sensors, holding the line in Kiel while I was visiting Moscow.
Dr.-Ing. Onur Urs, Dr.-Ing. Matic Klug and Prof. Dr.-Ing. Jeffrey McCord introduced me into the beauty of magneto-optic imaging during a long-standing collaboration concerning magnetic imaging experiments and many associated discussions.
Dr.-Ing. Iulian Teliban, Dr.-Ing. Phillip Durdaut essentially taught me all I know about

practical electrical engineering.
Dr.-Ing. Alexander Teplyuk the Ukrainian precision engineer, creating great, solid hardware.
Dr.-Ing. Jens Reermann, Eric Elzenheimer of DSS group for performing magic on signals.
Dr.-Ing. Steffen Chemnitz enabled an exciting HiWi time with Fraunhofer ISIT.
Cooperation in the warmest possible vibe persisted within the collaborative research environment during PAK902 grants and its successor Sonderforschungsbereich 1261 (SFB1261). Our project manager, Dr.-Ing. Julia Jedtberg (former Reverey) for steering great project trips and activities throughout many years.
Prof. Yuri K. Fetisov, Dr. Dmitry Burdin, Dr. Fedor Fedulov at MIREA for a very productive and unforgettable research stay in beautiful Moscow.
Dr.-Ing. Till Jurgeleit, Dr.-Ing. Erdem Yarar, Lea K. Jessen for a fantastic time in a chaotic, yet brilliant office.
Special thanks to Dr.-Ing. Christine Kirchhoff, Lars Bumke, Maike Wegner, Anne Kittmann, Dr.-Ing. Sebastian Toxwaerd and Lars Thormählen.
Wolfgang Taute, Berndt Neumann for (non-)technical discussions and better perspectives on various hardware projects.
Adriatique of Zürich and Extrawelt of Hamburg for constantly driving me through life.
My girlfriend, quasi-wife Dr.-Ing. Iris for endless patience and energy, always in action.
My Parents Susanne and Denis and my brother Barry as well as a colourful bunch of Friends.

6.2 Full List of Own Publications

- Sabrina M. Curtis, Niklas Wolff, Duygu Dengiz, Hanna Lewitz, Justin Jetter, Lars Bumke, **Patrick Hayes**, Erdem Yarar, Lars Thormählen, Lorenz Kienle, Dirk Meyners, and Eckhard Quandt. "Integration of AlN piezoelectric thin films on ultralow fatigue TiNiCu shape memory alloys". In: *Journal of Materials Research* 35.10 (**2020**), pp. 1298–1306. ISSN: 0884-2914

- Daniel Laumann, **Patrick Hayes**, Carolin Enzingmüller, Ilka Parchmann, and Eckhard Quandt. "Magnetostriction measurements with a low-cost magnetostrictive cantilever beam". In: *American Journal of Physics* 88.6 (**2020**), pp. 448–455. ISSN: 0002-9505

- **Patrick Hayes**, Matic Jovičević Klug, Sebastian Toxværd, Phillip Durdaut, Viktor Schell, Alexander Teplyuk, Dmitrii Burdin, Andreas Winkler, Robert Weser,

Yuri K. Fetisov, Michael Höft, Reinhard Knöchel, Jeffrey McCord, and Eckhard Quandt. "Converse Magnetoelectric Composite Resonator for Sensing Small Magnetic Fields". In: *Scientific reports* 9.1 (**2019**), p. 16355

▷ Cheng Tu, Zhao-Qiang Chu, Benjamin Spetzler, **Patrick Hayes**, Cun-Zheng Dong, Xian-Feng Liang, Huai-Hao Chen, Yi-Fan He, Yu-Yi Wei, Ivan Lisenkov, Hwaider Lin, Yuan-Hua Lin, Jeffrey McCord, Franz Faupel, Eckhard Quandt, and Nian-Xiang Sun. "Mechanical-Resonance-Enhanced Thin-Film Magnetoelectric Heterostructures for Magnetometers, Mechanical Antennas, Tunable RF Inductors, and Filters". In: *Materials* 12.14 (**2019**)

▷ Erdem Yarar, Dirk Meyners, Eckhard Quandt, Simon Fichtner, **Patrick Hayes**, André Piorra, Tim Reimer, Thomas Lisec, Peter Frank, Bernhard Wagner, and Fabian Lofink. "MEMS-Based AlScN Resonating Energy Harvester With Solidified Powder Magnet". In: *Journal of Microelectromechanical Systems* 28.6 (**2019**), pp. 1019–1031. ISSN: 1057-7157

▷ **Patrick Hayes**, Viktor Schell, Sebastian Salzer, Dmitrii Burdin, Erdem Yarar, André Piorra, Reinhard Knöchel, Yuri K. Fetisov, and Eckhard Quandt. "Electrically Modulated Magnetoelectric AlN/FeCoSiB Film Composites for DC Magnetic Field Sensing". In: *Journal of Physics D: Applied Physics* 51.35 (**2018**), p. 354002. ISSN: 0022-3727

▷ Yuri K. Fetisov, Dmitri A. Burdin, Nikolai A. Ekonomov, Leonid Y. Fetisov, Alexey A. Berzin, **Patrick Hayes**, and Eckhard Quandt. "Bistability in a multiferroic composite resonator". In: *Applied Physics Letters* 113.2 (**2018**), p. 022903. ISSN: 0003-6951

▷ Phillip Durdaut, Sebastian Salzer, Jens Reermann, Volker Robisch, **Patrick Hayes**, André Piorra, Dirk Meyners, Eckhard Quandt, Gerhard Schmidt, Reinhard Knöchel, and Michael Höft. "Thermal-Mechanical Noise in Resonant Thin-Film Magnetoelectric Sensors". In: *IEEE Sensors Journal* 17.8 (**2017**), pp. 2338–2348

▷ **Patrick Hayes**, Sebastian Salzer, Jens Reermann, Erdem Yarar, Volker Röbisch, André Piorra, D. Meyners, Michael Höft, Reinhard Knöchel, Gerhard Schmidt, and Eckhard Quandt. "Electrically modulated magnetoelectric sensors". In: *Applied Physics Letters* 108.18 (**2016**), p. 182902. ISSN: 0003-6951

▷ Necdet Onur Urs, Babak Mozooni, Piotr Mazalski, Mikhail Kustov, **Patrick Hayes**, Shayan Deldar, Eckhard Quandt, and Jeffrey McCord. "Advanced

magneto-optical microscopy: Imaging from picoseconds to centimeters - imaging spin waves and temperature distributions (invited)". In: *AIP Advances* 6.5 (**2016**), p. 055605. ISSN: 2158-3226

- ▷ Sebastian Salzer, Michael Höft, Reinhard Knöchel, **Patrick Hayes**, Erdem Yarar, André Piorra, and Eckhard Quandt. "Comparison of Frequency Conversion Techniques for Magnetoelectric Sensors". In: *Procedia Engineering* 120 (**2015**), pp. 940–943. ISSN: 18777058

- ▷ Ali Tavassolizadeh, **Patrick Hayes**, Karsten Rott, Günter Reiss, Eckhard Quandt, and Dirk Meyners. "Highly strain-sensitive magnetostrictive tunnel magnetoresistance junctions". In: *Journal of Magnetism and Magnetic Materials* 384 (**2015**), pp. 308–313. ISSN: 03048853

Granted Patents

- ▷ **Patrick Hayes**, André Piorra, Reinhard Knöchel, and Eckhard Quandt. "Magnetoelectric magnetic field measurement with frequency conversion". US10613159B2 / EP15170985. **2020**

Bibliography

[Ann+17] Venkateswarlu Annapureddy et al. "A pT/$\sqrt{}$Hz sensitivity ac magnetic field sensor based on magnetoelectric composites using low-loss piezoelectric single crystals". In: *Sensors and Actuators A: Physical* 260 (2017), pp. 206–211. ISSN: 09244247.

[AP12] Rashed Adnan Islam and Shashank Priya. "Progress in Dual (Piezoelectric-Magnetostrictive) Phase Magnetoelectric Sintered Composites". In: *Advances in Condensed Matter Physics* 2012.9 (2012), pp. 1–29. ISSN: 1687-8108.

[Ber+14] Bernhard Bergmair et al. "Fully coupled, dynamic model of a magnetostrictive amorphous ribbon and its validation". In: *Journal of Applied Physics* 115.2 (2014), p. 023905. ISSN: 0021-8979.

[BO89] R. Boll and K. J. Overshott. *Sensors*. Wiley, 1989. ISBN: 9783527267712.

[Bre73] Sheldon Breiner. *Applications manual for portable magnetometers*. Vol. 395. Geometrics Sunnyvale, California, 1973.

[BS19] Mattia Butta and Byron P. Schutte. "Low-Noise Orthogonal Fluxgate Using Flipped Current Joule Annealing". In: *IEEE Transactions on Magnetics* 55.7 (2019), pp. 1–6. ISSN: 0018-9464.

[BS70] Heinz Bittel and Leo Storm. *Rauschen*. Berlin, Heidelberg: Springer Berlin Heidelberg, 1970. ISBN: 978-3-642-49241-9.

[Bur+11] Alexandre Bur et al. "Giant electric field induced reversible and permanent magnetization reorientation on magnetoelectric Ni heterostructure". In: *Applied Physics Letters* 98.1 (2011), p. 012504. ISSN: 0003-6951.

[But03] Dwain K. Butler. "Implications of magnetic backgrounds for unexploded ordnance detection". In: *Journal of Applied Geophysics* 54.1 (2003), pp. 111–125. ISSN: 0926-9851.

[Car+14] S. Cardoso et al. "Magnetic tunnel junction sensors with pTesla sensitivity". In: *Microsystem Technologies* 20.4-5 (2014), pp. 793–802. ISSN: 0946-7076.

[CG09] Bernard Dennis Cullity and Chad D. Graham. *Introduction to magnetic materials*. 2nd ed. Hoboken, N.J: IEEE/Wiley, 2009. ISBN: 9780471477419.

[Chi+97] Laurent Chiesi et al. "Chopping of a weak magnetic field by a saturable magnetic shield". In: *Sensors and Actuators A: Physical* 60.1 (1997), pp. 5–9. ISSN: 09244247.

[Chu+17a] Zhaoqiang Chu et al. "A magnetoelectric flux gate: New approach for weak DC magnetic field detection". In: *Scientific reports* 7.1 (2017), p. 8592.

[Chu+17b] Zhaoqiang Chu et al. "Enhanced Resonance Magnetoelectric Coupling in (1-1) Connectivity Composites". In: *Advanced materials (Deerfield Beach, Fla.)* 29.19 (2017).

[Chu+19] Zhaoqiang Chu et al. "Enhanced low-frequency magnetic field sensitivity in magnetoelectric composite with amplitude modulation method". In: *Applied Physics Letters* 114.13 (2019), p. 132901. ISSN: 0003-6951.

[Coh68] David Cohen. "Magnetoencephalography: Evidence of Magnetic Fields Produced by Alpha-Rhythm Currents". In: *Science* 161.3843 (1968), pp. 784–786. ISSN: 1095-9203.

[CP11] Kyung-Hoon Cho and Shashank Priya. "Direct and converse effect in magnetoelectric laminate composites". In: *Applied Physics Letters* 98.23 (2011), p. 232904. ISSN: 0003-6951.

[Das+09] J. Das et al. "Enhancement in the field sensitivity of magnetoelectric laminate heterostructures". In: *Applied Physics Letters* 95.9 (2009), p. 092501. ISSN: 0003-6951.

[Dea+96] J. Deak et al. "A low–noise single–domain fluxgate sensor". In: *Applied Physics Letters* 69.8 (1996), pp. 1157–1159. ISSN: 0003-6951.

[Don+06a] Shuxiang Dong et al. "Near-ideal magnetoelectricity in high-permeability magnetostrictive/piezofiber laminates with a (2-1) connectivity". In: *Applied Physics Letters* 89.25 (2006), p. 252904. ISSN: 0003-6951.

[Don+06b] Shuxiang Dong et al. "Small dc magnetic field response of magnetoelectric laminate composites". In: *Applied Physics Letters* 88.8 (2006), p. 082907. ISSN: 0003-6951.

[Don+20] Cunzheng Dong et al. "A Portable Very Low Frequency (VLF) Communication System Based on Acoustically Actuated Magnetoelectric Antennas". In: *IEEE Antennas and Wireless Propagation Letters* 19.3 (2020), pp. 398–402. ISSN: 1536-1225.

[DP16] Carole Donada and Yannick Perez. “Editorial: Electromobility at the crossroads”. In: *International Journal of Automotive Technology and Management* 16 (2016).

[Dru95] D. Drung. “The PTB 83-SQUID system for biomagnetic applications in a clinic”. In: *IEEE Transactions on Appiled Superconductivity* 5.2 (1995), pp. 2112–2117. ISSN: 10518223.

[Dur+17] Phillip Durdaut et al. “Improved Magnetic Frequency Conversion Approach for Magnetoelectric Sensors”. In: *IEEE Sensors Letters* 1.3 (2017), pp. 1–4. ISSN: 2475-1472.

[EP01] M. Es-Souni and A. Piorra. “On the crystallization kinetics of solution deposited PZT thin films”. In: *Materials Research Bulletin* 36.15 (2001), pp. 2563–2575. ISSN: 00255408.

[Fan+15] Cong Fang et al. “Significant reduction of equivalent magnetic noise by in-plane series connection in magnetoelectric Metglas/Mn-doped Pb(Mg 1/3 Nb 2/3)O 3 -PbTiO 3 laminate composites”. In: *Journal of Physics D: Applied Physics* 48.46 (2015), p. 465002. ISSN: 0022-3727.

[Fet+14] Yuri K. Fetisov et al. “High-Sensitivity Wideband Magnetic Field Sensor Using Nonlinear Resonance Magnetoelectric Effect”. In: *IEEE Sensors Journal* 14.7 (2014), pp. 2252–2256.

[Fet+18] Yuri K. Fetisov et al. “Bistability in a multiferroic composite resonator”. In: *Applied Physics Letters* 113.2 (2018), p. 022903. ISSN: 0003-6951.

[Fle08] William J. Fleming. “New Automotive Sensors—A Review”. In: *IEEE Sensors Journal* 8.11 (2008), pp. 1900–1921.

[FPS07] Y. K. Fetisov, V. M. Petrov, and G. Srinivasan. “Inverse magnetoelectric effects in a ferromagnetic–piezoelectric layered structure”. In: *Journal of Materials Research* 22.08 (2007), pp. 2074–2080. ISSN: 0884-2914.

[Fri+19] Ron-Marco Friedrich et al. “Magnetic particle mapping using magnetoelectric sensors as an imaging modality”. In: *Scientific Reports* 9.1 (2019), pp. 1–11. ISSN: 2045-2322.

[GB02] L. Gammaitoni and A. R. Bulsara. “Noise activated nonlinear dynamic sensors”. In: *Physical review letters* 88.23 (2002), p. 230601. ISSN: 0031-9007.

[GDS08] R. Grössinger, Giap V. Duong, and R. Sato-Turtelli. “The physics of magnetoelectric composites”. In: *Journal of Magnetism and Magnetic Materials* 320.14 (2008), pp. 1972–1977. ISSN: 03048853.

[GHM16] Asaf Grosz, Michael J. Haji-Sheikh, and Subhas C. Mukhopadhyay. *High Sensitivity Magnetometers*. Vol. v.19. Smart Sensors, Measurement and Instrumentation. Cham: Springer International Publishing, 2016. ISBN: 9783319340685.

[Gil+11] S. M. Gillette et al. "Improved Sensitivity and Noise in Magneto-Electric Magnetic Field Sensors by Use of Modulated AC Magnetostriction". In: *IEEE Magnetics Letters* 2 (2011), p. 2500104.

[Gri+02] Craig A. Grimes et al. "Wireless Magnetoelastic Resonance Sensors: A Critical Review". In: *Sensors* 2.7 (2002), pp. 294–313.

[Gue+08] A. Guedes et al. "Hybrid magnetoresistive/microelectromechanical devices for static field modulation and sensor 1/f noise cancellation". In: *Journal of Applied Physics* 103.7 (2008), 07E924. ISSN: 0021-8979.

[Hay+18] Patrick Hayes et al. "Electrically modulated magnetoelectric AlN/FeCoSiB film composites for DC magnetic field sensing". In: *Journal of Physics D: Applied Physics* 51.35 (2018), p. 354002. ISSN: 0022-3727.

[Hay+19] Patrick Hayes et al. "Converse Magnetoelectric Composite Resonator for Sensing Small Magnetic Fields". In: *Scientific reports* 9.1 (2019), p. 16355.

[Hay+20] P. Hayes et al. "Magnetoelectric magnetic field measurement with frequency conversion". US10613159B2 / EP15170985. 2020.

[Hir+01] M. Hirota et al. "Magnetic detection of a surface ship by an airborne LTS SQUID MAD". In: *IEEE Transactions on Appiled Superconductivity* 11.1 (2001), pp. 884–887. ISSN: 10518223.

[HKG19] Evangelos Hristoforou, Aphrodite Ktena, and Shengkai Gong. "Magnetic Sensors: Taxonomy, Applications, and New Trends". In: *IEEE Transactions on Magnetics* 55.7 (2019), pp. 1–14. ISSN: 0018-9464.

[Hoc+13] Joshua L. Hockel et al. "A method to control magnetism in individual strain-mediated magnetoelectric islands". In: *Applied Physics Letters* 103.23 (2013), p. 232905. ISSN: 0003-6951.

[Hol08] John J. Holmes. "Reduction of a Ship's Magnetic Field Signatures". In: *Synthesis Lectures on Computational Electromagnetics* 3.1 (2008), pp. 1–68. ISSN: 1932-1252.

[Hon02] Yoshinobu Honkura. "Development of amorphous wire type MI sensors for automobile use". In: *Journal of Magnetism and Magnetic Materials* 249.1-2 (2002), pp. 375–381. ISSN: 03048853.

[HQK16] Patrick Hayes, Eckhard Quandt, and Reinhard Knöchel. "Magnetoelektrische Magnetfeldmessung mit Frequenzumsetzung". WO/2016/198042. 2016.

[HWC11] Joshua L. Hockel, Tao Wu, and Gregory P. Carman. "Voltage bias influence on the converse magnetoelectric effect of PZT/terfenol-D/PZT laminates". In: *Journal of Applied Physics* 109.6 (2011), p. 064106. ISSN: 0021-8979.

[Jah+12] Robert Jahns et al. "Sensitivity enhancement of magnetoelectric sensors through frequency-conversion". In: *Sensors and Actuators A: Physical* 183 (2012), pp. 16–21. ISSN: 09244247.

[Jah13] Robert Jahns. *Untersuchung und Optimierung von Empfindlichkeit und Rauschverhalten magnetoelektrischer Sensoren*. 2013.

[Jan+19] Michal Janosek et al. "1-pT noise fluxgate magnetometer for geomagnetic measurements and unshielded magnetocardiography". In: *IEEE Transactions on Instrumentation and Measurement* (2019), p. 1. ISSN: 0018-9456.

[Jov+19] Matic Jovičević Klug et al. "Antiparallel exchange biased multilayers for low magnetic noise magnetic field sensors". In: *Applied Physics Letters* 114.19 (2019), p. 192410. ISSN: 0003-6951.

[Jov19] Matic Jovičević Klug. *Methodological Reduction of Magnetically Induced Noise in Magnetic Multilayers for Sensor Applications*. 2019.

[KDG99] R. H. Koch, J. G. Deak, and G. Grinstein. "Fundamental limits to magnetic-field sensitivity of flux-gate magnetic-field sensors". In: *Applied Physics Letters* 75.24 (1999), pp. 3862–3864. ISSN: 0003-6951.

[Kim+10] Ju-Hyun Kim et al. "Large converse magnetoelectric coupling effect at room temperature in CoPd/PMN-PT (001) heterostructure". In: *Applied Physics Letters* 97.25 (2010), p. 252508. ISSN: 0003-6951.

[Kir+13] Christine Kirchhof et al. "Giant magnetoelectric effect in vacuum". In: *Applied Physics Letters* 102.23 (2013), p. 232905. ISSN: 0003-6951.

[Kit+18] Anne Kittmann et al. "Wide Band Low Noise Love Wave Magnetic Field Sensor System". In: *Scientific reports* 8.1 (2018), p. 278.

[KL05] Sakhrat Khizroev and Dmitri Litvinov. *Perpendicular Magnetic Recording*. Dordrecht: Springer Science + Business Media Inc, 2005. ISBN: 9781402026621.

[KMD08] Luděk Kraus, Michal Malátek, and Miroslav Dvořák. "Magnetic field sensor based on asymmetric inverse Wiedemann effect". In: *Sensors and Actuators A: Physical* 142.2 (2008), pp. 468–473. ISSN: 09244247.

[KST14] Svenja Knappe, Tilmann Sander, and Lutz Trahms. "Optically-Pumped Magnetometers for MEG". In: *Magnetoencephalography*. Ed. by Selma Supek and Cheryl J. Aine. Series in Bioengineering. Berlin, Heidelberg and s.l.: Springer Berlin Heidelberg, 2014, pp. 993–999. ISBN: 978-3-642-33045-2.

[Kul+14] A. Kulkarni et al. "Giant magnetoelectric effect at low frequencies in polymer-based thin film composites". In: *Applied Physics Letters* 104.2 (2014), p. 022904. ISSN: 0003-6951.

[Lag+12] Enno Lage et al. "Exchange biasing of magnetoelectric composites". In: *Nature materials* 11.6 (2012), pp. 523–529. ISSN: 1476-1122.

[LE06] J. Lenz and S. Edelstein. "Magnetic sensors and their applications". In: *IEEE Sensors Journal* 6.3 (2006), pp. 631–649.

[Li+13] Menghui Li et al. "Giant magnetoelectric effect in self-biased laminates under zero magnetic field". In: *Applied Physics Letters* 102.8 (2013), p. 082404. ISSN: 0003-6951.

[Liv82] J. D. Livingston. "Magnetomechanical properties of amorphous metals". In: *Physica Status Solidi (a)* 70.2 (1982), pp. 591–596. ISSN: 00318965.

[LML82] J. D. Livingston, W. G. Morris, and F. E. Luborsky. "Domain studies on amorphous ribbons with transverse or oblique magnetic anisotropy". In: *Journal of Applied Physics* 53.11 (1982), pp. 7837–7839. ISSN: 0021-8979.

[LS11] G. Lawes and G. Srinivasan. "Introduction to magnetoelectric coupling and multiferroic films". In: *Journal of Physics D: Applied Physics* 44.24 (2011), p. 243001. ISSN: 0022-3727.

[MAD87] M. D. Mermelstein, C. Askins, and A. Dandridge. "Stress-relieved magnetoelastic amorphous metal DC magnetometer". In: *Electronics Letters* 23.6 (1987), p. 280. ISSN: 00135194.

[Mar+13] S. Marauska et al. "Highly sensitive wafer-level packaged MEMS magnetic field sensor based on magnetoelectric composites". In: *Sensors and Actuators A: Physical* 189 (2013), pp. 321–327. ISSN: 09244247.

[Mer92] M. D. Mermelstein. "A magnetoelastic metallic glass low-frequency magnetometer". In: *IEEE Transactions on Magnetics* 28.1 (1992), pp. 36–56. ISSN: 0018-9464.

[MH08] A. J. Moulson and J. M. Herbert. *Electroceramics: Materials, properties, applications*. 2. ed., reprinted. Chichester: Wiley, 2008. ISBN: 9780471497479.

[MK10] Michal Malátek and Luděk Kraus. "Off-diagonal GMI sensor with stress-annealed amorphous ribbon". In: *Sensors and Actuators A: Physical* 164.1-2 (2010), pp. 41–45. ISSN: 09244247.

[MP95] Jaakko Malmivuo and Robert Plonsey. *Bioelectromagnetism Principles and Applications of Bioelectric and Biomagnetic Fields*. Oxford University Press, 1995. ISBN: 9780195058239.

[Mur97] Paul Muralt. "Piezoelectric thin films for mems". In: *Integrated Ferroelectrics* 17.1-4 (1997), pp. 297–307. ISSN: 1058-4587.

[Nai+13] Swapna S. Nair et al. "Lead free heterogeneous multilayers with giant magneto electric coupling for microelectronics/microelectromechanical systems applications". In: *Journal of Applied Physics* 114.6 (2013), p. 064309. ISSN: 0021-8979.

[Nan+13] Tianxiang Nan et al. "Self-biased 215 MHz magnetoelectric NEMS resonator for ultra-sensitive DC magnetic field detection". In: *Scientific reports* 3 (2013), p. 1985.

[Nan+17] Tianxiang Nan et al. "Acoustically actuated ultra-compact NEMS magnetoelectric antennas". In: *Nature Communications* 8.1 (2017), pp. 1–8. ISSN: 2041-1723.

[NM92] Y. Nakaya and H. Mori. "Magnetocardiography". In: *Clinical Physics and Physiological Measurement* 13.3 (1992), p. 191. ISSN: 0143-0815.

[NS99] J. Nogués and Ivan K. Schuller. "Exchange bias". In: *Journal of Magnetism and Magnetic Materials* 192.2 (1999), pp. 203–232. ISSN: 03048853.

[Ou-+18] Jun Ou-Yang et al. "Magnetoelectric laminate composites: An overview of methods for improving the DC and low-frequency response". In: *Journal of Physics D: Applied Physics* 51.32 (2018), p. 324005. ISSN: 0022-3727.

[PCP00] R. J. Prance, T. D. Clark, and H. Prance. "Ultra low noise induction magnetometer for variable temperature operation". In: *Sensors and Actuators A: Physical* 85.1-3 (2000), pp. 361–364. ISSN: 09244247.

[Per+14] Charith Perera et al. "A Survey on Internet of Things From Industrial Market Perspective". In: *IEEE Access* 2 (2014), pp. 1660–1679. ISSN: 2169-3536.

[Pet+11] Jonathan R. Petrie et al. “Enhanced sensitivity of magnetoelectric sensors by tuning the resonant frequency”. In: *Applied Physics Letters* 99.4 (2011), p. 043504. ISSN: 0003-6951.

[PFB96] R. S. Popovic, J. A. Flanagan, and P. A. Besse. “The future of magnetic sensors”. In: *Sensors and Actuators A: Physical* 56.1 (1996), pp. 39–55. ISSN: 09244247.

[Pfe+20] Christoph Pfeiffer et al. “A 7-Channel High-Tc SQUID-Based On-Scalp MEG System”. In: *IEEE transactions on bio-medical engineering* 67.5 (2020), pp. 1483–1489. ISSN: 0018-9294.

[PG09] Eugene Paperno and Asaf Grosz. “A miniature and ultralow power search coil optimized for a 20 mHz to 2 kHz frequency range”. In: *Journal of Applied Physics* 105.7 (2009), 07E708. ISSN: 0021-8979.

[Pio+13] André Piorra et al. “Magnetoelectric thin film composites with interdigital electrodes”. In: *Applied Physics Letters* 103.3 (2013), p. 032902. ISSN: 0003-6951.

[Pri+07] Shashank Priya et al. “Recent advancements in magnetoelectric particulate and laminate composites”. In: *Journal of Electroceramics* 19.1 (2007), pp. 149–166. ISSN: 1385-3449.

[Pri79] F. Primdahl. “The fluxgate magnetometer”. In: *Journal of Physics E: Scientific Instruments* 12.4 (1979), p. 241. ISSN: 0022-3735.

[Ree+15] Jens Reermann et al. “Adaptive Acoustic Noise Cancellation for Magnetoelectric Sensors”. In: *IEEE Sensors Journal* 15.10 (2015), pp. 5804–5812.

[Rip00] Pavel Ripka. “Magnetic Sensors and Magnetometers”. In: *Measurement Science and Technology* 13.4 (2000), p. 645. ISSN: 0957-0233.

[Rip03] Pavel Ripka. “Advances in fluxgate sensors”. In: *Sensors and Actuators A: Physical* 106.1-3 (2003), pp. 8–14. ISSN: 09244247.

[Röb+15] Volker Röbisch et al. “Exchange biased magnetoelectric composites for magnetic field sensor application by frequency conversion”. In: *Journal of Applied Physics* 117.17 (2015), 17B513. ISSN: 0021-8979.

[Rou+08] A. Roux et al. “The Search Coil Magnetometer for THEMIS”. In: *Space Science Reviews* 141.1-4 (2008), pp. 265–275. ISSN: 0038-6308.

[Rup+17] Michael G. Ruppert et al. “A review of demodulation techniques for amplitude-modulation atomic force microscopy”. In: *Beilstein journal of nanotechnology* 8 (2017), pp. 1407–1426. ISSN: 2190-4286.

[Sal18] Sebastian D. Salzer. *Readout Methods for Magnetoelectric Sensors: Auslesemethoden für magnetoelektrische Sensoren*. 2018.

[Sas02] I. Sasada. "Orthogonal fluxgate mechanism operated with dc biased excitation". In: *Journal of Applied Physics* 91.10 (2002), p. 7789. ISSN: 0021-8979.

[Sch+20] Viktor Schell et al. "Magnetic anisotropy controlled FeCoSiB thin films for surface acoustic wave magnetic field sensors". In: *Applied Physics Letters* 116.7 (2020), p. 073503. ISSN: 0003-6951.

[Sha+18] Vishal Shah et al. "Fully integrated, standalone zero field optically pumped magnetometer for biomagnetism". In: *Steep Dispersion Engineering and Opto-Atomic Precision Metrology XI*. Ed. by Selim M. Shahriar and Jacob Scheuer. SPIE, 2018, p. 51. ISBN: 9781510615816.

[She+14] Ying Shen et al. "High non-linear magnetoelectric coefficient in Metglas/PMN-PT laminate composites under zero direct current magnetic bias". In: *Journal of Applied Physics* 115.9 (2014), p. 094102. ISSN: 0021-8979.

[Sre+12] G. Sreenivasulu et al. "Magnetoelectric interactions in layered composites of piezoelectric quartz and magnetostrictive alloys". In: *Physical Review B* 86.21 (2012). ISSN: 0163-1829.

[Sri+01] G. Srinivasan et al. "Magnetoelectric bilayer and multilayer structures of magnetostrictive and piezoelectric oxides". In: *Physical Review B* 64.21 (2001), p. 214408. ISSN: 0163-1829.

[Sri+05] G. Srinivasan et al. "Magnetoelectric interactions in bilayers of yttrium iron garnet and lead magnesium niobate-lead titanate: Evidence for strong coupling in single crystals and epitaxial films". In: *Applied Physics Letters* 86.22 (2005), p. 222506. ISSN: 0003-6951.

[SSP14] G. Srinivasan, N. Sun, and S. Priya. *Composite magnetoelectrics: Materials, structures, and applications*. Woodhead Publishing Series in Electronic and Optical Materials. Oxford: Woodhead Publishing, 2014. ISBN: 9781782422549.

[Stu+05] Nathan A. Stutzke et al. "Low-frequency noise measurements on commercial magnetoresistive magnetic field sensors". In: *Journal of Applied Physics* 97.10 (2005), 10Q107. ISSN: 0021-8979.

[Tav+15] Ali Tavassolizadeh et al. "Highly strain-sensitive magnetostrictive tunnel magnetoresistance junctions". In: *Journal of Magnetism and Magnetic Materials* 384 (2015), pp. 308–313. ISSN: 03048853.

[TM04] S. Trolier-McKinstry and P. Muralt. "Thin Film Piezoelectrics for MEMS". In: *Journal of Electroceramics* 12.1/2 (2004), pp. 7–17. ISSN: 1385-3449.

[Tum07] Slawomir Tumanski. "Induction coil sensors—a review". In: *Measurement Science and Technology* 18.3 (2007), R31. ISSN: 0957-0233.

[Tum11] Slawomir Tumanski. *Handbook of Magnetic Measurements*. CRC Press, 2011. ISBN: 978-1-4398-2952-3.

[Tum13] Slawomir Tumanski. "Modern magnetic field sensors–a review". In: *Organ* 10.1 (2013), pp. 1–12.

[Tur+18a] Andrei V. Turutin et al. "Low-frequency magnetic sensing by magnetoelectric metglas/bidomain LiNbO3 long bars". In: *Journal of Physics D: Applied Physics* 51.21 (2018), p. 214001. ISSN: 0022-3727.

[Tur+18b] Andrei V. Turutin et al. "Magnetoelectric metglas/bidomain y + 140°-cut lithium niobate composite for sensing fT magnetic fields". In: *Applied Physics Letters* 112.26 (2018), p. 262906. ISSN: 0003-6951.

[UM20] Tsuyoshi Uchiyama and Jiaju Ma. "Development of pico tesla resolution amorphous wire magneto-impedance sensor for bio-magnetic field measurements". In: *Journal of Magnetism and Magnetic Materials* 514 (2020), p. 167148. ISSN: 03048853.

[Urs+14] Necdet Onur Urs et al. "Origin of hysteretic magnetoelastic behavior in magnetoelectric 2-2 composites". In: *Applied Physics Letters* 105.20 (2014), p. 202406. ISSN: 0003-6951.

[Urs+20] Necdet Onur Urs et al. "Direct Link between Specific Magnetic Domain Activities and Magnetic Noise in Modulated Magnetoelectric Sensors". In: *Physical Review Applied* 13.2 (2020), p. 024018.

[van+00] J. van Driel et al. "Exchange biasing by Ir19Mn81: Dependence on temperature, microstructure and antiferromagnetic layer thickness". In: *Journal of Applied Physics* 88.2 (2000), pp. 975–982. ISSN: 0021-8979.

[Vaz12] C. A. F. Vaz. "Electric field control of magnetism in multiferroic heterostructures". In: *Journal of physics. Condensed matter : an Institute of Physics journal* 24.33 (2012), p. 333201.

[Wan+11] Yaojin Wang et al. "An extremely low equivalent magnetic noise magnetoelectric sensor". In: *Advanced materials (Deerfield Beach, Fla.)* 23.35 (2011), pp. 4111–4114.

[Wik95] J. P. Wikswo. “SQUID magnetometers for biomagnetism and nondestructive testing: Important questions and initial answers”. In: *IEEE Transactions on Appiled Superconductivity* 5.2 (1995), pp. 74–120. ISSN: 10518223.

[Wu+11] Tao Wu et al. “Electrical and Mechanical Manipulation of Ferromagnetic Properties in Polycrystalline Nickel Thin Film”. In: *IEEE Magnetics Letters* 2 (2011), p. 6000104.

[Yab+09] S. Yabukami et al. “A thin film magnetic field sensor of sub-pT resolution and magnetocardiogram (MCG) measurement at room temperature”. In: *Journal of Magnetism and Magnetic Materials* 321.7 (2009), pp. 675–678. ISSN: 03048853.

[Yar+16a] Erdem Yarar et al. “Inverse bilayer magnetoelectric thin film sensor”. In: *Applied Physics Letters* 109.2 (2016), p. 022901. ISSN: 0003-6951.

[Yar+16b] Erdem Yarar et al. “Low temperature aluminum nitride thin films for sensory applications”. In: *AIP Advances* 6.7 (2016), p. 075115. ISSN: 2158-3226.

[Yar+19] Erdem Yarar et al. “MEMS-Based AlScN Resonating Energy Harvester With Solidified Powder Magnet”. In: *Journal of Microelectromechanical Systems* 28.6 (2019), pp. 1019–1031. ISSN: 1057-7157.

[Yar17] Erdem Yarar. “Inverse-Bilayer AlN/(Fe90Co10)78Si12B10 Magnetoelectric Composites”. PhD Thesis. Kiel: CAU Kiel, 2017.

[Zab+15] S. Zabel et al. “Phase modulated magnetoelectric delta-E effect sensor for sub-nano tesla magnetic fields”. In: *Applied Physics Letters* 107.15 (2015), p. 152402. ISSN: 0003-6951.

[Zab+16] Sebastian Zabel et al. “Multimode delta-E effect magnetic field sensors with adapted electrodes”. In: *Applied Physics Letters* 108.22 (2016), p. 222401. ISSN: 0003-6951.

[Zha+08a] Junyi Zhai et al. “Magnetoelectric Laminate Composites: An Overview”. In: *Journal of the American Ceramic Society* 91.2 (2008), pp. 351–358. ISSN: 1551-2916.

[Zha+08b] Junyi Zhai et al. “Magnetoelectric Laminate Composites: An Overview”. In: *Journal of the American Ceramic Society* 91.2 (2008), pp. 351–358. ISSN: 0002-7820.

[Zha+09] J. Zhai et al. “Magnetoelectric gyrator”. In: *The European Physical Journal B* 71.3 (2009), p. 383. ISSN: 1434-6036.

[Zhe+19] Chao Zheng et al. “Magnetoresistive Sensor Development Roadmap (Non-Recording Applications)”. In: *IEEE Transactions on Magnetics* 55.4 (2019), pp. 1–30. ISSN: 0018-9464.

[Zhu+15a] Xin Zhuang et al. “Dynamic Sensitivity and Noise Floor of a Bonded Magneto(Elasto)Electric Laminate for Low Frequency Magnetic Field Sensing under Strain Modulations”. In: *Key Engineering Materials* 644 (2015), pp. 236–239. ISSN: 1662-9795.

[Zhu+15b] Xin Zhuang et al. “Mechanical Noise Limit of a Strain-Coupled Magneto(Elasto)electric Sensor Operating Under a Magnetic or an Electric Field Modulation”. In: *IEEE Sensors Journal* 15.3 (2015), pp. 1575–1587.

[Zhu+15c] Xin Zhuang et al. “Sensitivity and Noise Evaluation of a Bonded Magneto(elasto) Electric Laminated Sensor Based on In-Plane Magnetocapacitance Effect for Quasi-Static Magnetic Field Sensing”. In: *IEEE Transactions on Magnetics* 51.1 (2015), pp. 1–4. ISSN: 0018-9464.

[Zim+05] E. Zimmermann et al. “An AMR sensor-based measurement system for magnetoelectrical resistivity tomography”. In: *IEEE Sensors Journal* 5.2 (2005), pp. 233–241.

[Zur16] Zurich Instruments. *Principles of lock-in detection and the state of the art: White Paper*. Ed. by Zurich Instruments AG. 2016.